JOINT INVERSION OF POTENTIAL FIELD AND ELECTROMAGNETIC DATA USING GRAMIAN CONSTRAINTS

by

Yue Zhu

A dissertation submitted to the faculty of
The University of Utah
in partial fulfillment of the requirements for the degree of

Doctor of Philosophy

in

Geophysics

Department of Geology and Geophysics

The University of Utah

May 2017

The University of Utah Graduate School

STATEMENT OF DISSERTATION APPROVAL

The dissertation of **Yue Zhu**

has been approved by the following supervisory committee members:

Michael S. Zhdanov	, Chair	**3-8-2017** Date Approved
Alexander V. Gribenko	, Member	**2-22-2017** Date Approved
Martin Čuma	, Member	**2-22-2017** Date Approved
Erich U. Petersen	, Member	**2-22-2017** Date Approved
Robert B. Smith	, Member	**3-9-2017** Date Approved

and by **Thure E. Cerling** , Chair/Dean of

the Department/College/School of **Geology and Geophysics**

and by David B. Kieda, Dean of The Graduate School.

ABSTRACT

One of the major challenges in the interpretation of geophysical data remains the ability to jointly invert multiple geophysical datasets for self-consistent three-dimensional (3D) earth models of different physical properties. This dissertation develops a method of joint inversion of potential field and electromagnetic data using Gramian constraints. A model weighting technique was introduced to guarantee a stable and converging joint inversion process. The developed joint inversion algorithm was successfully tested in a number of model studies, where the Gramian constraints make it possible to consider both linear and nonlinear relationships between the different physical properties. This dissertation also develops a novel method of inversion of magnetic data for the magnetization vector, when remanent magnetization is present. The method is based on a new magnetic forward modeling algorithm, which uses triangular prisms of arbitrary shape in order to achieve a more accurate approximation of the topography. The inversion also includes Gramian constraints in order to obtain a robust solution of otherwise ill-posed magnetic inverse problems. Another development in this dissertation is the localized Gramian constraints, which allows one to recover multiple lithologic relationships between the different physical properties. The case study of the joint inversion of airborne magnetic and electromagnetic data in the Lac de Gras area of the Northwest Territories of Canada demonstrated how joint inversion using the localized Gramian constraints can enhance subsurface imaging of mineral targets.

To the mountains and clouds

CONTENTS

ABSTRACT . . . . . **iii**

ACKNOWLEDGMENTS . . . . . **vi**

CHAPTERS

1. INTRODUCTION **1**

1.1 Overview of methodology 1
1.2 Physical property relationships 3
1.3 Thesis developments 4

2. THEORY **6**

2.1 Inversion methodology 6
2.2 Extended discussions 20

3. JOINT INVERSION OF GRAVITY AND MAGNETIC DATA . **25**

3.1 Linear relationship 25
3.2 Nonlinear relationship 29

4. MAGNETIZATION VECTOR INVERSION **47**

4.1 Theory 47
4.2 Model study 53
4.3 Case study 54

5. JOINT INVERSION OF MAGNETIC AND ELECTROMAGNETIC DATA **73**

5.1 Theory 73
5.2 Model study 75
5.3 Case study 76

6. CONCLUSIONS **96**

REFERENCES **98**

ACKNOWLEDGMENTS

I thank the Consortium for Electromagnetic Modeling and Inversion (CEMI) at the Department of Geology and Geophysics, University of Utah, and TechnoImaging for providing financial and technical support for this work. The support and resources from the Center for High Performance Computing at the University of Utah are also gratefully acknowledged. I deeply thank my advisor and chair of my committee, Dr. Michael S. Zhdanov, for his continuous guidance and providing direction of this research. Special thanks to my committee members, Dr. Alexander V. Gribenko and Dr. Martin Čuma, for their support, encouragement, and sharing their exceptional knowledge of geophysical research. I am also thankful to my committee members, Dr. Erich U. Petersen and Dr. Robert B. Smith, for their constructive criticism and suggestions for this work. I acknowledge Yuri Kinakin from Rio Tinto for providing the data and permission to publish the results. I appreciate Dr. Leif Cox for sharing his knowledge and codes of airborne electromagnetic inversion. I am also thankful to Dr. Le Wan for his generous support throughout my PhD study. Thanks to my colleagues from CEMI for helpful discussions and sharing of ideas, especially Dr. Hongzhu Cai and Dr. Daeung Yoon. I also thank the staff in the Department of Geology and Geophysics, University of Utah, for their help, especially Kim Atwater. Special thanks to Michael Jorgensen for his help with the English manuscript of this dissertation. Finally, I would like to thank my family and friends for their constant love and support.

CHAPTER 1

INTRODUCTION

1.1 Overview of methodology

Geophysical inversions are ill-posed problems strongly affected by nonuniqueness and instability (Zhdanov, 2002; Hansen, 2010). Given some observation errors, there usually exist a number of models which can fit the observed data within the noise level. In order to reduce such nonuniqueness and obtain a geologically reasonable model, one needs to incorporate constraints in the geophysical inversion. These constraints are usually based on general physical properties of the model parameters, e.g., conductivities and velocities have to be positive. One can also utilize additional information derived from available geologic and geophysical data in the survey area to reduce the searching space for the solution. This additional information can be incorporated in the form of a joint inversion.

In the paper by Vozoff and Jupp (1975), the joint inversion was first introduced as inverting for one physical property using combined geophysical methods. As the sophistication of geophysical explorations increases, there are often several independent data sets available within a survey area. The different geophysical data provide information about the different physical properties of rock formations. In many cases, this information is mutually complementary, which makes it natural to consider a joint inversion of different geophysical data for multiple physical properties.

Moorkamp et al. (2011) summarized two factors that help the joint inversion narrow the set of acceptable models. First, the different methods have complementary resolving kernels, resulting in the reduced null space for the aggregated data set. Second, the impact of noise differs for different geophysical methods so that adding another method improves the result more than adding more data of the same type.

There are different approaches to recover multiple physical properties in a joint inversion. In a case where the corresponding model parameters are empirically

or statistically correlated, the joint inversion can utilize the specific form of the correlation to reduce the number of unknowns (e.g., Jegen et al., 2009). This direct approach provides a strong coupling between the different model parameters and improves the inversion results when the given correlation is accurate. If the given correlation deviates away from the true relationship, one may get distorted or spurious results. An alternative way is to use the empirical or statistical correlation as a constraint, which provides a looser coupling compared to the direct approach and is less prone to erroneous results (Colombo and Stefano, 2007).

However, in practical applications, the empirical or statistical correlation may exist, but its specific form may be unknown. There is a need for a method of joint inversion which would not require a priori knowledge about the empirical or statistical relationship between the different model parameters. In this case, the joint inversion can be based on structural-coupled constraints (Haber and Oldenburg, 1997; Molodtsov et al., 2013). The one that has been used mostly is the cross-gradient approach (Gallardo and Meju, 2003), which is based on minimizing a value of the cross-gradients between different model parameters.

In the paper by Zhdanov et al. (2012), a new approach to the joint inversion of multimodal data using Gramian constraints was introduced. The Gramians are computed as determinants of the corresponding Gram matrices of the multimodal model parameters or their different attributes. Similar to the cross-gradient approach, the joint inversion with Gramian constraints does not require a priori knowledge about the empirical or statistical relationship between the different model parameters, but instead determines it in the process of the inversion. It was demonstrated in the cited paper that this new approach is a more general technique of the joint inversion, making it possible to consider correlations between any transformed model parameters in a unified way. One can use, for example, second derivatives of the model parameters, absolute values of the gradients, or any other transforms of the model parameters and their gradients.

1.2 Physical property relationships

Geophysical prospecting methods are based on the study of various physical fields, e.g., gravitational, magnetic, electrical, electromagnetic, seismic, thermal, etc. Different fields are related to different physical properties, which are further used to determine certain geologic structures or ore bodies. The physical properties which are most studied in geophysics include density, magnetic susceptibility, resistivity, and seismic velocities. In many cases, these properties are not independent of the others. For petrophysical inversions, the density, conductivity, and seismic velocities are linked through the porosity and water saturation, as described by Archie's law and Gassmann's equations (Abubakar et al., 2012; Gao et al., 2012). For plate tectonics and geothermal studies, the conductivity and seismic velocities are correlated such that both of them are functions of the temperature, pressure, and water content (Berdichevsky and Dmitriev, 2008; Newman et al., 2008). For mineral explorations, there usually exist some empirical or statistical relationships between the different physical properties, which are derived from drilling or field sampling. Although these relationships are usually not known a priori, one can still run joint inversions to correlate the different physical properties using cross-gradients or Gramian constraints (Zhu et al., 2013, 2014, 2015; Zhu and Zhdanov, 2015).

There are a few successful applications of joint inversion for multiple physical properties. In the study of regional geology, joint inversion of seismic traveltimes and magnetotelluric data was used to image the subsalt (De Stefano et al., 2011) and sub-basalt (Jegen et al., 2009) sediment structure, where the porosity effect on velocity and resistivity is dominant. In exploration applications, joint inversion of electromagnetic and seismic data were applied to monitor the oil-water contact by reconstructing the resistivity and seismic velocity models in different stages of reservoir production (Hu et al., 2009). However, it is still challenging to perform joint inversions of multimodal geophysical data. The different physical properties have different units which makes it difficult to determine appropriate weights for the regularization and correlation. One usually has to run many experiments with different weights in order to get satisfying inversion results (Moorkamp et al., 2011).

1.3 Thesis developments

In this dissertation, I formulated the joint inversion using Gramian constraints. Definitions and properties of the Gramians were discussed, and the conjugate gradient algorithm for solving the corresponding inverse problem was also derived. Several major developments to the joint inversion of multimodal geophysical data in this dissertation are summarized below.

The first development relates to the model weighting in the joint inversion algorithm. It is known that different physical properties have different units and can vary by several orders of magnitude, which introduces instability to the joint inversion and may affect the convergence of the inversion process. To overcome this difficulty, I introduced a model weighting technique in the joint inversion, which leads to dimensionless model parameters. This approach contributes to a stable and converging joint inversion algorithm regardless of the different units/magnitudes between the different physical properties.

The next development is localized Gramian constraints. In practical applications, there may exist multiple geologic anomalies, each having a unique lithologic relationship between the different physical properties. I explored the possibility to recover multiple lithologic relationships by the joint inversion. As illustrated by the synthetic model study, the standard joint inversion assumes a uniform lithologic trend throughout the entire inversion domain, which may produce distorted inversion results if this assumption is not true. To solve this problem, I proposed an improved joint inversion framework using the localized Gramian constraints, which allows different lithologic relationships in different subdomains.

The third development relates to the nonlinear correlation in the joint inversion. As discussed in the theory section, direct application of either cross-gradients or Gramian constraints enhances a linear correlation between the different model parameters. I proposed an indirect way to implement a polynomial relationship using Gramian constraints. This approach does not require a priori knowledge of the specific relationship but instead determines the polynomial coefficients in the process of the inversion. Generally, one can use the polynomial relationship to represent other nonlinear correlations, since most nonlinear relationships can be approximated by

a polynomial basis through Taylor expansions.

The fourth development is the new approach for the magnetization vector inversion using Gramian constraints. Usually, one solves for multiple physical properties in the joint inversion by inverting different geophysical data sets simultaneously. In other cases, one may need to invert only one type of geophysical data but for multiple physical properties or components, e.g., Cole-Cole parameters in the induced polarization method, anisotropic conductivities in the marine controlled source electromagnetics. These inverse problems have a large degree of nonuniqueness due to the increased number of unknowns, which are usually difficult to solve. However, the different physical properties or components are supposed to have similar spatial variations and represent the same zones of anomalies. It is natural to consider jointly inverting for the different physical properties or components. In the presence of remanent magnetization, one has to consider the model parameter as the three components of the magnetization vector instead of the magnetic susceptibility. I formulated the magnetic inverse problem using Gramian constraints to impose spatial similarities between the different components of the magnetization vector. To incorporate topography in the modeling domain of the magnetic inversion, I also developed a new magnetic forward modeling algorithm, which uses triangular prisms of arbitrary shape to achieve a more accurate approximation of the topography.

The last major development relates to the joint inversion for the magnetization vector and conductivity. This inverse problem is slightly different from the joint inversions discussed earlier, as one of the model parameters, the magnetization vector, is a vector of three scalar components, and thus has a different length than the other - the conductivity. In the case study for kimberlite exploration, there is an empirical correlation between the magnetization vector and the conductivity, in that the magnetization vector components and the conductivity have the same anomalous areas. Thus, I included three Gramian constraints when formulating the joint inverse problem, each used for a spatial correlation between one component of the magnetization vector and the conductivity.

CHAPTER 2

THEORY

This chapter is a mathematical preparation for the joint inversion using Gramian constraints. To start, Section 2.1.1 reviews the regularization theory of the inherently ill-posed geophysical inversions. This leads to the minimization of a parametric functional of two parts, (1) the misfit functional for least-square fitting of the observed data, and (2) the stabilizer for regularizing the properties of the solution. Section 2.1.2 introduces the parametric functional for the joint inversion, which has an additional term, the Gramian constraint, to measure the correlation between the different physical properties. The joint inversion is known for the difficulty that different physical properties have different units and can vary by several orders of magnitude. Section 2.1.3 provides a solution to this by modifying the parametric functional with new weighted model parameters. Section 2.1.4 then derives the conjugate gradient algorithm for solving the corresponding inverse problem. The second part of this chapter provides discussions about the cross-gradient approach and nonlinear correlation between the different physical properties.

2.1 Inversion methodology

2.1.1 Regularization theory

Regularization refers to a process of introducing additional information to solve an ill-posed problem, which cannot meet one or more of the following three conditions, existence, uniqueness, and stability (Zhdanov, 2002; Hansen, 2010). Unfortunately, geophysical inversions belong to the ill-posed problems, which require appropriate regularization to stabilize the inversion process. Basic ideas about the regularization are reviewed in this section. Consider a discrete linear inverse problem as follows:

$$\mathbf{Fm} = \mathbf{d}, \tag{2.1}$$

where the system matrix $\mathbf{F}$ is generally not square. One may consider the least square solution to problem (2.1), which is

$$\mathbf{m} = \left(\mathbf{F}^\top \mathbf{F}\right)^{-1} \mathbf{F}^\top \mathbf{d}. \tag{2.2}$$

Geophysical inversions can be represented in the discrete form as equation (2.1), where $\mathbf{F}$ is obtained from Taylor expansion of a general nonlinear forward operator. Ill-posed here means that matrix $\mathbf{F}^\top \mathbf{F}$ is singular or close to singular, and the resulted solution $\mathbf{m}$ in formula (2.2) is unstable. So small variations in the data vector $\mathbf{d}$ due to the observation errors can produce dramatic changes in the solution $\mathbf{m}$. In this dissertation, I mainly deal with the underdetermined system, where the number of unknowns is much greater than that of the data points. This is fairly common in the geophysical applications and is one of the major reasons for the ill-posedness of the inverse problems.

The classical way to stabilize the inverse problem (2.1) is through the Tikhonov regularization (Tikhonov, 1963), which yields the following solution:

$$\mathbf{m} = \left(\mathbf{F}^\top \mathbf{F} + \alpha \mathbf{I}\right)^{-1} \mathbf{F}^\top \mathbf{d}, \tag{2.3}$$

where α is some small positive number called the regularization parameter, and $\mathbf{I}$ is the identity matrix. By inserting some positive numbers to the diagonal elements of $\mathbf{F}^\top \mathbf{F}$, the matrix $\left(\mathbf{F}^\top \mathbf{F} + \alpha \mathbf{I}\right)$ becomes better conditioned.

Indeed, equation (2.3) is the solution to the optimization problem as follows:

$$P(\mathbf{m}) = \|\mathbf{F}\mathbf{m} - \mathbf{d}\|^2 + \alpha \|\mathbf{m}\|^2 \rightarrow \min. \tag{2.4}$$

The first term of the parametric functional $P(\mathbf{m})$ is called the misfit functional, which performs the least square fitting of the observed data, and the second term is the stabilizer for the regularization, which states the properties of the solution.

The stabilizer in expression (2.4) is the simplest one, the minimum norm stabilizer. It has a general form written as follows (Zhdanov, 2002):

$$S_{MN}(\mathbf{m}) = \|\mathbf{m} - \mathbf{m}_{apr}\|^2, \tag{2.5}$$

where $\mathbf{m}_{apr}$ is a priori model. This stabilizer is used to find a solution close to $\mathbf{m}_{apr}$. For the case of zero $\mathbf{m}_{apr}$, as in expression (2.4), one searches for a solution which fits the data and has a minimum length.

There are many other stabilizing functionals, e.g., the maximum smooth stabilizer (Zhdanov, 2002):

$$S_{MaxS}\left(\mathbf{m}\right)=\left\|\nabla\mathbf{m}\right\|^{2}, \tag{2.6}$$

which produces a smooth solution in the space, and the Occam stabilizer (Constable et al., 1987; Zhdanov, 2002):

$$S_{Occam}\left(\mathbf{m}\right)=\left\|\nabla^{2}\mathbf{m}\right\|^{2}, \tag{2.7}$$

which imposes Occam's razor on the solution.

2.1.2 Joint inversion formulation

Consider two different geophysical data sets, $\mathbf{d}^{(i)}$, and the related two physical properties, $\mathbf{m}^{(i)}$, for $i=1,2$. The separate inversions require the minimization of two independent parametric functionals as follows:

$$P\left(\mathbf{m}^{(i)}\right)=\left\|\mathbf{W}_{d}^{(i)}\left(\mathbf{A}^{(i)}(\mathbf{m}^{(i)})-\mathbf{d}^{(i)}\right)\right\|^{2}+\alpha^{(i)}\left\|\mathbf{W}_{m}^{(i)}\left(\mathbf{m}^{(i)}-\mathbf{m}_{apr}^{(i)}\right)\right\|^{2},i=1,2, \tag{2.8}$$

where $\mathbf{W}_{d}^{(i)}$ and $\mathbf{W}_{m}^{(i)}$ are the diagonal data and model weighting matrices.

The joint inversion recovers two physical properties simultaneously by using a single parametric functional according to the following formula:

$$\begin{aligned}P\left(\mathbf{m}^{(1)},\mathbf{m}^{(2)}\right)&=\sum_{i=1}^{2}\left\|\mathbf{W}_{d}^{(i)}\left(\mathbf{A}^{(i)}(\mathbf{m}^{(i)})-\mathbf{d}^{(i)}\right)\right\|^{2}\\&+\sum_{i=1}^{2}\alpha^{(i)}\left\|\mathbf{W}_{m}^{(i)}\left(\mathbf{m}^{(i)}-\mathbf{m}_{apr}^{(i)}\right)\right\|^{2}+\beta S_{G_{T}}\left(\mathbf{m}^{(1)},\mathbf{m}^{(2)}\right),\end{aligned} \tag{2.9}$$

where $\alpha^{(i)}$ and β are the positive regularization and correlation parameters, respectively. The term $S_{G_T}\left(\mathbf{m}^{(1)},\mathbf{m}^{(2)}\right)$ is the Gramian constraint of model parameter transforms (Zhdanov et al., 2012). In a case of two physical properties, it can be written as follows:

$$S_{G_{T}}\left(\mathbf{m}^{(1)},\mathbf{m}^{(2)}\right)=\begin{vmatrix}\left\langle\mathbf{T}^{(1)}\mathbf{m}^{(1)},\mathbf{T}^{(1)}\mathbf{m}^{(1)}\right\rangle & \left\langle\mathbf{T}^{(1)}\mathbf{m}^{(1)},\mathbf{T}^{(2)}\mathbf{m}^{(2)}\right\rangle\\ \left\langle\mathbf{T}^{(2)}\mathbf{m}^{(2)},\mathbf{T}^{(1)}\mathbf{m}^{(1)}\right\rangle & \left\langle\mathbf{T}^{(2)}\mathbf{m}^{(2)},\mathbf{T}^{(2)}\mathbf{m}^{(2)}\right\rangle\end{vmatrix}, \tag{2.10}$$

where $\mathbf{T}^{(i)}$ are the transform operators, and $\langle\ ,\ \rangle$ stands for the inner product.

The matrices $\mathbf{T}^{(i)}$ can be used for various purposes. If the two model parameters are discretized differently, they can be mapped onto the same grid by choosing $\mathbf{T}^{(i)}$ as the projecting operators. The matrices $\mathbf{T}^{(i)}$ can also be the discrete differential operators, logarithmic, exponential, or any other transforms which emphasize the specific properties of the models. All these transformations can be considered as the attributes of the model parameters, because they are defined as some functions of the model parameters (Zhdanov et al., 2012).

Expression (2.10) can be further written as follows:

$$S_G\big(\mathbf{m}_t^{(1)}, \mathbf{m}_t^{(2)}\big) = \begin{vmatrix} \big\langle \mathbf{m}_t^{(1)}, \mathbf{m}_t^{(1)} \big\rangle & \big\langle \mathbf{m}_t^{(1)}, \mathbf{m}_t^{(2)} \big\rangle \\ \big\langle \mathbf{m}_t^{(2)}, \mathbf{m}_t^{(1)} \big\rangle & \big\langle \mathbf{m}_t^{(2)}, \mathbf{m}_t^{(2)} \big\rangle \end{vmatrix}$$

$$= \big\|\mathbf{m}_t^{(1)}\big\|^2 \big\|\mathbf{m}_t^{(2)}\big\|^2 \big(1 - \eta^2\big(\mathbf{m}_t^{(1)}, \mathbf{m}_t^{(2)}\big)\big), \tag{2.11}$$

where $\mathbf{m}_t^{(i)} = \mathbf{T}^{(i)}\mathbf{m}^{(i)}$, and $\eta\big(\mathbf{m}_t^{(1)}, \mathbf{m}_t^{(2)}\big)$ is the correlation coefficient:

$$\eta\big(\mathbf{m}_t^{(1)}, \mathbf{m}_t^{(2)}\big) = \frac{\big\langle \mathbf{m}_t^{(1)}, \mathbf{m}_t^{(2)} \big\rangle}{\big\|\mathbf{m}_t^{(1)}\big\| \big\|\mathbf{m}_t^{(2)}\big\|}. \tag{2.12}$$

The following inequality holds for any transformed model parameters:

$$\big\langle \mathbf{m}_t^{(1)}, \mathbf{m}_t^{(2)} \big\rangle \leq \big\|\mathbf{m}_t^{(1)}\big\| \big\|\mathbf{m}_t^{(2)}\big\|. \tag{2.13}$$

Therefore, one can obtain

$$0 \leq \eta^2\big(\mathbf{m}_t^{(1)}, \mathbf{m}_t^{(2)}\big) \leq 1, \tag{2.14}$$

and

$$S_G\big(\mathbf{m}_t^{(1)}, \mathbf{m}_t^{(2)}\big) \geq 0. \tag{2.15}$$

Expression (2.11) shows that the Gramian constraint provides a measure of the correlation between the two transformed model parameters. Indeed, the Gramian goes to zero, when the correlation coefficient η is close to one, which corresponds to the maximum correlation. Thus, by minimizing a parametric functional with the Gramian constraint (2.10), one enforces a correlation between the model parameters or their attributes.

2.1.3 Model and data weightings

It is known that different physical properties have different units and can vary by several orders of magnitude, which introduces instability to the joint inversion and may affect the convergence of the inversion process. An appropriate model weighting is critical for a stable and converging joint inversion algorithm.

Consider the following normalized model parameters:

$$\widetilde{\mathbf{m}}^{(i)} = W_{m,c}^{(i)}\big(\mathbf{m}^{(i)} - \mathbf{m}_b^{(i)}\big), \tag{2.16}$$

where $W_{m,c}^{(i)}$ are the model weighting coefficients, and $\mathbf{m}_b^{(i)}$ are the background physical properties. If one selects the model weighting coefficients in an appropriate way, the effect of the units and magnitudes can be removed, resulting the dimensionless model parameters $\widetilde{\mathbf{m}}^{(i)}$. However, this requires a priori knowledge of the model parameters that one is solving for. Most of the time, before running the joint inversion, I first apply the separate inversions for benchmarking the joint inversion results. In this case, the inverted models obtained by the separate inversions can be used to compute the model weighting coefficients for the joint inversion, which are defined as follows:

$$W_{m,c}^{(i)} = \frac{1}{\max\left|\mathbf{m}_s^{(i)} - \mathbf{m}_b^{(i)}\right|}, \tag{2.17}$$

where $\mathbf{m}_s^{(i)}$ are the solutions obtained from the separate inversions.

Note that, the model parameters obtained in the separate and joint inversions usually have a similar order of magnitude. Therefore, the normalized model parameters in formula (2.16) are approximately bound between -1 to 1. To make use of the dimensionless model parameters, I formulate the joint inversion for $\widetilde{\mathbf{m}}^{(i)}$ as follows:

$$\begin{aligned} P\left(\widetilde{\mathbf{m}}^{(1)}, \widetilde{\mathbf{m}}^{(2)}\right) &= \sum_{i=1}^{2} \left\|\mathbf{W}_d^{(i)}\left(\tilde{\mathbf{A}}^{(i)}\left(\widetilde{\mathbf{m}}^{(i)}\right) - \mathbf{d}^{(i)}\right)\right\|^2 \\ &+ \sum_{i=1}^{2} \alpha^{(i)} \left\|\mathbf{W}_m^{(i)}\left(\widetilde{\mathbf{m}}^{(i)} - \widetilde{\mathbf{m}}_{apr}^{(i)}\right)\right\|^2 + \beta S_{G_T}\left(\widetilde{\mathbf{m}}^{(1)}, \widetilde{\mathbf{m}}^{(2)}\right), \end{aligned} \tag{2.18}$$

where $\tilde{\mathbf{A}}^{(i)}\left(\widetilde{\mathbf{m}}^{(i)}\right) = \mathbf{A}^{(i)}\left(\mathbf{m}^{(i)}\right)$.

The model weighting coefficients act as multipliers to the regularization and correlation parameters in the above parametric functional, if one substitutes expression (2.18) with formulas (2.16) and (2.17). The solutions to the minimization problem

(2.9) is equivalent to problem (2.18), given comparable regularization and correlation parameters. By correlating the normalized model parameters in expression (2.18), the selection of the correlation parameter becomes independent of the units and magnitudes of the different physical properties.

In the past, I computed the model weighting coefficients in a different way:

$$W_{m,c}^{(i),n+1} = \frac{1}{\left\| \mathbf{m}_n^{(i)} - \mathbf{m}_b^{(i)} \right\|}, \tag{2.19}$$

where n and $n+1$ are the iteration numbers, considering an iterative inversion process. Since the solutions $\mathbf{m}^{(i)}$ are unknown, $W_{m,c}^{(i)}$ at current iteration are computed using the model parameters obtained at the previous iteration. The model weighting coefficients by formula (2.19) change from iteration to iteration, which introduces instability to the joint inversion. In contrast, $W_{m,c}^{(i)}$ in formula (2.17) are constants, which work better for a stable and converging joint inversion algorithm.

In expression (2.18), the data weighting matrices are computed as follows:

$$\mathbf{W}_d^{(i)} = W_{d,c}^{(i)} \mathbf{W}_{d,s}^{(i)}, \tag{2.20}$$

where $\mathbf{W}_{d,s}^{(i)}$ are the diagonal data weighting matrices used in the separate inversions, and $W_{d,c}^{(i)}$ are the weighting coefficients used for the different data sets in the joint inversion. I select the data weighting coefficients as follows:

$$W_{d,c}^{(i)} = \frac{1}{\left\| \mathbf{W}_{d,s}^{(i)} \left(\tilde{\mathbf{A}}^{(i)}(\widetilde{\mathbf{m}}_{ini}^{(i)}) - \mathbf{d}^{(i)} \right) \right\|}, \tag{2.21}$$

where $\widetilde{\mathbf{m}}_{ini}^{(i)}$ are the initial normalized model parameters. In this way, the misfit functionals can be written as follows:

$$\Phi^{(i)}(\widetilde{\mathbf{m}}^{(i)}) = \frac{\left\| \mathbf{W}_{d,s}^{(i)} \left(\tilde{\mathbf{A}}^{(i)}(\widetilde{\mathbf{m}}^{(i)}) - \mathbf{d}^{(i)} \right) \right\|^2}{\left\| \mathbf{W}_{d,s}^{(i)} \left(\tilde{\mathbf{A}}^{(i)}(\widetilde{\mathbf{m}}_{ini}^{(i)}) - \mathbf{d}^{(i)} \right) \right\|^2}. \tag{2.22}$$

In the first iteration of an inversion process, with $\widetilde{\mathbf{m}}^{(i)} = \widetilde{\mathbf{m}}_{ini}^{(i)}$, both misfit functionals are equal to 1. This allows the misfits of the different data sets to vary in comparable magnitudes in the following iterations, and thus have the same level of data fittings in the final results.

2.1.4 Conjugate gradient algorithm

The conjugate gradient method is used to solve the optimization problem (2.18), which requires a calculation of the gradient (steepest ascent direction) of the parametric functional. The first variation of the parametric functional is calculated as:

$$\delta P\left(\widetilde{\mathbf{m}}^{(1)},\widetilde{\mathbf{m}}^{(2)}\right)=2\sum_{i=1}^{2}\left(\delta\tilde{\mathbf{A}}^{(i)}\left(\widetilde{\mathbf{m}}^{(i)}\right)\right)^{\top}\left(\mathbf{W}_{d}^{(i)}\right)^{2}\left(\tilde{\mathbf{A}}^{(i)}\left(\widetilde{\mathbf{m}}^{(i)}\right)-\mathbf{d}^{(i)}\right)$$

$$+2\sum_{i=1}^{2}\alpha^{(i)}\left(\delta\widetilde{\mathbf{m}}^{(i)}\right)^{\top}\left(\mathbf{W}_{m}^{(i)}\right)^{2}\left(\widetilde{\mathbf{m}}^{(i)}-\widetilde{\mathbf{m}}_{apr}^{(i)}\right)+\beta\delta S_{G_T}\left(\widetilde{\mathbf{m}}^{(1)},\widetilde{\mathbf{m}}^{(2)}\right). \tag{2.23}$$

Taking into consideration that the operators $\tilde{\mathbf{A}}^{(i)}$ are differentiable, one can write:

$$\delta\tilde{\mathbf{A}}^{(i)}\left(\mathbf{m}^{(i)}\right)=\tilde{\mathbf{F}}^{(i)}\delta\widetilde{\mathbf{m}}^{(i)},i=1,2, \tag{2.24}$$

where $\tilde{\mathbf{F}}^{(i)}$ are the Fréchet derivative matrices of $\tilde{\mathbf{A}}^{(i)}$.

The first variation of the Gramian constraint is calculated as follows:

$$\delta S_{G_T}\left(\widetilde{\mathbf{m}}^{(1)},\widetilde{\mathbf{m}}^{(2)}\right)=2\sum_{i=1}^{2}\left(\delta\widetilde{\mathbf{m}}^{(i)}\right)^{\top}\mathbf{l}_{G}^{(i)}, \tag{2.25}$$

where the vectors $\mathbf{l}_{G}^{(i)}$ are given as:

$$\mathbf{l}_{G}^{(1)}=\left(\mathbf{T}^{(1)}\right)^{\top}\left\{\widetilde{\mathbf{m}}_{t}^{(1)}\left[\left(\widetilde{\mathbf{m}}_{t}^{(2)}\right)^{\top}\left(\widetilde{\mathbf{m}}_{t}^{(2)}\right)\right]-\widetilde{\mathbf{m}}_{t}^{(2)}\left[\left(\widetilde{\mathbf{m}}_{t}^{(2)}\right)^{\top}\left(\widetilde{\mathbf{m}}_{t}^{(1)}\right)\right]\right\}, \tag{2.26}$$

$$\mathbf{l}_{G}^{(2)}=\left(\mathbf{T}^{(2)}\right)^{\top}\left\{\widetilde{\mathbf{m}}_{t}^{(2)}\left[\left(\widetilde{\mathbf{m}}_{t}^{(1)}\right)^{\top}\left(\widetilde{\mathbf{m}}_{t}^{(1)}\right)\right]-\widetilde{\mathbf{m}}_{t}^{(1)}\left[\left(\widetilde{\mathbf{m}}_{t}^{(1)}\right)^{\top}\left(\widetilde{\mathbf{m}}_{t}^{(2)}\right)\right]\right\}, \tag{2.27}$$

and the vectors $\widetilde{\mathbf{m}}_{t}^{(i)}$ are defined as:

$$\widetilde{\mathbf{m}}_{t}^{(i)}=\mathbf{T}^{(i)}\widetilde{\mathbf{m}}^{(i)},i=1,2. \tag{2.28}$$

After some algebra, the vectors $\mathbf{l}_{G}^{(i)}$ can be further represented as follows:

$$\mathbf{l}_{G}^{(i)}=\mathbf{G}^{(i)}\widetilde{\mathbf{m}}^{(i)},i=1,2, \tag{2.29}$$

where the matrices $\mathbf{G}^{(i)}$ are computed as:

$$\mathbf{G}^{(1)}=\left(\mathbf{T}^{(1)}\right)^{\top}\left[\left(\widetilde{\mathbf{m}}_{t}^{(2)}\right)^{\top}\left(\widetilde{\mathbf{m}}_{t}^{(2)}\right)\mathbf{I}-\left(\widetilde{\mathbf{m}}_{t}^{(2)}\right)\left(\widetilde{\mathbf{m}}_{t}^{(2)}\right)^{\top}\right]\mathbf{T}^{(1)}, \tag{2.30}$$

$$\mathbf{G}^{(2)}=\left(\mathbf{T}^{(2)}\right)^{\top}\left[\left(\widetilde{\mathbf{m}}_{t}^{(1)}\right)^{\top}\left(\widetilde{\mathbf{m}}_{t}^{(1)}\right)\mathbf{I}-\left(\widetilde{\mathbf{m}}_{t}^{(1)}\right)\left(\widetilde{\mathbf{m}}_{t}^{(1)}\right)^{\top}\right]\mathbf{T}^{(2)}. \tag{2.31}$$

and the operator $\mathbf{I}$ is the identity matrix.

Substituting expressions (2.24) and (2.25) into formula (2.23), one can obtain:

$$\delta P\left(\widetilde{\mathbf{m}}^{(1)}, \widetilde{\mathbf{m}}^{(2)}\right) = 2\sum_{i=1}^{2}\left(\delta\widetilde{\mathbf{m}}^{(i)}\right)^{\top}\mathbf{l}^{(i)}, \tag{2.32}$$

where the steepest ascent directions $\mathbf{l}^{(i)}$ are calculated as follows:

$$\mathbf{l}^{(i)} = \left(\tilde{\mathbf{F}}^{(i)}\right)^{*}\left(\mathbf{W}_d^{(i)}\right)^2\mathbf{r}^{(i)} + \alpha^{(i)}\left(\mathbf{W}_m^{(i)}\right)^2\left(\widetilde{\mathbf{m}}^{(i)} - \widetilde{\mathbf{m}}_{apr}^{(i)}\right) + \beta\mathbf{G}^{(i)}\widetilde{\mathbf{m}}^{(i)}, \tag{2.33}$$

The operator * represents the conjugate transpose of a general complex Fréchet derivative matrix, e.g., in electromagnetic inversions. The vectors $\mathbf{r}^{(i)}$ in the above formula are the data residuals:

$$\mathbf{r}^{(i)} = \tilde{\mathbf{A}}^{(i)}\left(\widetilde{\mathbf{m}}^{(i)}\right) - \mathbf{d}^{(i)}, i = 1, 2. \tag{2.34}$$

If one selects

$$\delta\widetilde{\mathbf{m}}^{(i)} = -k\mathbf{l}^{(i)}, i = 1, 2, \tag{2.35}$$

where k is some positive real number. Then

$$\delta P(\widetilde{\mathbf{m}}^{(1)}, \widetilde{\mathbf{m}}^{(2)}) = -2k\sum_{i=1}^{2}\left\|\mathbf{l}^{(i)}\right\|^2. \tag{2.36}$$

Expression (2.36) confirms that the selection of the perturbations of the model parameters based on formula (2.33) ensures the decrease of the parametric functional.

The matrix $\mathbf{G}^{(1)}$ is independent of $\widetilde{\mathbf{m}}^{(1)}$ but a function of $\widetilde{\mathbf{m}}^{(2)}$. Similarly, the matrix $\mathbf{G}^{(2)}$ is independent of $\widetilde{\mathbf{m}}^{(2)}$ but a function of $\widetilde{\mathbf{m}}^{(1)}$. Therefore, the joint inversion (2.9) is inherently nonlinear, even if the forward operators $\tilde{\mathbf{A}}^{(i)}$ are linear. Iterative algorithms, e.g., conjugate gradient method, iterative Newton's method, etc., are suggested to use for problem (2.9). The joint inversion is also affected by the initial models, as other nonlinear problems. In this dissertation, the half space initial models are used mostly, which turns out to be a good choice by allowing a smooth growth of the correlation between the solutions, if there is one.

I construct an iterative process using the regularized conjugate gradient (RCG) algorithm for problem (2.9), which can be summarized as follows:

$$\mathbf{r}_n = \tilde{\mathbf{A}}\left(\widetilde{\mathbf{m}}_n\right) - \mathbf{d}, \tag{2.37a}$$

$$\mathbf{l}_n = \tilde{\mathbf{F}}^* \mathbf{W}_d^2 \mathbf{r}_n + \alpha \mathbf{W}_m^2 \left(\widetilde{\mathbf{m}}_n - \widetilde{\mathbf{m}}_{apr} \right) + \beta \mathbf{G} \widetilde{\mathbf{m}}_n, \tag{2.37b}$$

$$\tilde{\mathbf{l}}_n = \mathbf{l}_n + \frac{\|\mathbf{l}_n\|^2}{\|\mathbf{l}_{n-1}\|^2} \tilde{\mathbf{l}}_{n-1}, \ \tilde{\mathbf{l}}_0 = \mathbf{l}_0, \tag{2.37c}$$

$$\tilde{k}_n = \frac{\tilde{\mathbf{l}}_n^\top \mathbf{l}_n}{\tilde{\mathbf{l}}_n^\top \left(\mathbf{F}^* \mathbf{W}_d^2 \mathbf{F} + \alpha \mathbf{W}_m^2 + \beta \mathbf{G} \right) \tilde{\mathbf{l}}_n}, \tag{2.37d}$$

$$\widetilde{\mathbf{m}}_{n+1} = \widetilde{\mathbf{m}}_n - \tilde{k}_n \tilde{\mathbf{l}}_n. \tag{2.37e}$$

In the last formula I use the following notations:

$$\widetilde{\mathbf{m}}_n = \begin{bmatrix} \widetilde{\mathbf{m}}_n^{(1)} \\ \\ \widetilde{\mathbf{m}}_n^{(2)} \end{bmatrix},$$

$$\mathbf{d} = \begin{bmatrix} \mathbf{d}^{(1)} \\ \\ \mathbf{d}^{(2)} \end{bmatrix},$$

$$\tilde{\mathbf{F}} = \begin{bmatrix} \tilde{\mathbf{F}}^{(1)} & \\ & \tilde{\mathbf{F}}^{(2)} \end{bmatrix},$$

$$\mathbf{W}_d = \begin{bmatrix} \mathbf{W}_d^{(1)} & \\ & \mathbf{W}_d^{(2)} \end{bmatrix},$$

$$\alpha = \begin{bmatrix} \alpha^{(1)} \mathbf{I}^{(1)} & \\ & \alpha^{(2)} \mathbf{I}^{(2)} \end{bmatrix},$$

$$\mathbf{W}_m = \begin{bmatrix} \mathbf{W}_m^{(1)} & \\ & \mathbf{W}_m^{(2)} \end{bmatrix},$$

$$\mathbf{G} = \begin{bmatrix} \mathbf{G}^{(1)} & \\ & \mathbf{G}^{(2)} \end{bmatrix},$$

where $\mathbf{I}^{(i)}$ are the identity matrices. In process (2.37), I arrange $\widetilde{\mathbf{m}}^{(1)}$ and $\widetilde{\mathbf{m}}^{(2)}$ into a big vector $\widetilde{\mathbf{m}}$ and update this aggregated model parameter iteratively.

An alternate algorithm to the above process is to update the normalized model parameters $\widetilde{\mathbf{m}}^{(1)}$ and $\widetilde{\mathbf{m}}^{(2)}$ sequentially at iteration number n as follows:

$$\mathbf{r}_n^{(i)} = \tilde{\mathbf{A}}^{(i)}\big(\widetilde{\mathbf{m}}_n^{(i)}\big) - \mathbf{d}^{(i)}, \tag{2.38a}$$

$$\mathbf{l}_n^{(i)} = \big(\tilde{\mathbf{F}}^{(i)}\big)^*\big(\mathbf{W}_d^{(i)}\big)^2\mathbf{r}_n^{(i)} + \alpha^{(i)}\big(\mathbf{W}_m^{(i)}\big)^2\big(\widetilde{\mathbf{m}}_n^{(i)} - \widetilde{\mathbf{m}}_{apr}^{(i)}\big) + \beta\mathbf{G}^{(i)}\widetilde{\mathbf{m}}_n^{(i)}, \tag{2.38b}$$

$$\tilde{\mathbf{l}}_n^{(i)} = \mathbf{l}_n^{(i)} + \frac{\big\|\mathbf{l}_n^{(i)}\big\|^2}{\big\|\mathbf{l}_{n-1}^{(i)}\big\|^2}\tilde{\mathbf{l}}_{n-1}^{(i)},\ \tilde{\mathbf{l}}_0^{(i)} = \mathbf{l}_0^{(i)}, \tag{2.38c}$$

$$\tilde{k}_n^{(i)} = \frac{\big(\tilde{\mathbf{l}}_n^{(i)}\big)^\top\mathbf{l}_n^{(i)}}{\big(\tilde{\mathbf{l}}_n^{(i)}\big)^\top\Big(\big(\mathbf{F}^{(i)}\big)^*\big(\mathbf{W}_d^{(i)}\big)^2\mathbf{F}^{(i)} + \alpha\big(\mathbf{W}_m^{(i)}\big)^2 + \beta\mathbf{G}^{(i)}\Big)\tilde{\mathbf{l}}_n^{(i)}}, \tag{2.38d}$$

$$\widetilde{\mathbf{m}}_{n+1}^{(i)} = \widetilde{\mathbf{m}}_n^{(i)} - \tilde{k}_n^{(i)}\tilde{\mathbf{l}}_n^{(i)}, \tag{2.38e}$$

for $i = 1, 2$. The conjugate directions and step lengths are computed slightly different between processes (2.37) and (2.38). If there is difficulty of convergence using algorithm (2.37) in an inversion, one can try process (2.38) since different step lengths of the different model parameters may help the convergence of the inversion.

As usual, iterative process (2.37) or (2.38) is terminated when the misfit reaches the required level δ_d:

$$\Phi\left(\widetilde{\mathbf{m}}_{n+1}\right) = \left\|\mathbf{r}_{n+1}\right\|^2 = \delta_d. \tag{2.39}$$

Figure 2.1 gives the main steps of the joint inversion using Gramian constraints and normalized model parameters in a flow chart.

I usually run several inversions with zero correlation parameter, $\beta = 0$, to find suitable regularization parameters, $\alpha^{(i)}$, and then moderately increase the correlation parameter, β, until the inversion results are acceptable. The values of the regularization and correlation parameters in this dissertation are selected as follows:

$$\alpha^{(i)} = 10^{-6} \sim 10^{-2} \times \frac{\big\|\mathbf{W}_d^{(i)}\big(\tilde{\mathbf{A}}^{(i)}\left(\widetilde{\mathbf{m}}_1^{(i)}\right) - \mathbf{d}^{(i)}\big)\big\|^2}{\big\|\mathbf{W}_m^{(i)}\big(\widetilde{\mathbf{m}}_1^{(i)} - \widetilde{\mathbf{m}}_{apr}^{(i)}\big)\big\|^2}, i = 1, 2, \tag{2.40}$$

$$\beta = 10^{-6} \sim 10^{-2} \times \frac{\sum_{i=1,2}\big\|\mathbf{W}_d^{(i)}\big(\tilde{\mathbf{A}}^{(i)}\big(\widetilde{\mathbf{m}}_1^{(i)}\big) - \mathbf{d}^{(i)}\big)\big\|^2}{S_{G_T}\big(\widetilde{\mathbf{m}}_1^{(1)}, \widetilde{\mathbf{m}}_1^{(2)}\big)}, \tag{2.41}$$

where $\mathbf{m}_1^{(i)}$ are the model parameters recovered from the first iteration.

2.1.5 Fréchet derivative computation

Here, I briefly discuss the forward modeling and Fréchet derivative computation of gravity, magnetic, and electromagnetic methods. The gravity and gravity gradiometry fields caused by the density source $\rho(\mathbf{r})$ distributed within volume V can be represented by the following integral formulas:

$$g_\alpha(\mathbf{r}') = \gamma \iiint_D \rho(\mathbf{r}) \frac{\alpha - \alpha'}{|\mathbf{r} - \mathbf{r}'|^3} dv, \tag{2.42}$$

$$g_{\alpha\beta}(\mathbf{r}') = \gamma \iiint_D \rho(\mathbf{r}) \frac{1}{|\mathbf{r} - \mathbf{r}'|^3} \left(\frac{3(\alpha - \alpha')^2}{|\mathbf{r} - \mathbf{r}'|^2} - 1 \right) dv, \alpha = \beta, \tag{2.43}$$

$$g_{\alpha\beta}(\mathbf{r}') = \gamma \iiint_D \rho(\mathbf{r}) \frac{3(\alpha - \alpha')(\beta - \beta')}{|\mathbf{r} - \mathbf{r}'|^5} dv, \alpha \neq \beta, \tag{2.44}$$

where $\mathbf{r}$ is the radius vector of a point within the volume V, and $\mathbf{r}'$ is the vector of an observation point; γ is the universal gravitational constant; $\alpha, \beta = x, y, z$, and $\alpha,' \beta' = x', y', z'$.

By discretizing a three-dimensional (3D) earth model into a grid of N_m cells and assuming each has a constant density, the gravity and gravity gradiometry fields can be expressed in the following discrete form (Zhdanov, 2002):

$$g_\alpha(\mathbf{r}') = \gamma \sum_{k=1}^{N_m} \rho_k \iiint_{V_k} \frac{\alpha - \alpha'}{|\mathbf{r} - \mathbf{r}'|^3} dv, \tag{2.45}$$

$$g_{\alpha\beta}(\mathbf{r}') = \gamma \sum_{k=1}^{N_m} \rho_k \iiint_{V_k} \frac{1}{|\mathbf{r} - \mathbf{r}'|^3} \left(\frac{3(\alpha - \alpha')^2}{|\mathbf{r} - \mathbf{r}'|^2} - 1 \right) dv, \alpha = \beta, \tag{2.46}$$

$$g_{\alpha\beta}(\mathbf{r}') = \gamma \sum_{k=1}^{N_m} \rho_k \iiint_{V_k} \frac{3(\alpha - \alpha')(\beta - \beta')}{|\mathbf{r} - \mathbf{r}'|^5} dv, \alpha \neq \beta. \tag{2.47}$$

where ρ_k is the density of the k^{th} cell. One can use Gaussian quadrature to numerically evaluate the integrals in the above formulas.

Assume a discrete number of observation points $\mathbf{r}'_n = (x'_n, y'_n, z'_n)$, with $n = 1, ..., N_d$. Using discrete model parameters and discrete data, one can represent the gravity forward modeling in the matrix notation as follows:

$$\mathbf{d}^g = \mathbf{A}^g \mathbf{m}, \tag{2.48}$$

where $\mathbf{d}^g$ is the N_d length vector of the observed gravity data, $\mathbf{m}$ is the N_m length vector of the density, and $\mathbf{A}^g$ is a linear operator of the gravity forward modeling problem. Both $\mathbf{d}^g$ and $\mathbf{A}^g$ may be partitioned for joint modeling and inversion of multiple component gravity data.

The anomalous magnetic field induced by the magnetic source distributed within volume V with the magnetization vector $\mathbf{I}(\mathbf{r})$ can be represented by the following integral formula:

$$\mathbf{H}(\mathbf{r}') = -\iiint_D \frac{1}{|\mathbf{r}-\mathbf{r}'|^3}\left(\mathbf{I}(\mathbf{r}) - \frac{3\big(\mathbf{I}(\mathbf{r})\cdot(\mathbf{r}-\mathbf{r}')\big)(\mathbf{r}-\mathbf{r}')}{|\mathbf{r}-\mathbf{r}'|^2}\right)dv. \tag{2.49}$$

By discretizing a 3D earth model into a grid of N_m cells and assuming each has a constant intensity of magnetization, the magnetic field can be expressed in the following discrete form (Zhdanov, 2002):

$$\mathbf{H}(\mathbf{r}') = -\sum_{k=1}^{N_m}\iiint_{V_k} \frac{1}{|\mathbf{r}-\mathbf{r}'|^3}\left(\mathbf{I}_k - \frac{3\big(\mathbf{I}_k\cdot(\mathbf{r}-\mathbf{r}')\big)(\mathbf{r}-\mathbf{r}')}{|\mathbf{r}-\mathbf{r}'|^2}\right)dv, \tag{2.50}$$

where $\mathbf{I}_k$ is the intensity of magnetization of the k^{th} cell. Similarly, a Gaussian quadrature can be used to numerically evaluate the integral in the above formula.

In ground and airborne magnetic surveys, the total magnetic intensity field is measured, which can be computed approximately as follows:

$$\Delta T(\mathbf{r}') \approx \mathbf{l}(\mathbf{r}')\cdot\Delta\mathbf{H}(\mathbf{r}'). \tag{2.51}$$

I assume that the x axis is directed eastward, the y axis is directed northward, and the z axis is directed downward. Given the inclination (I), declination (D), and azimuth (A) from the International Geomagnetic Reference Field (IGRF), the direction of the inducing magnetic field can be computed as follows:

$$l_x = \cos(I)\sin(D-A), \tag{2.52}$$

$$l_y = \cos(I)\cos(D-A), \tag{2.53}$$

$$l_z = \sin(I). \tag{2.54}$$

If there is no remanent magnetization, the intensity of magnetization, $\mathbf{I}(\mathbf{r})$, is linearly related to an inducing magnetic field, $\mathbf{H}_0(\mathbf{r})$, through the magnetic susceptibility, $\chi(\mathbf{r})$:

$$\mathbf{I}(\mathbf{r}) = \chi(\mathbf{r})\mathbf{H}_0(\mathbf{r}) = \chi(\mathbf{r})H_0\mathbf{l}(\mathbf{r}), \tag{2.55}$$

where $\mathbf{l}(\mathbf{r})$ is the unit vector along the direction of the inducing field. If the remanent magnetization is present, one needs to consider the magnetic model parameter as the magnetization vector rather than the scalar susceptibility. This modifies equation (2.55) as follows:

$$\mathbf{I}(\mathbf{r}) = H_0\mathbf{M}(\mathbf{r}), \tag{2.56}$$

where $\mathbf{M}$ has two parts: induced, $\mathbf{M}_{ind}$, and remnant, $\mathbf{M}_{rem}$, magnetizations:

$$\mathbf{M}(\mathbf{r}) = \mathbf{M}_{ind}(\mathbf{r}) + \mathbf{M}_{rem}(\mathbf{r}). \tag{2.57}$$

Similarly, I consider a discrete number of observation points $\mathbf{r}'_n = (x'_n, y'_n, z'_n)$, with $n = 1, ..., N_d$. Using discrete model parameters and discrete data, one can represent the magnetic forward modeling in the matrix notation as follows:

$$\mathbf{d}^m = \mathbf{A}^m\mathbf{m}, \tag{2.58}$$

where $\mathbf{d}^m$ is the N_d length vector of the observed magnetic data, and $\mathbf{A}^m$ is a linear operator of the magnetic forward modeling problem. If there is no remanent magnetization, $\mathbf{m}$ is the N_m length vector of the magnetic susceptibility. If the remanent magnetization is present, $\mathbf{m}$ becomes the $3N_m$ length vector of the magnetization vector components. Also, both $\mathbf{d}^m$ and $\mathbf{A}^m$ may be partitioned for joint modeling and inversion of multiple component magnetic data.

Consider a 3D geoelectrical model with background conductivity of σ_b and some local inhomogeneous domain D. The conductivity within the domain D can be written as $\sigma = \sigma_b + \Delta\sigma$. This model is excited by an electromagnetic field generated by an arbitrary source with an extraneous current distribution $\mathbf{j}^e$ within some domain Q. Assume the field is monochromatic and changes with time as e^{-iwt}. One can express the anomalous fields produced by the anomalous conductivity distribution $\Delta\sigma$ using the following integral representation (Hohmann, 1975; Zhdanov, 2009):

$$\mathbf{E}^a(\mathbf{r}') = \iiint_D \widehat{\mathbf{G}}_E(\mathbf{r}'|\mathbf{r})\Delta\sigma(\mathbf{r}) \cdot \mathbf{E}(\mathbf{r})dv, \tag{2.59}$$

$$\mathbf{H}^a(\mathbf{r}') = \iiint_D \widehat{\mathbf{G}}_H(\mathbf{r}'|\mathbf{r})\Delta\sigma(\mathbf{r}) \cdot \mathbf{E}(\mathbf{r})dv, \tag{2.60}$$

where $\mathbf{E}(\mathbf{r})$ is the total electric field induced in domain D with the anomalous conductivity, $\Delta\sigma$, which can be decomposed into a sum of the background, $\mathbf{E}^b$, and anomalous, $\mathbf{E}^a$, fields as follows:

$$\mathbf{E} = \mathbf{E}^b + \mathbf{E}^a. \tag{2.61}$$

Electric field $\mathbf{E}(\mathbf{r})$ in domain D can be found using a conventional integral equation (IE) method, by solving the corresponding domain equation:

$$\mathbf{E}^a(\mathbf{r}') = \iiint_D \widehat{\mathbf{G}}_E(\mathbf{r}'|\mathbf{r})\Delta\sigma(\mathbf{r}) \cdot \left[\mathbf{E}^b(\mathbf{r}) + \mathbf{E}^a(\mathbf{r})\right] dv. \tag{2.62}$$

In formulas (2.59) and (2.60), $\widehat{\mathbf{G}}_E(\mathbf{r}'|\mathbf{r})$ and $\widehat{\mathbf{G}}_H(\mathbf{r}'|\mathbf{r})$ are the electric and magnetic Green's tensors defined for a medium with the background conductivity, σ_b. In the paper by Hursán and Zhdanov (2002), a contraction IE algorithm was developed to solve for the domain electric field in equation (2.62).

One can represent the forward modeling of airborne EM data as the following matrix equation:

$$\mathbf{d}^{em} = \mathbf{A}^{em}(\mathbf{m}), \tag{2.63}$$

where $\mathbf{d}^{em}$ is the N_d length vector of observed data, $\mathbf{m}$ is the N_m length vector of the anomalous conductivities, $\Delta\sigma$; and $\mathbf{A}^{em}$ is the nonlinear EM modeling operator.

In the case of gravity or magnetic inversion, the Fréchet derivative matrix is identical to the forward modeling operator. In the case of electromagnetic inversion, the Fréchet derivative matrix is computed using the quasi-Born approximation (Gribenko and Zhdanov, 2007) as follows:

$$\mathbf{F}_E = \mathbf{G}_E\mathbf{E}_D, \tag{2.64}$$

$$\mathbf{F}_H = \mathbf{G}_H\mathbf{E}_D, \tag{2.65}$$

where $\mathbf{E}_D$ is the total electric field inside the inhomogeneous domain D, and $\mathbf{F}_E$ and $\mathbf{F}_H$ are the Fréchet derivatives of the electric and magnetic fields, respectively.

2.2 Extended discussions

2.2.1 Cross-gradient constraint

One of the approaches to formulate the joint inversion is the use of the cross-gradients, which enhances structural similarities between the different model parameters. The cross-gradient constraint is defined as follows (Gallardo and Meju, 2003):

$$S_{cg}\left(m^{(1)}(\mathbf{r}), m^{(2)}(\mathbf{r})\right) = \left\|\nabla m^{(1)}(\mathbf{r}) \times \nabla m^{(2)}(\mathbf{r})\right\|^2, \tag{2.66}$$

where $m^{(i)}(\mathbf{r}), i = 1, 2$, are the volume distributions of the model parameters.

The cross-gradient constraint is minimized, when the two gradients, $\nabla m^{(1)}(\mathbf{r})$ and $\nabla m^{(2)}(\mathbf{r})$, are parallel to each other, resulting in the following linear relationship:

$$\nabla m^{(1)}(\mathbf{r}) = k \nabla m^{(2)}(\mathbf{r}), \tag{2.67}$$

or its equivalence

$$m^{(1)}(\mathbf{r}) = k m^{(2)}(\mathbf{r}) + b. \tag{2.68}$$

Condition (2.68) holds for arbitrary k and b, implying that there are infinite pairs of $m^{(1)}(\mathbf{r})$ and $m^{(2)}(\mathbf{r})$ that can minimize the cross-gradient constraint. The final solutions are the ones that can fit the observed data in the meanwhile. That is, k and b are determined by minimizing the misfit functionals (of course, with the stabilizers).

One can also construct a gradient-type Gramian constraint as follows, which works in a similar way as the cross-gradient constraint:

$$S_{G_\nabla}\left(m^{(1)}(\mathbf{r}), m^{(2)}(\mathbf{r})\right) = \begin{vmatrix} \left\langle \nabla m^{(1)}(\mathbf{r}), \nabla m^{(1)}(\mathbf{r}) \right\rangle & \left\langle \nabla m^{(1)}(\mathbf{r}), \nabla m^{(2)}(\mathbf{r}) \right\rangle \\ \left\langle \nabla m^{(2)}(\mathbf{r}), \nabla m^{(1)}(\mathbf{r}) \right\rangle & \left\langle \nabla m^{(2)}(\mathbf{r}), \nabla m^{(2)}(\mathbf{r}) \right\rangle \end{vmatrix}. \tag{2.69}$$

Expression (2.69) gets minimized when the two gradients, $\nabla m^{(1)}(\mathbf{r})$ and $\nabla m^{(2)}(\mathbf{r})$, are linearly correlated, which is equivalent to either condition (2.67) or (2.68). In contrast, the following Gramian constraint,

$$S_G\left(m^{(1)}(\mathbf{r}), m^{(2)}(\mathbf{r})\right) = \begin{vmatrix} \left\langle m^{(1)}(\mathbf{r}), m^{(1)}(\mathbf{r}) \right\rangle & \left\langle m^{(1)}(\mathbf{r}), m^{(2)}(\mathbf{r}) \right\rangle \\ \left\langle m^{(2)}(\mathbf{r}), m^{(1)}(\mathbf{r}) \right\rangle & \left\langle m^{(2)}(\mathbf{r}), m^{(2)}(\mathbf{r}) \right\rangle \end{vmatrix}, \tag{2.70}$$

approaches zero when the model parameters satisfy:

$$m^{(1)}(\mathbf{r}) = k m^{(2)}(\mathbf{r}), \tag{2.71}$$

which is condition (2.68) for the special case $b = 0$.

If one considers the model parameters as the anomalous physical properties,

$$\widetilde{m}^{(i)}(\mathbf{r}) = m^{(i)}(\mathbf{r}) - m_b^{(i)}(\mathbf{r}),\ i = 1, 2, \tag{2.72}$$

where $m_b^{(i)}(\mathbf{r})$ are the background, all the three constraints, S_{cg}, $S_{G\nabla}$, and S_G, become equivalent and approach zeros when:

$$\widetilde{m}^{(1)}(\mathbf{r}) = k\widetilde{m}^{(2)}(\mathbf{r}). \tag{2.73}$$

In this case, minimizing a parametric functional with any of the three constraints would enhance the same linear correlation between the model parameters (2.72).

However, there is a subtle difference in the numerical implementation of the three constraints. I did a few numerical tests and found that the joint inversion using S_G is better conditioned than the other two, S_{cg} and $S_{G\nabla}$, by avoiding the gradient operator. This directly affects the convergence rate when using iterative solvers for the joint inversion.

2.2.2 Nonlinear relationship

Inversions usually produce smoothed or averaged results compared to the true solutions. Thus, it makes sense to approximate the nonlinear relationship with the linear one when the variations of the model parameters are relatively smooth. However, if the linear approximation cannot meet the accuracy, one should consider the nonlinear relationship for a better characterization of the true models. Here, I provide a way to implement the nonlinear correlation by assuming a polynomial relationship between the two model parameters.

Consider a quadratic relationship as follows:

$$\widetilde{m}^{(2)}(\mathbf{r}) = c_1\widetilde{m}^{(1)}(\mathbf{r}) + c_2\big(\widetilde{m}^{(1)}(\mathbf{r})\big)^2, \tag{2.74}$$

where $\widetilde{m}(\mathbf{r})^{(i)} = m^{(i)}(\mathbf{r}) - m_b^{(i)}(\mathbf{r})$ are the anomalous physical properties. The following Gramian constraint gets minimized under condition (2.74) for arbitrary c_1 and c_2:

$$S_G\big(c_1\widetilde{m}^{(1)}(\mathbf{r}) + c_2\left(\widetilde{m}^{(1)}(\mathbf{r})\right)^2, \widetilde{m}^{(2)}(\mathbf{r})\big) =$$

$$\begin{vmatrix} \left\| c_1\widetilde{m}^{(1)}(\mathbf{r}) + c_2\left(\widetilde{m}^{(1)}(\mathbf{r})\right)^2 \right\|^2 & \left\langle c_1\widetilde{m}^{(1)}(\mathbf{r}) + c_2\left(\widetilde{m}^{(1)}(\mathbf{r})\right)^2, \widetilde{m}^{(2)}(\mathbf{r}) \right\rangle \\ \left\langle \widetilde{m}^{(2)}(\mathbf{r}), c_1\widetilde{m}^{(1)}(\mathbf{r}) + c_2\left(\widetilde{m}^{(1)}(\mathbf{r})\right)^2 \right\rangle & \left\| \widetilde{m}^{(2)}(\mathbf{r}) \right\|^2 \end{vmatrix}. \quad (2.75)$$

However, one cannot implement this Gramian constraint directly because the coefficients c_1 and c_2 are unknown.

I further decompose the Gramian constraint (2.75) into three parts as follows:

$$S_G\big(c_1\widetilde{m}^{(1)}(\mathbf{r}) + c_2\left(\widetilde{m}^{(1)}(\mathbf{r})\right)^2, \widetilde{m}^{(2)}(\mathbf{r})\big) =$$

$$c_1 S_G\left(\widetilde{m}^{(1)}(\mathbf{r}), \widetilde{m}^{(2)}(\mathbf{r})\right) + c_2 S_G\big(\left(\widetilde{m}^{(1)}(\mathbf{r})\right)^2, \widetilde{m}^{(2)}(\mathbf{r})\big)$$

$$+2c_1c_2 S_{NG}\big(\widetilde{m}^{(1)}(\mathbf{r}), \left(\widetilde{m}^{(1)}\right)^2, \widetilde{m}^{(2)}(\mathbf{r})\big), \quad (2.76)$$

where $S_G\left(\widetilde{m}^{(1)}(\mathbf{r}), \widetilde{m}^{(2)}(\mathbf{r})\right)$ and $S_G\big(\left(\widetilde{m}^{(1)}(\mathbf{r})\right)^2, \widetilde{m}^{(2)}(\mathbf{r})\big)$ are the Gramian constraints:

$$S_G\left(\widetilde{m}^{(1)}(\mathbf{r}), \widetilde{m}^{(2)}(\mathbf{r})\right) = \begin{vmatrix} \left\| \widetilde{m}^{(1)}(\mathbf{r}) \right\|^2 & \left\langle \widetilde{m}^{(1)}(\mathbf{r}), \widetilde{m}^{(2)}(\mathbf{r}) \right\rangle \\ \left\langle \widetilde{m}^{(2)}(\mathbf{r}), \widetilde{m}^{(1)}(\mathbf{r}) \right\rangle & \left\| \widetilde{m}^{(2)}(\mathbf{r}) \right\|^2 \end{vmatrix}, \quad (2.77)$$

$$S_G\big(\left(\widetilde{m}^{(1)}(\mathbf{r})\right)^2, \widetilde{m}^{(2)}(\mathbf{r})\big) = \begin{vmatrix} \left\| \left(\widetilde{m}^{(1)}(\mathbf{r})\right)^2 \right\|^2 & \left\langle \left(\widetilde{m}^{(1)}(\mathbf{r})\right)^2, \widetilde{m}^{(2)}(\mathbf{r}) \right\rangle \\ \left\langle \widetilde{m}^{(2)}(\mathbf{r}), \left(\widetilde{m}^{(1)}(\mathbf{r})\right)^2 \right\rangle & \left\| \widetilde{m}^{(2)}(\mathbf{r}) \right\|^2 \end{vmatrix}, \quad (2.78)$$

and S_{NG} is a non-Gramian term:

$$S_{NG} = \begin{vmatrix} \left\langle \widetilde{m}^{(1)}(\mathbf{r}), \left(\widetilde{m}^{(1)}(\mathbf{r})\right)^2 \right\rangle & \left\langle \widetilde{m}^{(1)}(\mathbf{r}), \widetilde{m}^{(2)}(\mathbf{r}) \right\rangle \\ \left\langle \widetilde{m}^{(2)}(\mathbf{r}), \left(\widetilde{m}^{(1)}(\mathbf{r})\right)^2 \right\rangle & \left\langle \widetilde{m}^{(2)}(\mathbf{r}), \widetilde{m}^{(2)}(\mathbf{r}) \right\rangle \end{vmatrix}. \quad (2.79)$$

Numerical test indicates that S_{NG} is also non-negative. Thus, by minimizing a parametric functional containing the constraints from (2.77) to (2.79), it is possible to impose a quadratic relationship between the anomalous physical properties without knowing the coefficients c_1 and c_2 in advance.

To implement a general N order polynomial relationship as follows:

$$\widetilde{m}^{(2)}(\mathbf{r}) = c_1\widetilde{m}^{(1)}(\mathbf{r}) + \cdots + c_N\big(\widetilde{m}^{(1)}(\mathbf{r})\big)^N, \quad (2.80)$$

one can use a similar approach to find the corresponding constraints: (1) construct a prototype Gramian constraint like formula (2.75); (2) decompose it into several

parts, which are all independent of the coefficients c_i $(i = 1, ..., N)$, e.g., expressions (2.77) to (2.79). Generally, one can use the polynomial relationship to represent other nonlinear correlations, since most nonlinear relationships can be approximated by the polynomial basis through Taylor expansions.

One advantage of the approach described above is that it does not require a priori knowledge about the specific relationship but instead determines the polynomial coefficients, c_1, .., to c_N, in the process of the inversion. However, one is responsible to make assumptions about the order of the polynomial relationship. If the variations of the model parameters are relatively smooth, which correspond to most of the examples in this dissertation, the linear correlation $(N = 1)$ is accurate enough.

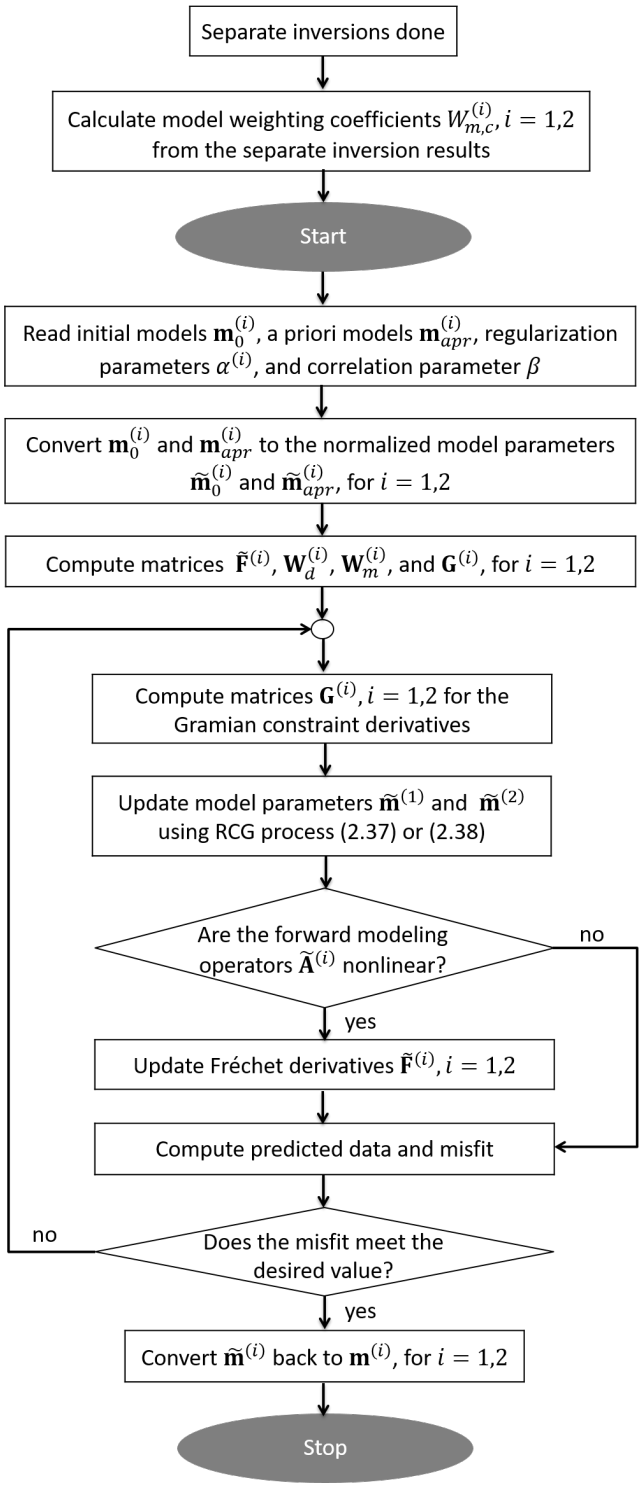

Figure 2.1. Flow chart showing the main steps of the joint inversion using Gramian constraints and normalized model parameters.

CHAPTER 3

JOINT INVERSION OF GRAVITY AND MAGNETIC DATA

This chapter presents synthetic model studies for the joint inversion of gravity and magnetic data. Section 3.1.1 begins with a synthetic model with one block anomaly, which has a large difference in the magnitude between the density and magnetic susceptibility. This model is used to verify the stability and convergence of the joint inversion algorithm derived in the previous chapter. Section 3.1.2 moves to the second synthetic model with two cubic anomalies, each having a unique lithologic relationship between the density and magnetic susceptibility. An improved joint inversion process using the localized Gramian constraints was developed to recover multiple lithologic relationships. Sections 3.2.1 presents one more model study to recover a nonlinear relationship between the density and magnetic susceptibility.

3.1 Linear relationship

3.1.1 Model 1: A block model

Consider a synthetic model with an anomaly of the size 400 m by 400 m by 200 m, as shown in Figure 3.1. There are 441 receivers at 30 m above the ground, covering an area of 1 km by 1 km with a horizontal spacing of 50 m by 50 m. The density and magnetic susceptibility within the anomaly are 1.0 g/cm^3 and 6×10^{-4} SI, respectively. There is a large difference in the magnitude between the two physical properties in order to test the stability and convergence of the joint inversion algorithm. The synthetic gravity, gravity gradiometry, and total magnetic intensity (TMI) fields were calculated and inverted. I ran both separate and joint inversions with the same domain size of 1000 m $\times$ 1000 m $\times$ 500 m and a uniform rectangular grid of 50 m $\times$ 50 m $\times$ 50 m.

For this simple block model, the separate inversions recovered the shape of the anomaly reasonably well, as shown in Figure 3.2. The lower part of the recovered density anomaly is less diffused than that of the magnetic susceptibility anomaly, which is due to the fact that the gravity field g_z decays slower than the TMI field, and as a result, has a higher sensitivity in the deeper part of the inversion domain. I ran the joint inversion by minimizing the parametric functional in formula (2.18) with $T^{(i)} = \nabla$, and using the model weighting coefficients according to formulas (2.17). In comparison to the separate inversion results, the two properties recovered by the joint inversion share a similar structural feature, especially for the lower part of the anomaly, as shown in Figure 3.3.

The cross plots of the recovered physical properties (density and magnetic susceptibility in this case) provide good means to visualize the lithologic relationships between these properties. The cross plot derived from the separate inversions in Figure 3.4 (a) revealed a linear trend between the density and magnetic susceptibility, which is already close to the true relationship. However, there remain some cloudy regions, e.g., near the origin and upper end of the recovered trend. In contrast, the cross plot based on the results of the joint inversion in Figure 3.4 (b) is cleaner with points lined up and tightly following the true relationship. The slope of the recovered linear trend indicates the correct ratio between different properties of the anomaly. Thus, I can conclude that, if the actual correlation exists between the different properties, the joint inversion will find the proper distributions of these properties and will recover the existing trend in the corresponding cross plot. The convergence plot in Figure 3.5 shows a smooth decrease of the misfit functional as the iteration number increases. This result confirms that the developed joint inversion algorithm is effective and stable, considering the different units and magnitudes of the different physical properties.

3.1.2 Model 2: Two blocks

The second synthetic model consists of two cubic anomalies, both with side lengths of 200 m, as shown in Figure 3.6. One of the cubes has a larger density (1.0 g/cm^3) and lower magnetic susceptibility (0.06 SI), while the other one has a smaller density

(0.5 g/cm^3) and a higher magnetic susceptibility (0.1 SI). There are 441 receivers at 30 m above the ground, covering an area of 1 km by 1 km with the spacing in the horizontal directions of 50 m by 50 m. The gravity, gravity gradiometry, and TMI fields were calculated and inverted. I ran several different inversions with the same domain size of 1000 m $\times$ 1000 m $\times$ 500 m and a uniform rectangular grid of 50 m $\times$ 50 m $\times$ 50 m.

Figure 3.7 presents the results of the separate inversions for this model. Both the gravity and magnetic inversions recovered two anomalies with reasonable positions and geometries, especially the horizontal extent. There are also more diffused anomalies in the deeper parts for the magnetic susceptibility than for the density model. The recovered model from the separate inversions has a normalized misfit of 0.08, which is calculated according to the following formula:

$$\varphi = \big(\sum_{i=1,2} \|\mathbf{A}^{(i)}(\mathbf{m}^{(i)}) - \mathbf{d}^{(i)}\|^2 / \sum_{i=1,2} \|\mathbf{d}^{(i)}\|^2\big)^{1/2}. \tag{3.1}$$

The cross plot based on the results of the separate inversions gives some indication, though unclear, of the presence of two lithologic trends between the density and magnetic susceptibility.

I also ran the joint inversion for this model, with $T^{(i)} = \nabla$ in the Gramian constraint in formula (2.18). Although the joint inversion recovered two anomalies, the magnitudes of the density and magnetic susceptibility anomalies are not correct, as shown Figure 3.8. As a result, the recovered model has a relatively large normalized misfit of 0.28. The cross plot derived from current joint inversion reveals only one lithologic trend, which further indicates that the recovered magnitudes of the density and magnetic susceptibility are distorted.

Comparing the separate and joint inversion results, it seems that the distortion comes from correlating the different physical properties in the joint inversion. To verify this, I ran another joint inversion with a decreased correlation parameter. This time, the magnitudes of the recovered density and magnetic susceptibility anomalies were improved, as in Figure 3.9, resulting in a normalized misfit of 0.11. There are two clustered trends in the cross plot derived from current joint inversion, which is

another evidence of improvement. However, comparing the recovered lithologic trends with the true ones, they are still not accurate enough.

Further analysis indicates that the current joint inversion method in formula (2.18) enforces a single uniform lithologic relationship between the different physical properties throughout the inversion domain. If this assumption is true, one can get reasonable results, as shown in Figure 3.3. However, if this assumption gets violated, one may get the distorted models, as shown in Figure 3.8, where only one trend was recovered instead of two. By reducing the correlation parameter, I diminished this distortion effect, as shown in Figures 3.9, where multiple trends showed up in the cross plot. However, this does not always solve the problem.

In order to allow different types of correlations for the different anomalies, I divide the inversion domain into N subdomains, each containing a specific lithologic relationship between the different physical properties. I also modify the parametric functional in formula (2.18) to represent different Gramian terms for the different subdomains, as follows:

$$P(\widetilde{\mathbf{m}}^{(1)},\widetilde{\mathbf{m}}^{(2)}) = \sum_{i=1}^{2} \left\| \mathbf{W}_d^{(i)} \left(\tilde{\mathbf{A}}^{(i)}(\widetilde{\mathbf{m}}^{(i)}) - \mathbf{d}^{(i)} \right) \right\|^2$$

$$+ \sum_{i=1}^{2} \alpha^{(i)} \left\| \mathbf{W}_m^{(i)} \left(\widetilde{\mathbf{m}}^{(i)} - \widetilde{\mathbf{m}}_{apr}^{(i)} \right) \right\|^2 + \beta \sum_{j=1}^{N} S_{G_T}\left(\widetilde{\mathbf{m}}_j^{(1)}, \widetilde{\mathbf{m}}_j^{(2)} \right), \tag{3.2}$$

where $\widetilde{\mathbf{m}}_j^{(i)}$ are the normalized model parameters within the j^{th} subdomain. Minimizing this parametric functional allows one to enforce the following relationships:

$$T^{(1)}\widetilde{\mathbf{m}}_j^{(1)} = k_j T^{(2)} \widetilde{\mathbf{m}}_j^{(2)}, \tag{3.3}$$

where k_j can be different for the different subdomains. Appropriate subdomains can be established based on the available geology and the results of the separate inversions. I call this approach *a joint inversion with localized Gramian constraints*.

For example, for current synthetic model, it is easy to determine two anomalies and the related subdomains from the separate inversion results, corresponding to the volumes covering two separate blocks. The joint inversion based on minimization of the modified parametric functional in formula (3.2) produced the distributions of the

density and magnetic susceptibility with more accurate magnitudes and locations, as shown in Figure 3.10, resulting in a decreased misfit of 0.06. The cross plot derived from current joint inversion clearly reveals two linear trends, each with a unique slope close to the true relationship.

A comparison between the cross plots derived from the separate and joint inversions is presented in Figure 3.11. Figure 3.12 summarizes the main steps of the joint inversion with the localized Gramian constraints in a flow chart. The success of this approach is mainly related to grouping the existing lithologic relationships and establishing the corresponding subdomains, which I suggest to get from the results of the separate inversions using statistical tools, e.g., k-means clustering.

3.2 Nonlinear relationship

3.2.1 Model 3: A dipping dike

Consider a synthetic model of a dipping dike. The dike has a horizontal dimension of 250 m by 300 m and extends vertically from 50 m to 400 m, as shown in Figure 3.13. There are 441 receivers covering an area of 1 km by 1 km with a horizontal spacing of 50 m by 50 m. The density and magnetic susceptibility of the anomaly increase from the top to the bottom. There is a nonlinear relationship between the two physical properties as follows:

$$\log(\chi(\mathbf{r}) + \chi_b) = c_1\rho(\mathbf{r}) + c_2, \tag{3.4}$$

where χ_b, c_1 and c_2 are some constants. The gravity, gravity gradiometry, and TMI fields were calculated and inverted. I ran the joint inversion to enhance a quadratic relationship between the density and magnetic susceptibility, which is based on a parametric functional as follows:

$$P(\widetilde{\mathbf{m}}^{(1)}, \widetilde{\mathbf{m}}^{(2)}) = \sum_{i=1}^{2} \left(\left\| \mathbf{W}_d^{(i)} \left(\tilde{\mathbf{A}}^{(i)}(\widetilde{\mathbf{m}}^{(i)}) - \mathbf{d}^{(i)} \right) \right\|^2 + \alpha^{(i)} \left\| \mathbf{W}_m^{(i)} \left(\widetilde{\mathbf{m}}^{(i)} - \widetilde{\mathbf{m}}_{apr}^{(i)} \right) \right\|^2 \right)$$

$$+\beta_1 S_G\left(\widetilde{\mathbf{m}}^{(1)}, \widetilde{\mathbf{m}}^{(2)}\right) + \beta_2 S_G\left(\left(\widetilde{\mathbf{m}}^{(1)}\right)^2, \widetilde{\mathbf{m}}^{(2)}\right) + \beta_3 S_{NG}\left(\widetilde{\mathbf{m}}^{(1)}, \left(\widetilde{\mathbf{m}}^{(1)}\right)^2, \widetilde{\mathbf{m}}^{(2)}\right), \tag{3.5}$$

where the normalized model parameters are defined as follows:

$$\widetilde{\mathbf{m}}^{(1)} = W_{m,c}^{(1)}\,\rho(\mathbf{r}), \tag{3.6}$$

$$\widetilde{\mathbf{m}}^{(2)} = W_{m,c}^{(2)}\,\chi(\mathbf{r}). \tag{3.7}$$

The separate and joint inversion results are shown in Figures 3.14 and Figure 3.15, respectively. The joint inversion recovered a better dipping structure and more accurate bulk density and magnetic susceptibility of the anomaly than the separate inversions. A comparison between the cross plots derived from the separate and joint inversions in Figure 3.16 shows that the joint inversion enhances a quadratic relationship between the density and magnetic susceptibility, which gives a better approximation of the true nonlinear relationship.

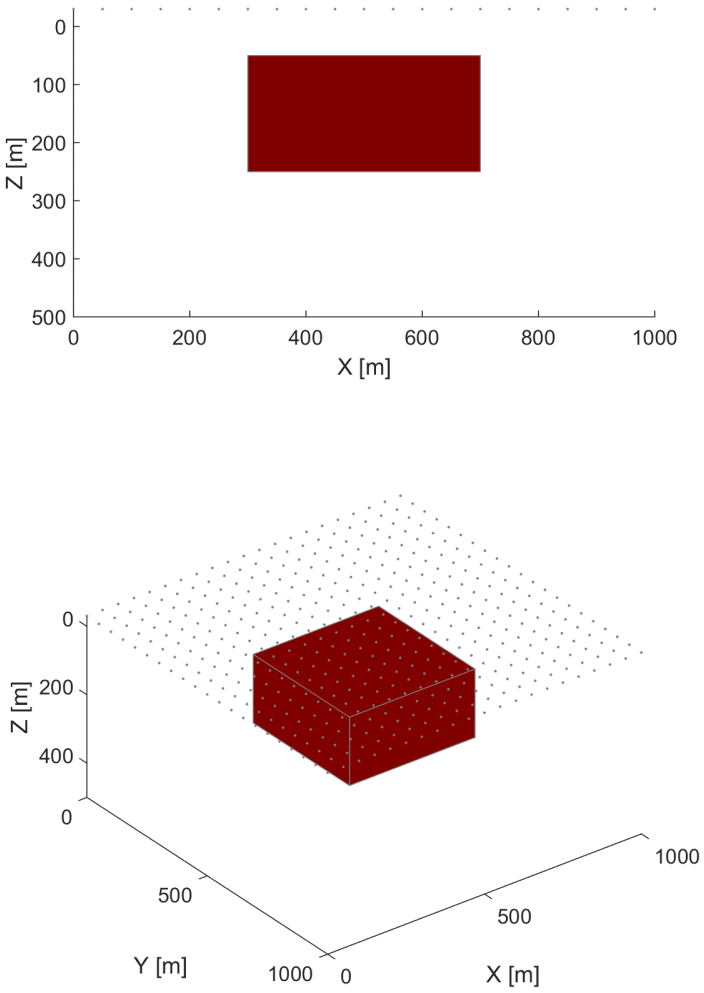

Figure 3.1. Model 1. Vertical (top) and 3D (bottom) views of the block. The size of the anomaly is 400 m × 400 m × 200 m. The gray dots indicate the positions of the receivers.

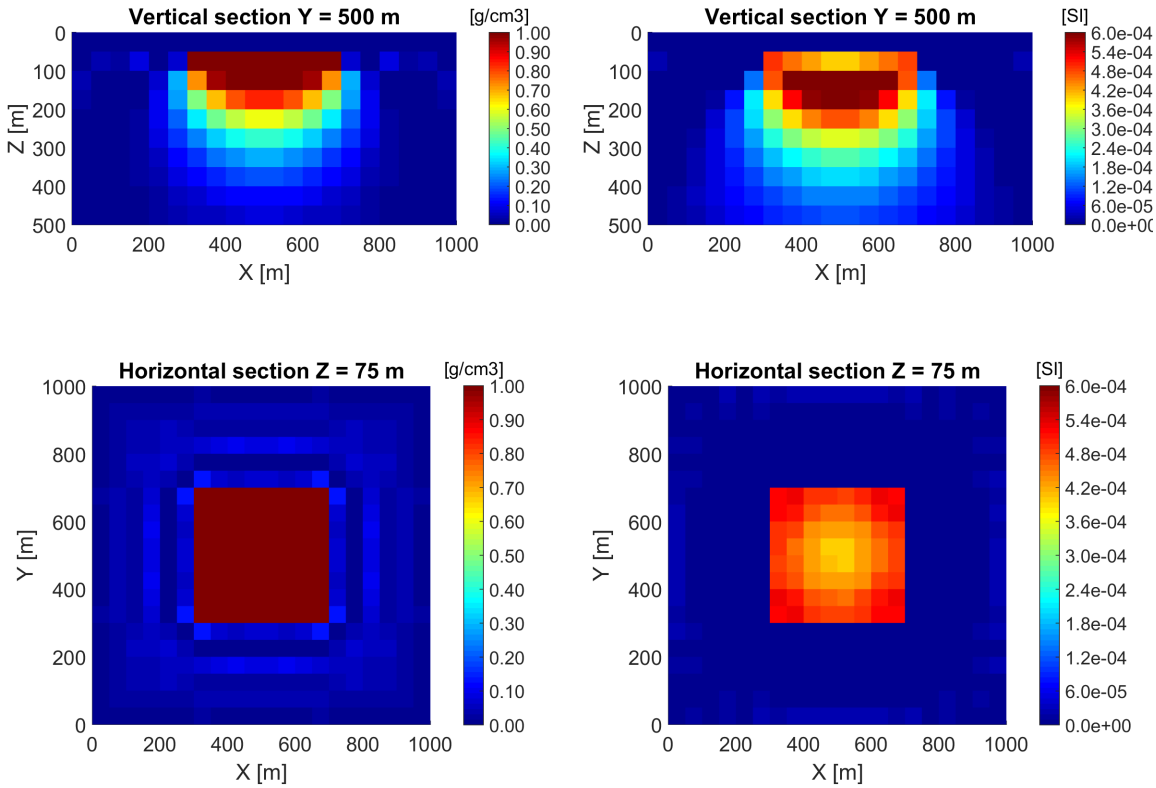

Figure 3.2. Model 1. The density (left panels) and magnetic susceptibility (right panels) of the block model recovered from the separate inversions. The vertical (top panels) and horizontal (bottom panels) sections are provided. The lower boundary of the anomaly is more diffused in the recovered magnetic susceptibility than in the recovered density model.

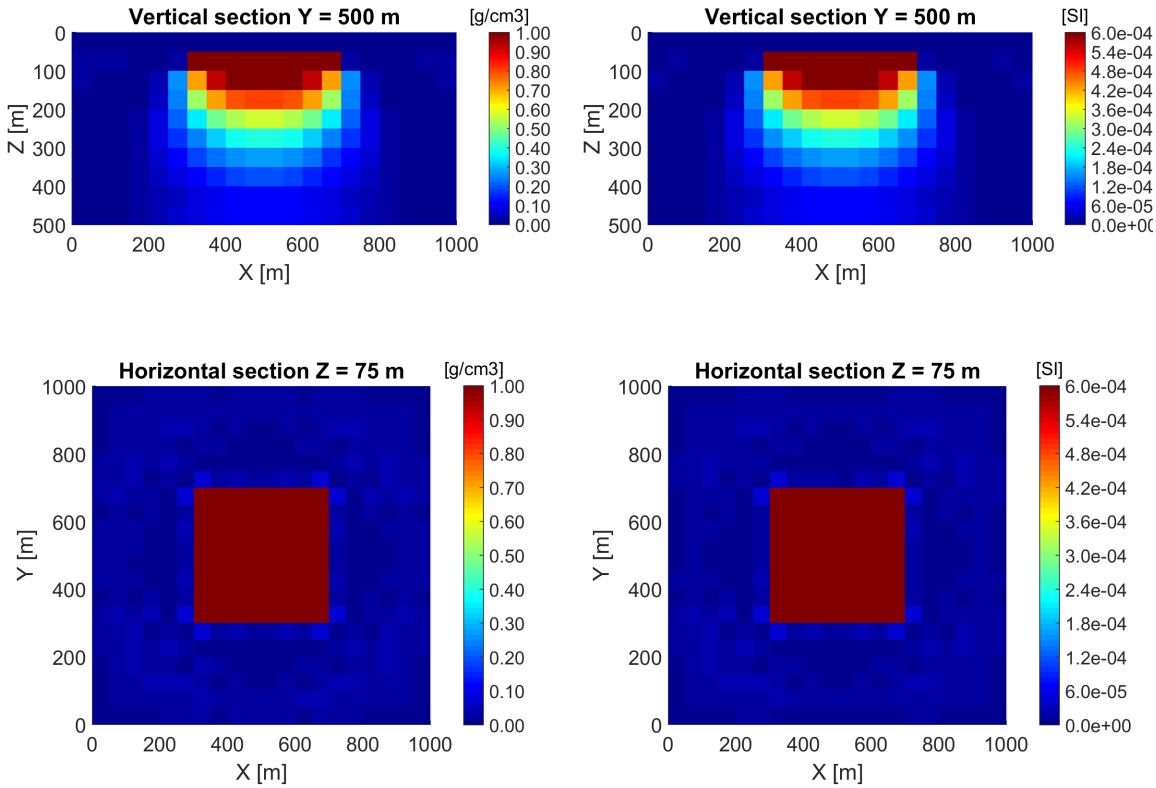

Figure 3.3. Model 1. The density (left panels) and magnetic susceptibility (right panels) of the block model recovered from the joint inversion. The vertical (top panels) and horizontal (bottom panels) sections are provided. The lower boundary of the anomaly in the recovered magnetic susceptibility model is improved compared to the results of the separate inversions.

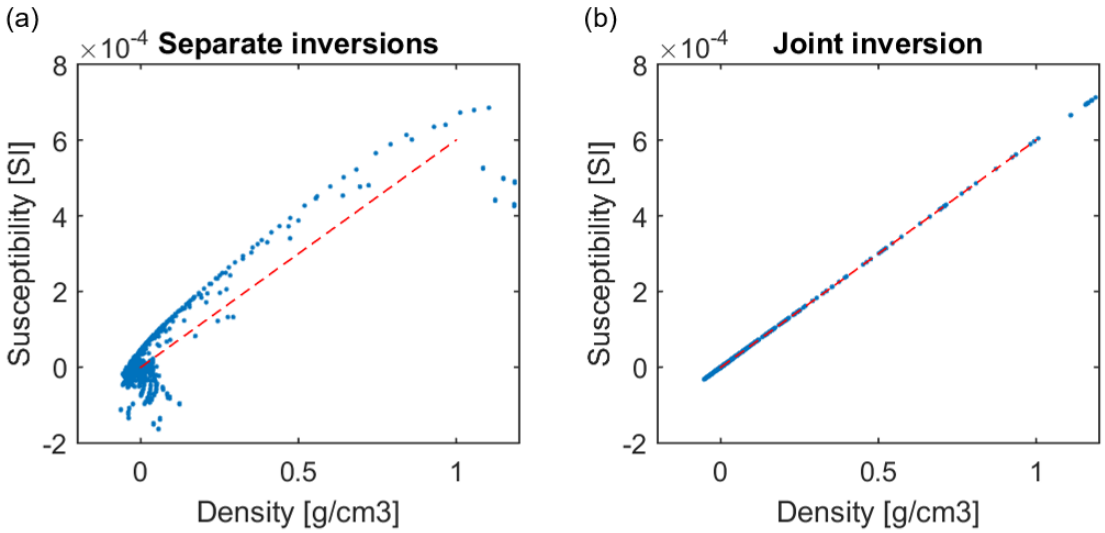

Figure 3.4. Model 1. Cross plots between the density and magnetic susceptibility derived from the (a) separate and (b) joint inversions. The true linear relationship between these two physical properties is represented by the dashed red line.

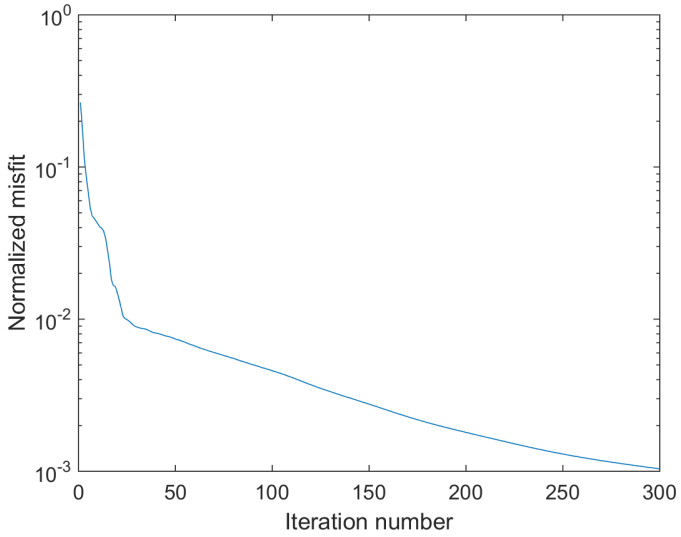

Figure 3.5. Model 1. A convergence plot of the normalized misfit vs. the iteration number of the joint inversion.

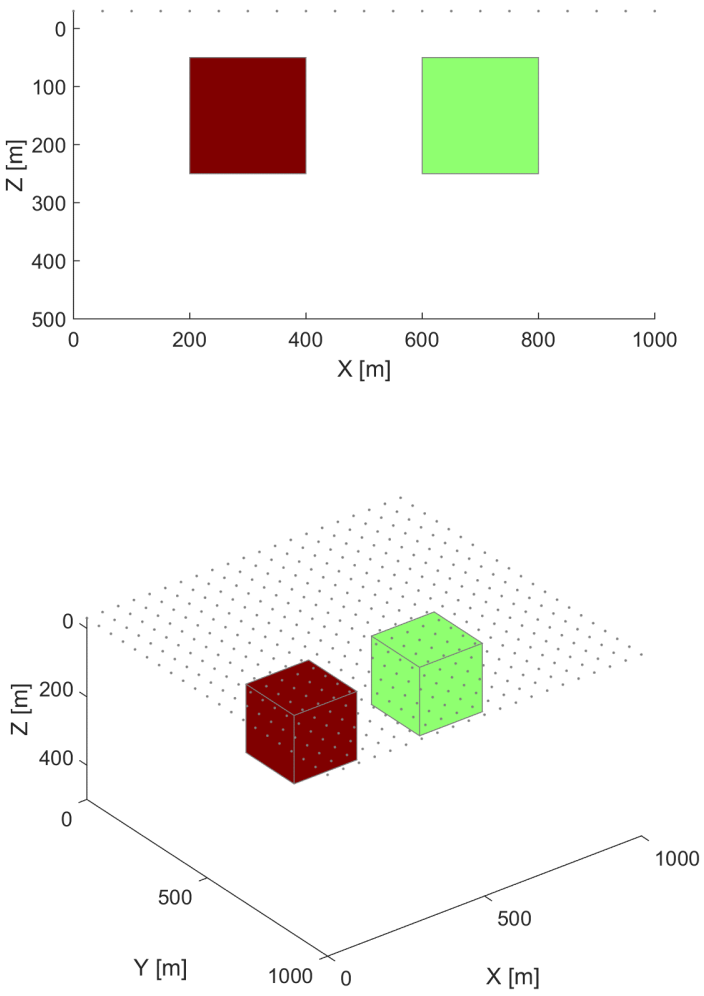

Figure 3.6. Model 2. Vertical (top) and 3D (bottom) views of the two-blocks model. The left block has a higher density and lower magnetic susceptibility than the right one. The gray dots indicate the positions of the receivers.

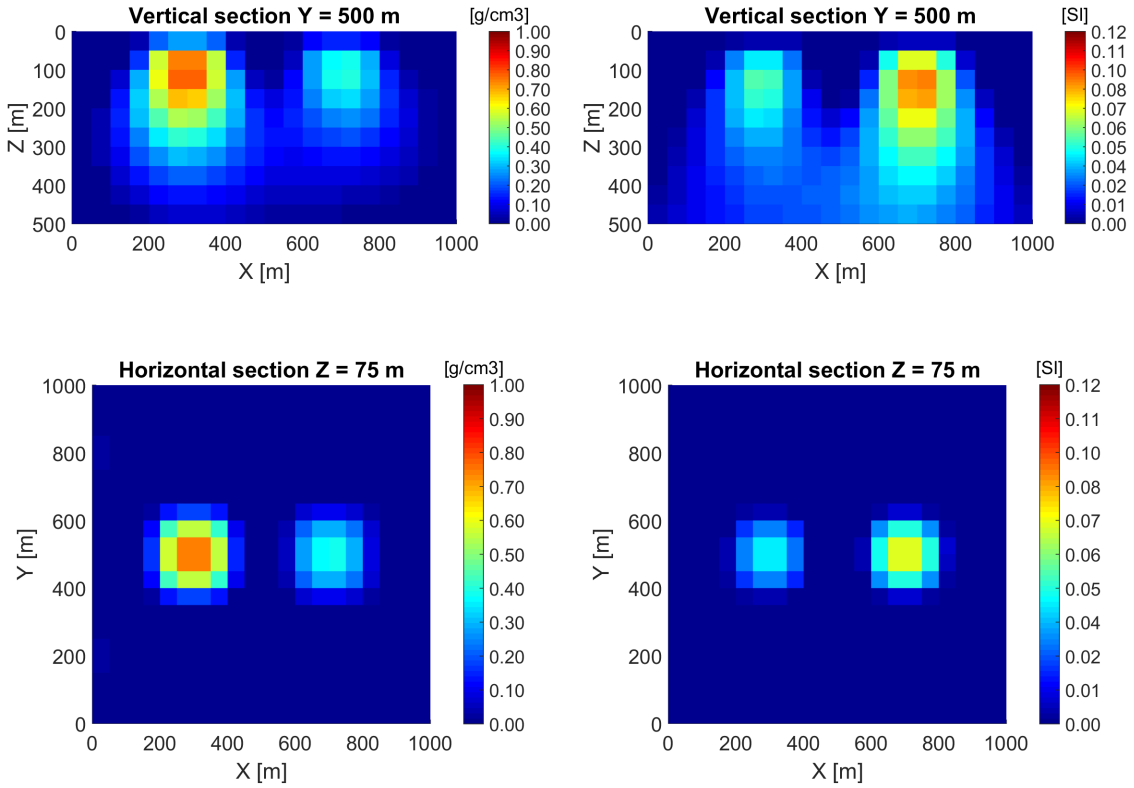

Figure 3.7. Model 2. The density (left panels) and magnetic susceptibility (right panels) of the two-blocks model recovered from the separate inversions. The vertical (top panels) and horizontal (bottom panels) sections are provided. Both the gravity and magnetic inversions recovered two anomalies reasonably well, resulting in a normalized misfit of 0.08.

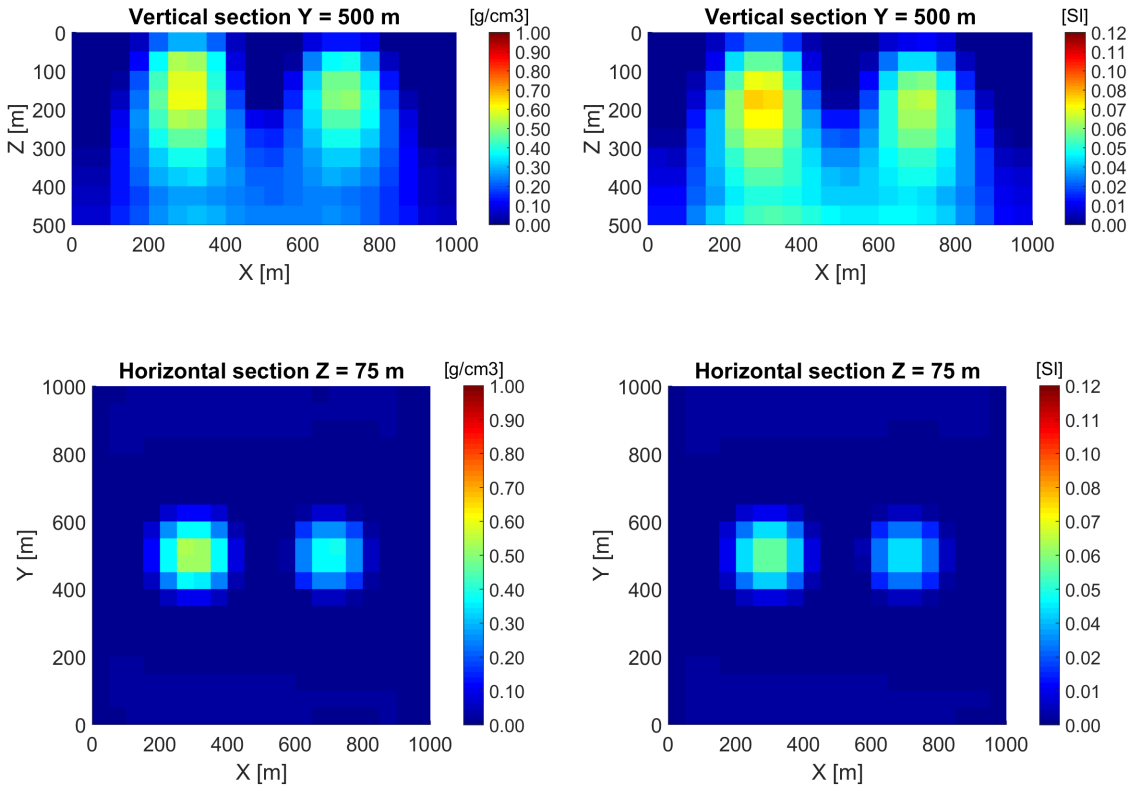

Figure 3.8. Model 2. The density (left panels) and magnetic susceptibility (right panels) of the two-blocks model recovered from the joint inversion. The vertical (top panels) and horizontal (bottom panels) sections are provided. Although the joint inversion recovered two anomalies, the magnitudes of the density and magnetic susceptibility anomalies are not correct, resulting in a normalized misfit of 0.28.

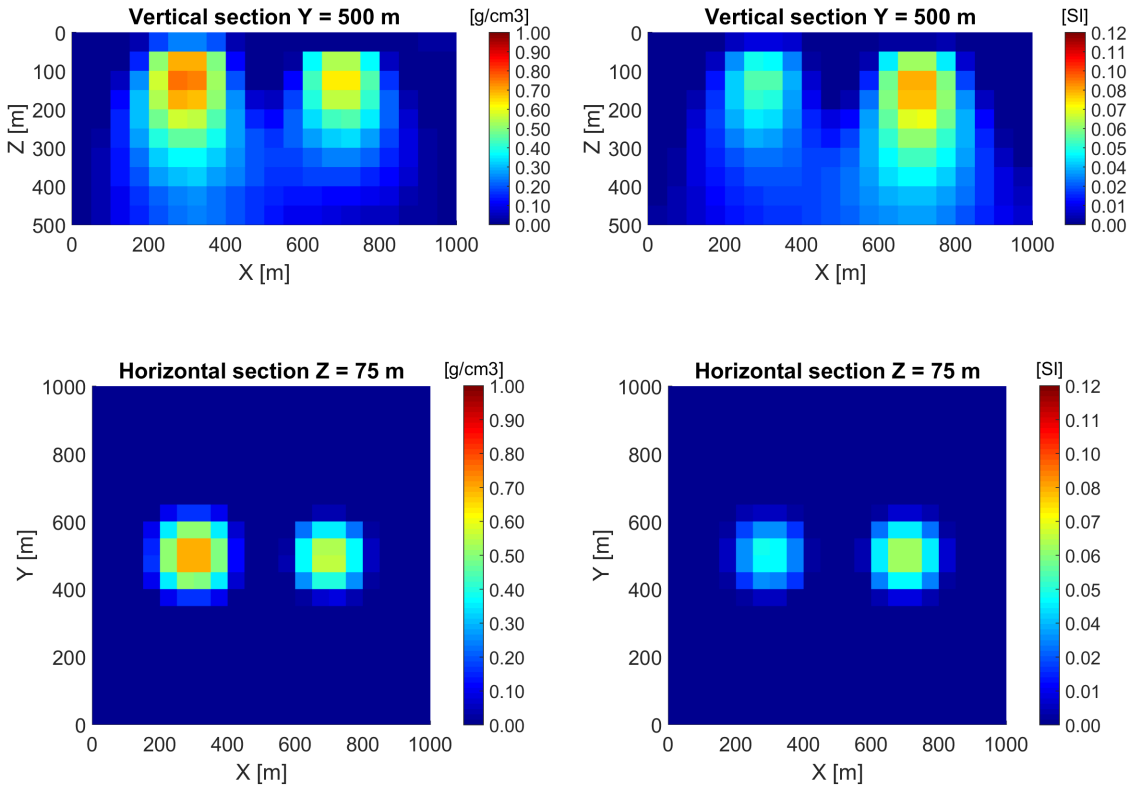

Figure 3.9. Model 2. The density (left panels) and magnetic susceptibility (right panels) of the two-blocks model recovered from the joint inversion with a decreased correlation parameter. The vertical (top panels) and horizontal (bottom panels) sections are provided. The magnitudes of the recovered density and magnetic susceptibility anomalies were improved, resulting in a normalized misfit of 0.11.

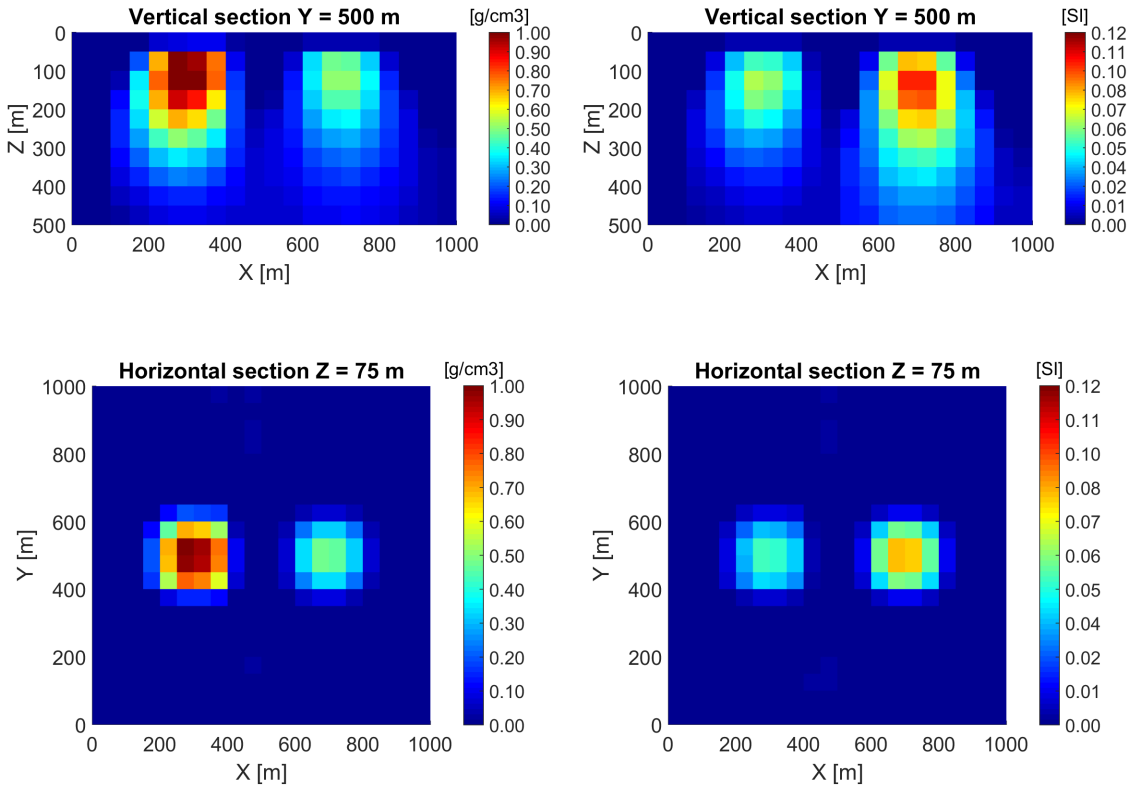

Figure 3.10. Model 2. The density (left panels) and magnetic susceptibility (right panels) of the two-blocks model recovered from the modified joint inversion with the localized Gramian constraints. The vertical (top panels) and horizontal (bottom panels) sections are provided. The recovered properties agree well with the true model, resulting in a normalized misfit of 0.06.

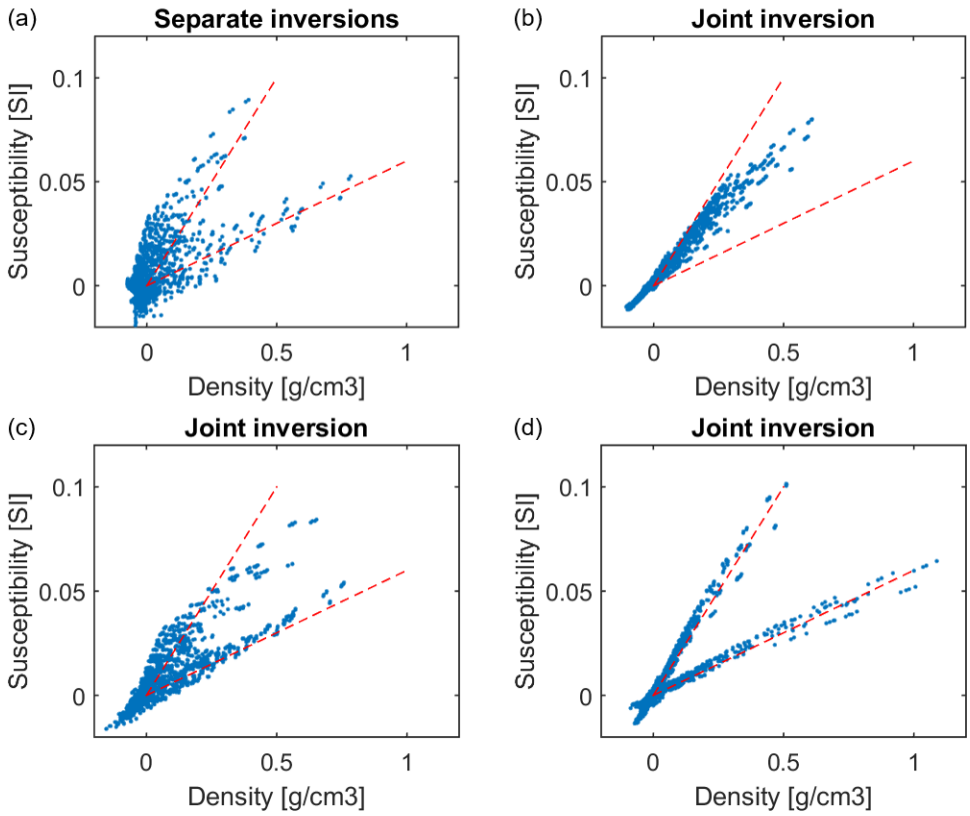

Figure 3.11. Model 2. Cross plots between the density and magnetic susceptibility derived from different inversions: (a) separate inversions; (b) joint inversion based on formula (2.18); (c) joint inversion based on formula (2.18) with a decreased correlation parameter; (d) joint inversion with the localized Gramian constraints. The dashed red lines represent the true linear relationships.

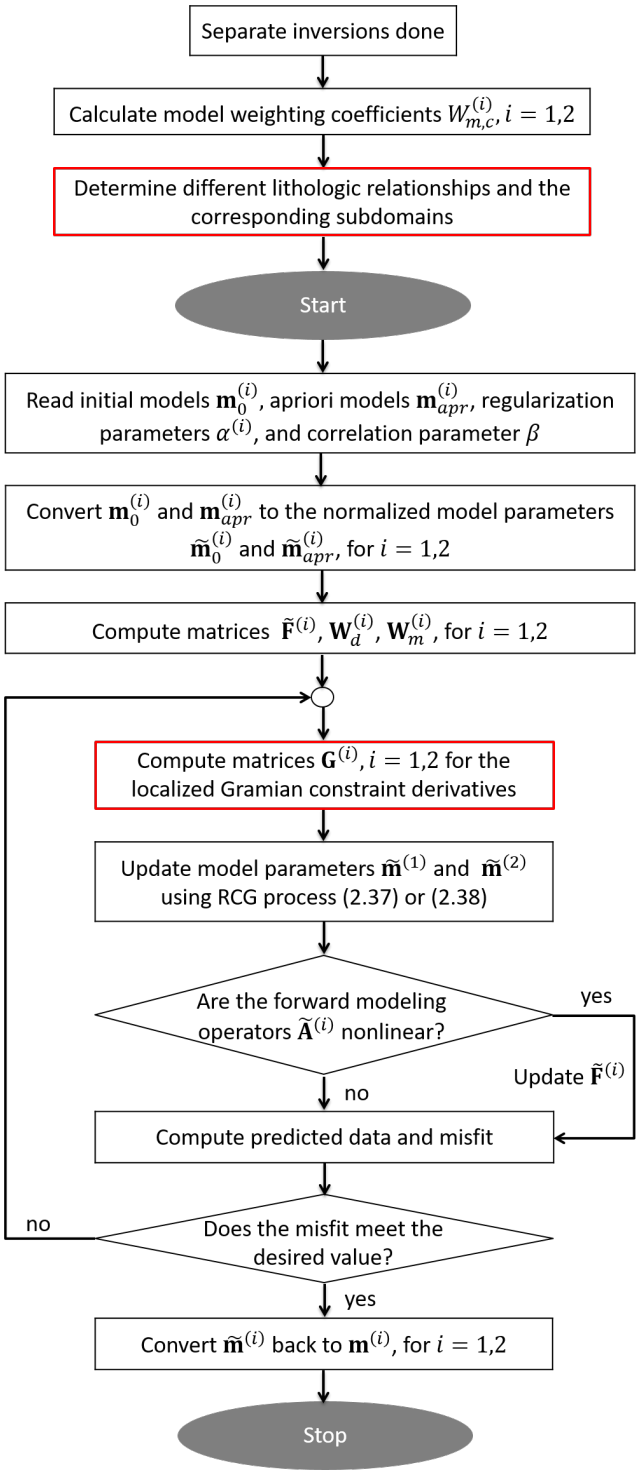

Figure 3.12. Flow chart showing the main steps of the joint inversion with the localized Gramian constraints. The red boxes emphasize the steps related to the localized Gramian constraints.

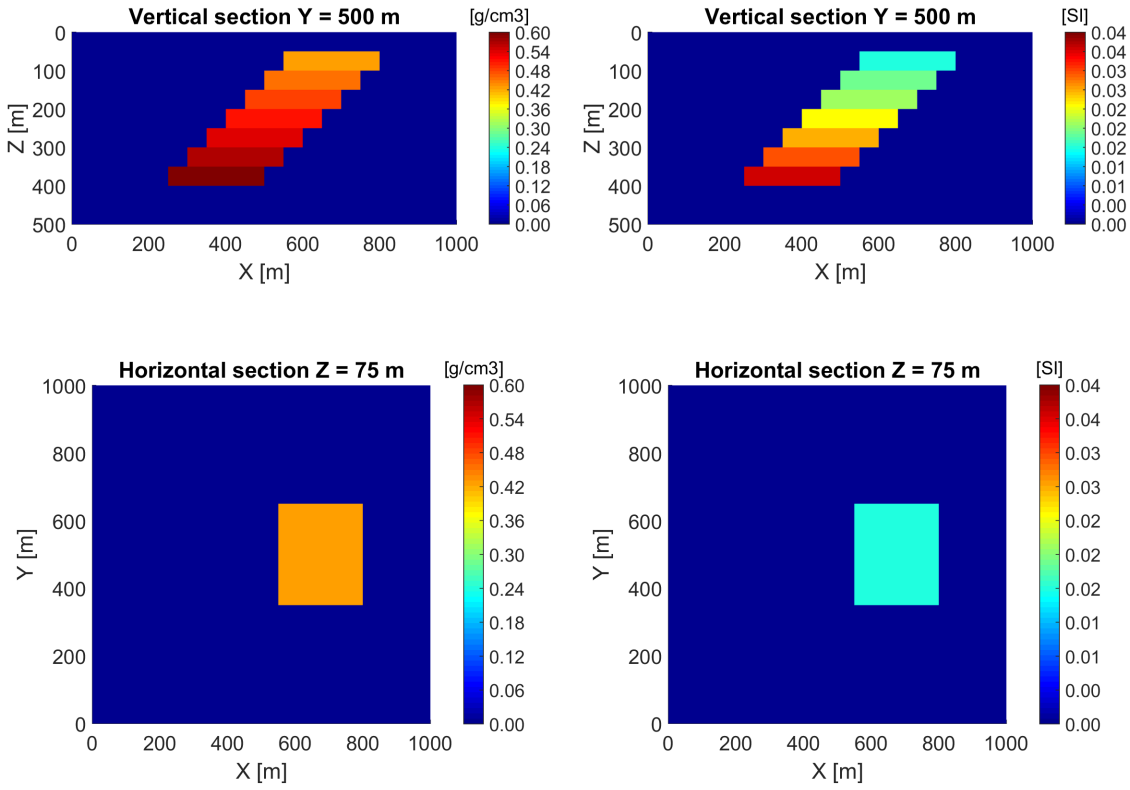

Figure 3.13. Model 3. The vertical (top panels) and horizontal (bottom panels) sections of the density (left panels) and magnetic susceptibility (right panels) distributions of the synthetic dike model.

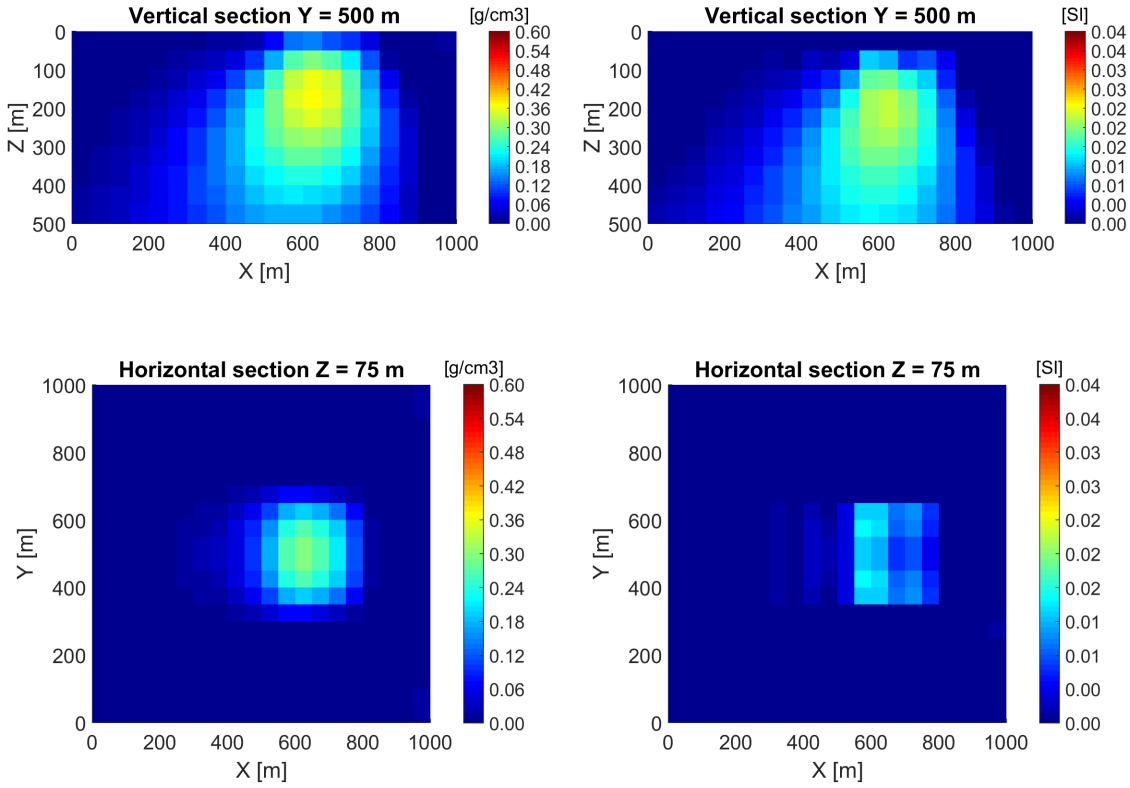

Figure 3.14. Model 3. The density (left panels) and magnetic susceptibility (right panels) of the dike model recovered from the separate inversions. The vertical (top panels) and horizontal (bottom panels) sections are provided.

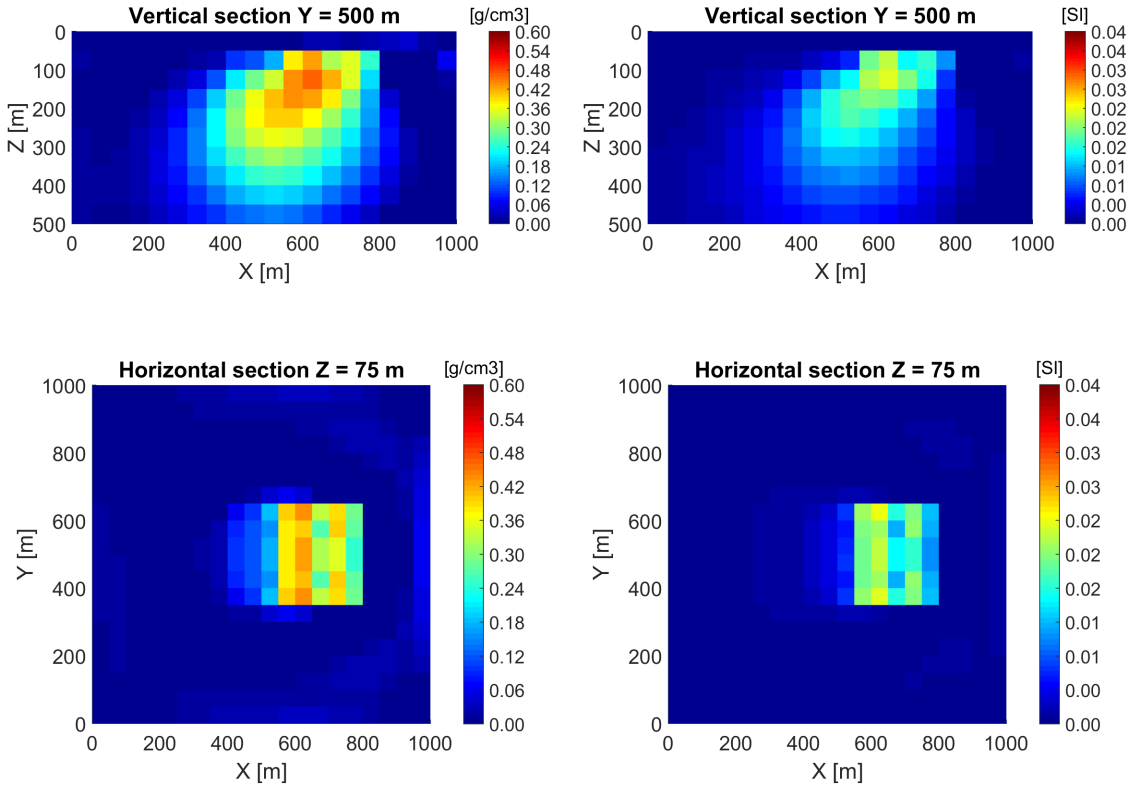

Figure 3.15. Model 3. The density (left panels) and magnetic susceptibility (right panels) of the dike model recovered from the joint inversions. The vertical (top panels) and horizontal (bottom panels) sections are provided.

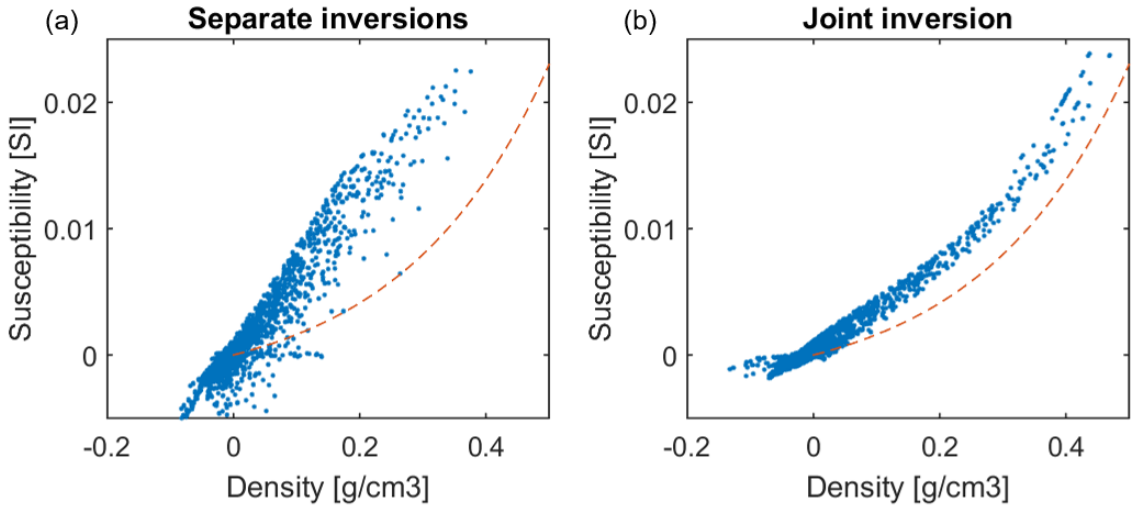

Figure 3.16. Model 3. Cross plots between the density and magnetic susceptibility derived from the (a) separate and (b) joint inversions. The dashed red line represents the true nonlinear relationship.

CHAPTER 4

MAGNETIZATION VECTOR INVERSION

Conventional 3D magnetic inversion methods are based on the assumption that there is no remanent magnetization, and the inversion is run for magnetic susceptibility only. However, this approach ignores the situation where the direction of magnetization of the rocks is different from the direction of the induced magnetic field. This situation happens in a case of remanent magnetization, typical for geologic structures such as kimberlites, dikes, iron-rich ultramafic pegmatitoids, platinum group element reefs, and banded iron formations. This chapter presents a novel method of inversion of magnetic data for the scalar components of the magnetization vector. The method is based on a new magnetic forward modeling algorithm, which uses triangular prisms of arbitrary shape in order to achieve a more accurate approximation of the topography. The inversion also includes Gramian constraints to correlate the magnetization vector components, in order to obtain a robust solution of otherwise ill-posed magnetic inverse problems. The method was successfully tested on a synthetic model of the magnetized dipping dike. Subsequent inversion of airborne magnetic data collected in the Northwest Territories of Canada demonstrated how inversion for the magnetization vector with Gramian constraints can improve the subsurface imaging of kimberlites.

4.1 Theory

4.1.1 Forward modeling

Most 3D inversion methods in use today have been developed for recovering a 3D magnetic susceptibility model from the magnetic vector field, **H**, or from the total magnetic intensity (TMI) data, **T**, assuming that there is no remanent magnetization (e.g., Li and Oldenburg, 1996, 2003; Portniaguine and Zhdanov, 2002; Čuma et al., 2012). However, it is well established that in many geological areas the direction of

magnetization in a rock differs from the direction of today's magnetic field, $\mathbf{H}_0$. This effect is manifested by the presence of the remanent magnetization in the rocks. To include both induced and remanent magnetization, one needs to model on three components of the magnetization vector rather than the scalar susceptibility. A variation of this approach was used by Lelièvre and Oldenburg (2009) to invert TMI data. This enables explicit inversion of the magnetization direction and amplitude, rather than just the magnetization amplitude only (e.g., Li et al., 2010). Recently, Ellis et al. (2012) reported further progress in the solution of this problem; they introduced a technique for regularized inversion for the magnetization vector. From the magnetization vector, one can recover information about both the remanent and induced magnetization.

For modeling the magnetic data, I discretize the 3D earth model into a grid of N_m cells, each of constant intensity of magnetization. Following Zhdanov (2002), the total magnetic intensity field, can be expressed in discrete form as follows:

$$\Delta T(\mathbf{r}') = -H_0 \sum_{k=1}^{N_m} \mathbf{l}(\mathbf{r}') \cdot \iiint_{V_k} \frac{1}{|\mathbf{r}-\mathbf{r}'|^3} \left(\mathbf{M}_k - \frac{3(\mathbf{M}_k \cdot (\mathbf{r}-\mathbf{r}'))(\mathbf{r}-\mathbf{r}')}{|\mathbf{r}-\mathbf{r}'|^2} \right) dv, \quad (4.1)$$

where $\mathbf{r}$ is the vector of a point within the source, $\mathbf{r}'$ is the vector of an observation point, and $\mathbf{M}_k = (M_{xk}, M_{yk}, M_{zk})$ is the magnetization vector of the k^{th} cell.

Consider a flat earth model and discretize the modeling domain into a set of rectangular prisms. One can compute the volume integral in equation (4.1) in closed form, as it was done in Bhattacharyya (1980) for magnetic susceptibility. One can also evaluate the volume integral numerically with sufficient accuracy using single-point Gaussian integration with pulse basis functions provided the depth to the center of the cell exceeds twice the dimension of the cell (Zhdanov, 2002):

$$\Delta T(\mathbf{r}') \approx -H_0 \sum_{k=1}^{N_m} \mathbf{l}(\mathbf{r}') \cdot \frac{1}{|\mathbf{r}-\mathbf{r}'|^3} \left(\mathbf{M}_k - \frac{3(\mathbf{M}_k \cdot (\mathbf{r}-\mathbf{r}'))(\mathbf{r}-\mathbf{r}')}{|\mathbf{r}-\mathbf{r}'|^2} \right) \Delta x \Delta y \Delta z, \quad (4.2)$$

where Δx, Δy, and Δz are the cell sizes in the x, y, and z directions, respectively.

However, the Earth's surface is usually not flat and may have a variable topography. In order to accurately represent the surface undulation, one needs to use the cells with more complex shapes. For this reason, I shift the top four vertices of a rectangular prism in the uppermost layer according to the true terrain height, as

shown in Figure 4.1. In this way, the rectangular prisms are still the elements in the modeling domain but with some cells distorted according to topography. Here, I present a detailed numerical algorithm to compute the following volume integral for an arbitrary k^{th} rectangular cell (either distorted or undistorted):

$$\Delta T_k(\mathbf{r}') = \iiint_{V_k} \Psi\big(\mathbf{r}-\mathbf{r}', \mathbf{M}_k\big) dv, \tag{4.3}$$

where the kernel function $\Psi\big(\mathbf{r}-\mathbf{r}', \mathbf{M}_k\big)$ is defined as follows:

$$\Psi\big(\mathbf{r}-\mathbf{r}', \mathbf{M}_k\big) = -H_0 \mathbf{l}(\mathbf{r}') \cdot \frac{1}{|\mathbf{r}-\mathbf{r}'|^3} \left(\mathbf{M}_k - \frac{3(\mathbf{M}_k \cdot (\mathbf{r}-\mathbf{r}'))(\mathbf{r}-\mathbf{r}')}{|\mathbf{r}-\mathbf{r}'|^2} \right). \tag{4.4}$$

I first split the k^{th} rectangular prism into four triangular prisms, as shown in Figure 4.1. So that

$$\Delta T_k(\mathbf{r}') = \sum_{j=1}^{4} \iiint_{V_k^j} \Psi\big(\mathbf{r}-\mathbf{r}', \mathbf{M}_k\big) dv. \tag{4.5}$$

Using the concept of isoparametric elements developed in the theory of finite element methods (Jin, 2014), the volume integration in equation (4.5) can be accomplished by transforming an arbitrarily shaped triangular prism in the xyz space into an orthogonal element in the $\xi\eta\zeta$ space, as shown in Figure 4.2. This transformation can be expressed as follows:

$$x = \sum_{i=1}^{6} N_i^e(\xi, \eta, \zeta) x_i, \tag{4.6}$$

$$y = \sum_{i=1}^{6} N_i^e(\xi, \eta, \zeta) y_i, \tag{4.7}$$

$$z = \sum_{i=1}^{6} N_i^e(\xi, \eta, \zeta) z_i, \tag{4.8}$$

where (x_i, y_i, z_i) is the coordinate of the i^{th} node of a triangular prism; N_i^e is the basis function obtained as follows:

$$N_i^e = \frac{1}{2}(1-\xi-\eta)(1+\zeta_i\zeta), i = 1, 4, \tag{4.9}$$

$$N_i^e = \frac{1}{2}\xi(1+\zeta_i\zeta), i = 2, 5, \tag{4.10}$$

$$N_i^e = \frac{1}{2}\eta(1+\zeta_i\zeta), i = 3, 6. \tag{4.11}$$

Now I can write the integral in equation (4.5) in the transformed $\xi\eta\zeta$ space,

$$\Delta T_k(x', y', z') = \sum_{j=1}^{4} \iiint_{V_k^j} \Psi\big(x, y, z, x', y', z', \mathbf{M}_k\big) dx dy dz$$

$$= \sum_{j=1}^{4} \iiint_{\Delta} \Psi_k^j\big(\xi, \eta, \zeta, x', y', z', \mathbf{M}_k\big) |\mathbf{J}|_k^j d\xi d\eta d\zeta, \tag{4.12}$$

where Δ denotes the orthogonal triangular prism in the $\xi\eta\zeta$ space. The indices j and k represent dependency on the j^{th} triangular prism in the k^{th} rectangular cell. The term $|\mathbf{J}|$ is the determinant of the matrix $\mathbf{J}$ defined as follows:

$$\mathbf{J} = \begin{bmatrix} \dfrac{\partial x}{\partial \xi} & \dfrac{\partial y}{\partial \xi} & \dfrac{\partial z}{\partial \xi} \\ \dfrac{\partial x}{\partial \eta} & \dfrac{\partial y}{\partial \eta} & \dfrac{\partial z}{\partial \eta} \\ \dfrac{\partial x}{\partial \zeta} & \dfrac{\partial y}{\partial \zeta} & \dfrac{\partial z}{\partial \zeta} \end{bmatrix}. \tag{4.13}$$

Following Martin et al. (2013), I use Gaussian quadrature to evaluate the integral over the orthogonal triangular prism in the $\xi\eta\zeta$ space in equation (4.12), as follows:

$$\Delta T_k(x', y', z') = \sum_{j=1}^{4} \iiint_{\Delta} \Psi_k^j\big(\xi, \eta, \zeta, x', y', z', \mathbf{M}_k\big) |\mathbf{J}|_k^j d\xi d\eta d\zeta \tag{4.14}$$

$$= \sum_{j=1}^{4} \sum_{p=1}^{N_p} W_p \Psi_k^j\big(\xi_p, \eta_p, \zeta_p, x', y', z', \mathbf{M}_k\big) \, |\mathbf{J}|_k^j \,, \tag{4.15}$$

where N_p is the number of Gaussian points and W_p are the p^{th} quadrature weights. Thus, I arrive at the expression for the total magnetic intensity in equation (4.1) based on numerical integration:

$$\Delta T = \sum_{k=1}^{N_m} \Delta T_k = \sum_{k=1}^{N_m} \sum_{j=1}^{4} \sum_{p=1}^{N_p} W_p \Psi_k^j\big(\xi_p, \eta_p, \zeta_p, x', y', z', \mathbf{M}_k\big) \, |\mathbf{J}|_k^j \,. \tag{4.16}$$

This approach can be extended to computing any potential fields and their derivatives by simply changing the kernel function Ψ.

4.1.2 Inverse problem formulation

In the paper by Zhu et al. (2014), the authors developed a method of direct inversion of the magnetic data for the magnetization vector in each cell. The results

presented in the cited paper illustrated the practical difficulties of this inversion related to the fact that in this case one has to determine three unknown components of the magnetization vector within each cell instead of one unknown value of susceptibility. The main problem was with the increased practical nonuniqueness associated with this inverse problem. However, there is inherent correlation between the different components of the magnetization vector. The three scalar components have similar spatial variations and represent the same zones of anomalous magnetization. Therefore, it is possible to expect that the different components of the magnetization vector should be mutually correlated.

It was demonstrated in the paper by Zhdanov et al. (2012) that one can enforce a correlation between different model parameters by using Gramian constraints. Following the cited paper, I have included three Gramian constraints in the parametric functional as follows:

$$P(\mathbf{m}) = \|\mathbf{W}_d\left(\mathbf{Am}-\mathbf{d}\right)\|^2 + \alpha\|\mathbf{W}_m(\mathbf{m}-\mathbf{m}_{apr})\|^2 + \beta\sum_{\gamma=x,y,z} S_G(\mathbf{M}_\gamma, \chi_{\mathit{eff}}), \quad (4.17)$$

where $\mathbf{m}$ is the $3N_m$ length vector of magnetization vector components; $\mathbf{M}_\gamma$ is the N_m length vector of the γ component of magnetization vector, $\gamma = x, y, z$; χ_{eff} is the N_m length vector of the effective magnetic susceptibility, defined as the magnitude of the magnetization vector:

$$\chi_{\mathit{eff}} = \sqrt{\mathbf{M}_x^2 + \mathbf{M}_y^2 + \mathbf{M}_z^2}\ ; \quad (4.18)$$

and S_G is the Gramian constraint:

$$S_G(\mathbf{M}_\gamma, \chi_{\mathit{eff}}) = \begin{vmatrix} \langle \mathbf{M}_\gamma, \mathbf{M}_\gamma \rangle & \langle \mathbf{M}_\gamma, \chi_{\mathit{eff}} \rangle \\ \langle \chi_{\mathit{eff}}, \mathbf{M}_\gamma \rangle & \langle \chi_{\mathit{eff}}, \chi_{\mathit{eff}} \rangle \end{vmatrix}, \gamma = x, y, z. \quad (4.19)$$

Using the Gramian constraint (4.19), I enhance a direct correlation between the scalar components of the magnetization vector with χ_{eff}, which is computed at the previous iteration of an inversion and is updated on every iteration. The advantage of using the Gramian constraint in equation (4.19) is that it does not require a priori knowledge of the magnetization vector, e.g., direction, dominant component, etc.

One may consider minimizing a different parametric functional as follows:

$$P(\mathbf{m}) = \|\mathbf{W}_d\left(\mathbf{Am}-\mathbf{d}\right)\|^2 + \alpha\|\mathbf{W}_m(\mathbf{m}-\mathbf{m}_{apr})\|^2$$

$$+\beta\Big(S_G(\mathbf{M}_x,\mathbf{M}_y)+S_G(\mathbf{M}_x,\mathbf{M}_z)+S_G(\mathbf{M}_y,\mathbf{M}_z)\Big). \tag{4.20}$$

Formula (4.20) enhances a correlation between the three components of the magnetization vector without using the intermediate parameter of effective magnetic susceptibility. However, this approach may not work as expected sometimes. It is possible that all three components recovered after the initial iteration of an inversion deviate from the true solutions. In the later iterations, such deviations will not vanish because the correlation is between the distorted components. This problem can be diminished by correlating each component with the effective magnetic susceptibility, as done in formula (4.17), since the magnitude of the magnetization vector is more reliable than the individual scalar components. Thus, I suggest using formula (4.17) instead of formula (4.20) when solving for the magnetization vector.

Minimization problem (4.17) can be solved using a variety of optimization methods. For improved convergence and to avoid any matrix inversions, I minimize equation (4.17) using the regularized conjugate gradient (RCG) method. The iterative process of the RCG method is summarized as follows:

$$\mathbf{r}_n = \mathbf{Am}_n - \mathbf{d}, \tag{4.21a}$$

$$\mathbf{l}_n = \mathbf{F}^\top\mathbf{W}_d^2\mathbf{r}_n + \alpha\mathbf{W}_m^2\left(\mathbf{m}_n-\mathbf{m}_{apr}\right) + \beta\mathbf{G}\widetilde{\mathbf{m}}_n, \tag{4.21b}$$

$$\tilde{\mathbf{l}}_n = \mathbf{l}_n + \frac{\|\mathbf{l}_n\|^2}{\|\mathbf{l}_{n-1}\|^2}\tilde{\mathbf{l}}_{n-1},\ \tilde{\mathbf{l}}_0 = \mathbf{l}_0, \tag{4.21c}$$

$$\tilde{k}_n = \frac{\tilde{\mathbf{l}}_n^\top\mathbf{l}_n}{\tilde{\mathbf{l}}_n^\top\left(\mathbf{F}^\top\mathbf{W}_d^2\mathbf{F}+\alpha\mathbf{W}_m^2+\beta\mathbf{G}\right)\tilde{\mathbf{l}}_n}, \tag{4.21d}$$

$$\mathbf{m}_{n+1} = \mathbf{m}_n - \tilde{k}_n\tilde{\mathbf{l}}_n. \tag{4.21e}$$

The Fréchet derivative matrix $\mathbf{F}$ is identical to the operator $\mathbf{A}$, since the magnetic forward modeling is a linear problem. The matrix $\mathbf{G}$ is computed as follows:

$$\mathbf{G} = \begin{bmatrix} \mathbf{G}_x & & \\ & \mathbf{G}_y & \\ & & \mathbf{G}_z \end{bmatrix}, \tag{4.22}$$

where $\mathbf{G}_x$, $\mathbf{G}_y$, and $\mathbf{G}_z$ are the partial derivative matrices of the Gramian constraints in expression (4.17) with respect to $\mathbf{M}_x$, $\mathbf{M}_y$ and $\mathbf{M}_z$, respectively:

$$\mathbf{G}_\gamma = \left(\chi_{\mathit{eff}}\right)^\top \left(\chi_{\mathit{eff}}\right)\mathbf{I} - \left(\chi_{\mathit{eff}}\right)\left(\chi_{\mathit{eff}}\right)^\top, \gamma = x, y, z. \tag{4.23}$$

Note that, I treat χ_{eff} as a semiconstant variable. That is, its value is updated in the iterative process (4.21), but its derivatives with respect to $\mathbf{M}_x$, $\mathbf{M}_y$, and $\mathbf{M}_z$ are considered to be zeros. This holds when the change of the model parameter is relatively small between the iterations.

As usual, the iterative process (4.21) is terminated when the misfit reaches the required level δ_d:

$$\Phi\left(\mathbf{m}_{n+1}\right) = \left\|\mathbf{r}_{n+1}\right\|^2 = \delta_d. \tag{4.24}$$

4.2 Model study

4.2.1 A magnetized dipping dike

Let us consider a dipping dike with a magnetization opposite to the inducing field. The dike has a horizontal dimension of 250 m by 300 m and extends vertically from 50 m to 400 m as shown in Figure 4.3. The dike has a constant magnetization with a magnitude of 0.06 SI. The three components of the magnetization vector $\mathbf{M}$ are given as follows:

$$\begin{aligned} M_x &= -6.6 \times 10^{-3}, \\ M_y &= \ \ 1.4 \times 10^{-2}, \\ M_z &= -5.8 \times 10^{-2}. \end{aligned}$$

There are 441 surface receivers covering an area of 1 km by 1 km with a horizontal spacing of 50 m by 50 m. The parameters of the inducing magnetic field were selected as follows: $H_0 = 50\ 000$ nT, $I = 75°$, and $D = 25°$. The synthetic observed magnetic data were computed using a rectangular discretization according to formula (4.2),

since no topography was considered in this model. The TMI field and H_x, H_y and H_z components produced by the dipping dike are shown in Figure 4.4. Note that, formulas for H_x, H_y and H_z components can be obtained from equation (4.4) by simply directing vector $\mathbf{l}(\mathbf{r}')$ along the x, y, and z directions.

I inverted for the magnetization vector using both TMI and three magnetic components. The recovered magnetization using only minimum norm stabilizer and using both minimum norm and Gramian constraints are shown in Figures 4.5 and 4.6. By using the Gramian constraints, I was able to recover a model, which has a magnitude of magnetization and a shape close to the true model. I also found artifacts associated with M_x and M_y components using only the minimum norm stabilizer. These artifacts were greatly reduced in the inversion using both the minimum norm stabilizer and the Gramian constraints.

4.3 Case study: Kimberlite exploration in the Northwest of Canada

4.3.1 Regional geology

I present a case study of the inversion of airborne magnetic data in the Diavik Diamond Mine area. The Diavik Diamond Mine area is located near Lac de Gras in the central part of the Slave Structural Province, which forms a distinct cratonic block within the Canadian Precambrian Shield (Roscoe and Postle, 2005; Yip, 2008; Yip and Thompson, 2015). The Slave craton contains deformed and metamorphosed, Archean aged metaturbidite and lesser metavolcanic rocks of the Yellowknife Supergroup. These supracrustal rocks have been intruded by extensive Archean granitoids, and are in turn intruded by undeformed, late Archean granites and diabase dike swarms. Figure 4.7 presents a regional geology map showing the Slave Structural Province.

Structurally, the Slave craton is dominated by Proterozoic faulting and emplacement of several sets of diabase dikes (Stubley, 1998). Some of the dikes may have played a role in the structural ground preparation that allowed for the emplacement and localization of the kimberlite pipes in the region. The Slave Geological Province maybe divided into east and west domains. The west domain represents older thicker and more resistive lithosphere than the east domain that underlies the Lac de Gras

area. Based on exploration record, the east Slave area has been more productive in kimberlite exploration. Most reported diamondiferous kimberlite pipes found in the Slave Province are relatively small compared to kimberlite occurrences worldwide. They generally have a surface area of about five acres (about 20,000 m^2). The Diavik pipes have similar dimensions.

4.3.2 Local geology

Stubley (1998) reported three main Archean lithologies in the Lac de Gras area, including greywacke-mudstone metaturbidites (metamorphosed sedimentary rocks), biotite hornblende tonalite to quartz diorite (felsic to imtermediate rocks), and two-mica or K-spar porphyritic granite and granodiorite (felsic rocks), as shown in Figure 4.8. The area of the kimberlite pipes in Diavik is underlain by late Archean (2.5 to 2.8 billion years) muscovite-biotite granites (Roscoe and Postle, 2005). Proterozoic diabase dikes have been traced on the Diavik property by airborne and ground magnetic surveys. These dikes have blocky fracture and joint pattern that may provide permeable channels for groundwater.

Kimberlites are heterogeneous alkali ultramafic rocks exhibiting a wide variety of textures, including matrix-to-clast ratios, matrix alteration (serpentinization, clay alteration), and often containing country rock inclusions, mantle xenoliths and xenocrysts of various unique mineral phases including diamond. The Diavik kimberlites are Eocene in age (54 to 58 million years) and were formed by volcanic surface eruptions and near-surface injections of kimberlite magma and volcaniclastic debris into the granitic country rocks and into mid-Cretaceous to Tertiary mudstones. These latter formations covered the Archean basement at the time of kimberlite emplacement but have since been entirely eroded from the area.

4.3.3 Properties of kimberlites

Diamonds are included as xenocrysts in kimberlite magmas as they form and ascend through the upper mantle and crust. As the kimberlite magmas approach the surface, they degas and erupt explosively, forming the characteristic carrot-shaped diatreme. Abundant kimberlite is erupted as pyroclastic ejecta and falls both within

and adjacent to the pipe. The diatreme is filled with a combination of pyroclastic kimberlite, hypabyssal kimberlite, and in the case of the Lac de Gras pipes, Cretaceous mudstone that slumped back into the pipe. At Lac de Gras, the tops of the pipes were removed by continental glaciation. The kimberlites, being softer than the surrounding rocks, tended to form depressions which, after the glaciers retreated, filled with water to become small lakes. When pipes occur under larger lakes, such as Lac de Gras, the pipes typically lie beneath small depressions on the lake bottom.

The diamondiferous kimberlite pipes at Diavik intrude the granitic rocks and metaturbidites of the Slave craton. A typical kimberlite pipe has the shape of a carrot and can be subdivided from the top to bottom into crater, diatreme, and hypabysal facies kimberlite (Power and Hildes, 2007), as shown in Figure 4.9. Crater facies kimberlite is a mixture of tuffaceous kimberlite, surrounding country rock and overlying sediments. In much of the Slave Craton, crater facies kimberlite includes a significant component of shale and mudstone, sometimes with a significant component of entrained organic material. A crater facies kimberlite is often deeply weathered and serpentinized. Diatreme facies describe an explosive kimberlite breccia composed of fine-grained kimberlite, mantle nodules and angular fragments of the surrounding country rock. Diatreme facies rocks are generally confined to a central breccia pipe and are generally less altered than crater facies rocks. Hypabyssal kimberlite consists of unaltered fine-grained kimberlite with mantle nodules and rare fragments of country rock. Hypabyssal kimberlite bodies include dikes, blind intrusions and the root zones of kimberlite pipes.

Early exploration of the Diavik property consisted of airborne geophysical surveys and sampling of glacial till for diamond indicator minerals such as garnets, chromite and ilmenite. Targets were followed up by small-diameter core drilling. This work led to the discovery of a number of kimberlite pipes, which were further tested by small- and large-diameter core drilling. It shows that kimberlites have generally higher magnetic susceptibility than surrounding gneisses and granites and are additionally prone to retain remnant magnetization. As a result, magnetic anomalies are always associated with kimberlite pipes. The electrical resistivity, seismic velocity and density of kimberlites increase with depth from crater facies through hypabyssal facies.

4.3.4 Airborne magnetic survey

The airborne magnetic survey covers an area of 8 km by 7 km with an average flights height of 33 m. There are 103 flight lines with a line spacing of 75 m. The inducing magnetic field in the survey area has a strength of 59 000 nT with inclination and declination around 80° and 15°, respectively. Figure 4.10 shows the observed TMI field, which were obtained by subtracting the intensity of the inducing field from the original data. The airborne magnetic data in the survey area are characterized by a significant positive background field. For a better characterization of the weak anomaly of the magnetic susceptibility typical for kimberlites, I approximated the regional background TMI field, associated with the country rocks, with a third order polynomial and subtracted it from the observed TMI data. Figure 4.11 shows the map of the residual TMI anomaly.

The kimberlites in this area have been characterized by strong remanent magnetization, which require the inversion for the magnetization vector instead of the scalar magnetic susceptibility. I have applied the developed inversion algorithm based on both minimum norm stabilizer and Gramian constraints to a subset of the field airborne magnetic data collected in this area for kimberlite exploration. I have also taken into account of the terrain heights in constructing the inversion domain.

4.3.5 Inversion results

The subset of the residual TMI data shown in Figure 4.11 was inverted for a magnetization vector using both the minimum norm and Gramian stabilizers. A set of triangular prisms was used to better represent the topography in the uppermost layer of the inversion domain. I shifted the top four vertices of the rectangular prisms in the uppermost layer of the inversion domain to represent the actual terrain heights. These rectangular prisms were further divided into the triangular prisms for a better modeling of the topography.

Figures 4.12 to 4.14 show horizontal and vertical sections of the magnitude and scalar components of the magnetization vectors obtained by the inversion. Using both the minimum norm and Gramian stabilizers in the inversion, I was able to enhance a correlation between the different components and recover a higher intensity of mag-

netization in the target area. Basically, the kimberlite deposits are associated with the round anomalies having a dominant negative M_z component and less dominant M_x and M_y components. The elongated anomalies along the northeast-southwest direction are the magnetic dikes, which also have a dominant M_z component but are with a positive sign.

For comparison, the inversion results obtained by using only the minimum norm stabilizer are also provided in Figures 4.12 to 4.14. One can see the artifacts in the images of the M_x and M_y components in the locations of the kimberlite pipes as well as the magnetic dikes. These artifacts were greatly reduced by using the Gramian constraints in the inversion.

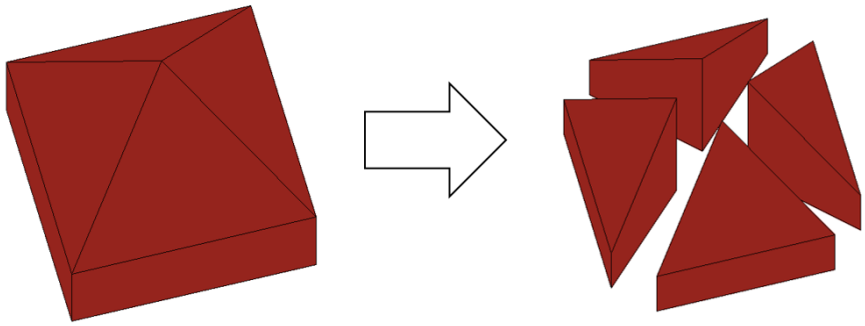

Figure 4.1. An example of a distorted rectangular prism (left) and the corresponding four triangular prisms (right).

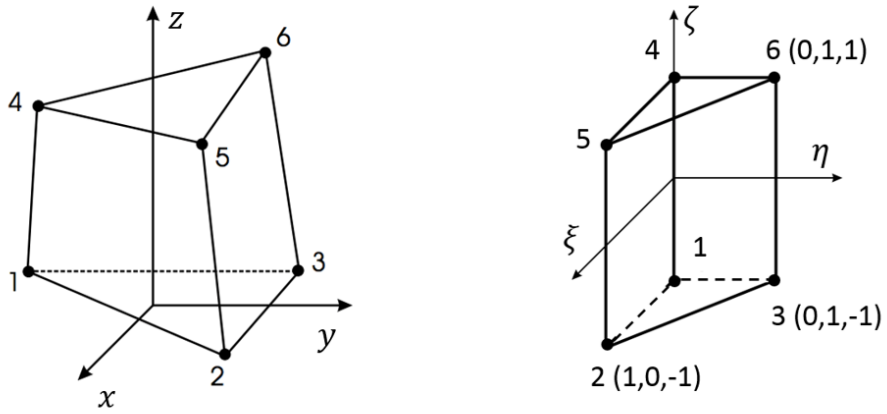

Figure 4.2. An arbitrarily shaped triangular prism in the xyz space (left) and the orthogonal element in the $\xi\eta\zeta$ space (right), with $\xi \in [0, 1]$, $\eta \in [0, 1]$, and $\zeta \in [-[1, 1]$.

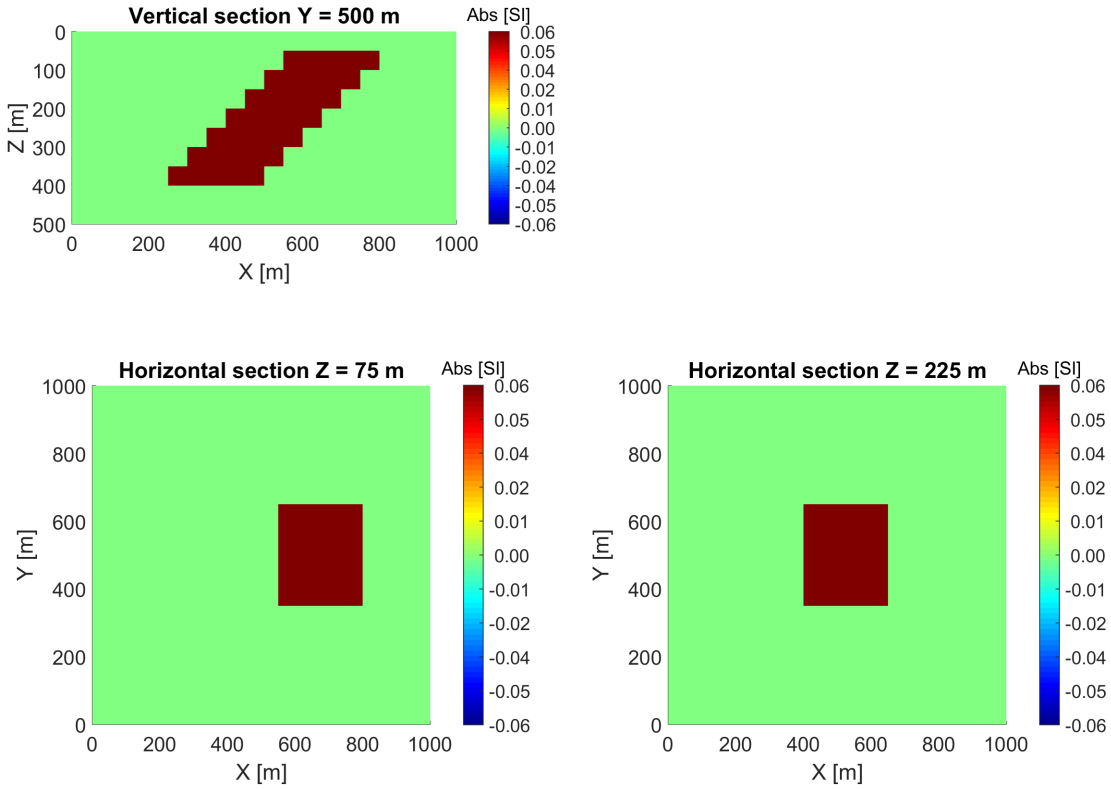

Figure 4.3. Model 1: A magnetized dipping dike. The magnitude of magnetization is 0.06 SI. The dike has a horizontal dimension of 250 m x 300 m and extends from 50 m to 400 m in depth.

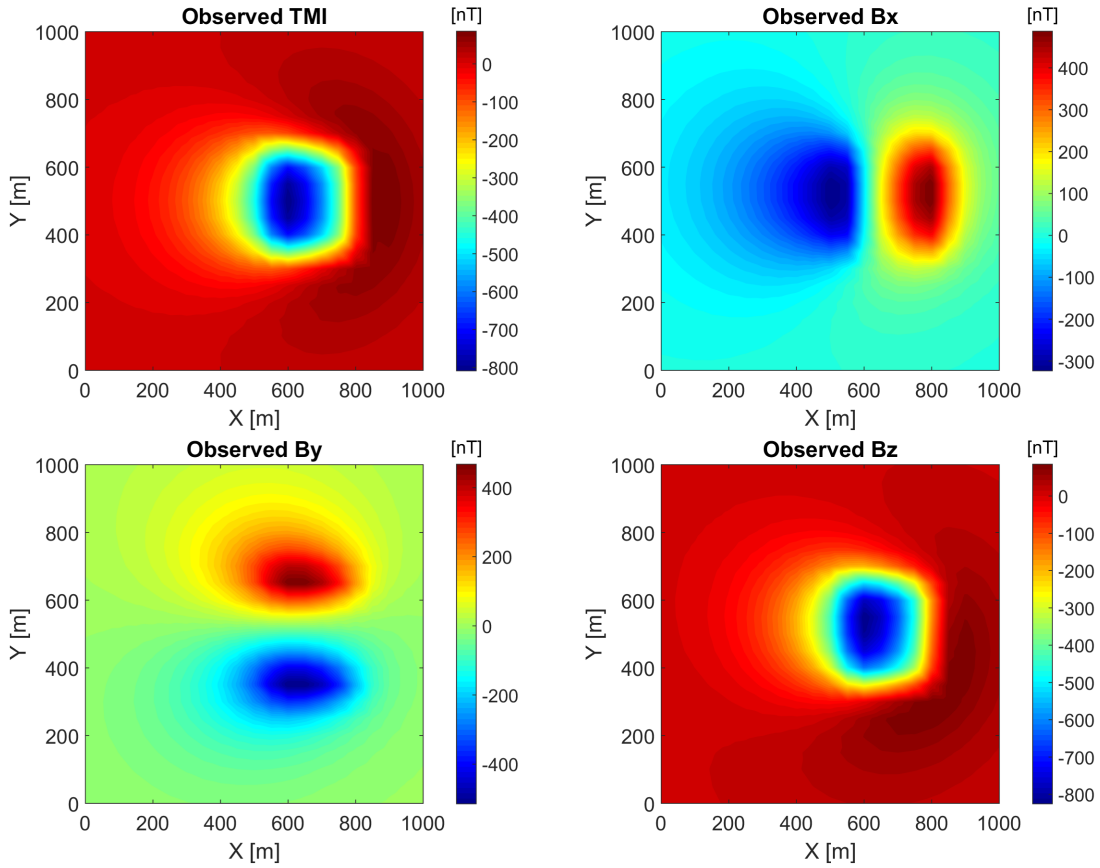

Figure 4.4. Model 1. Maps of the TMI field and H_x, H_y, and H_z components, produced by the dike model.

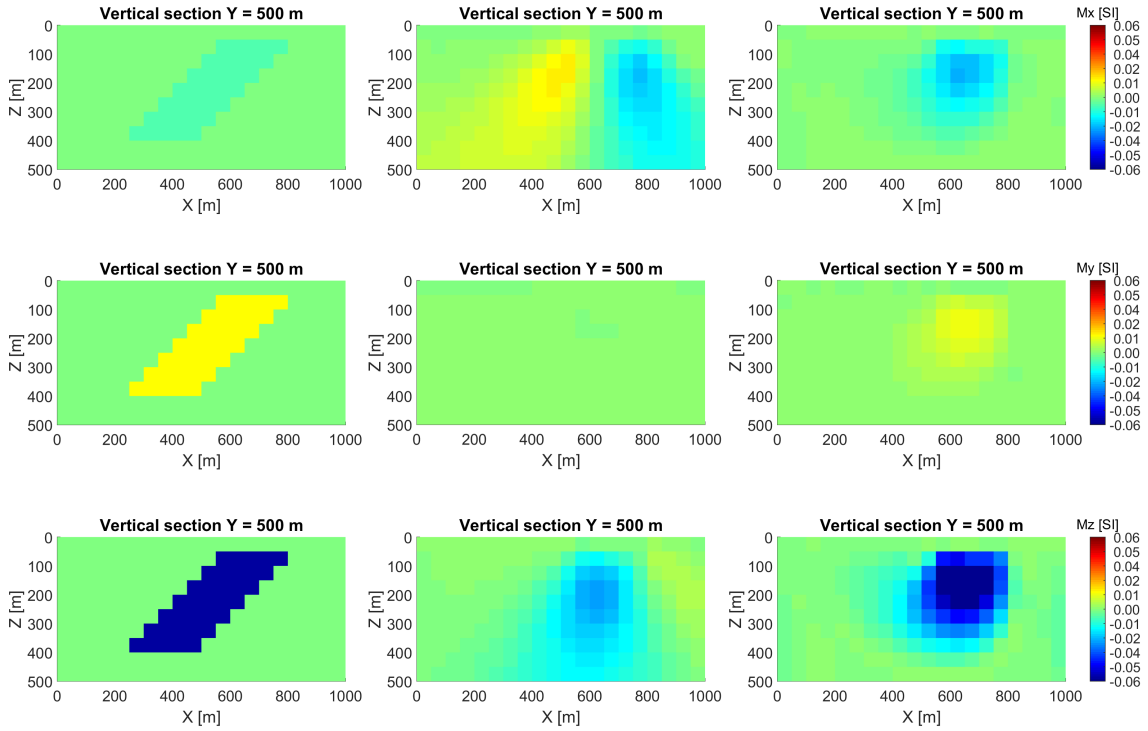

Figure 4.5. Model 1. Vertical sections of the recovered scalar components of the magnetization vector, which are M_x, M_y, and M_z from the top to the bottom, respectively. The inversion results using only the minimum norm stabilizer (second column) and using both the minimum norm stabilizer and the Gramian constraints (third column) are provided. The first column shows the scalar components of the magnetization vector of the true model.

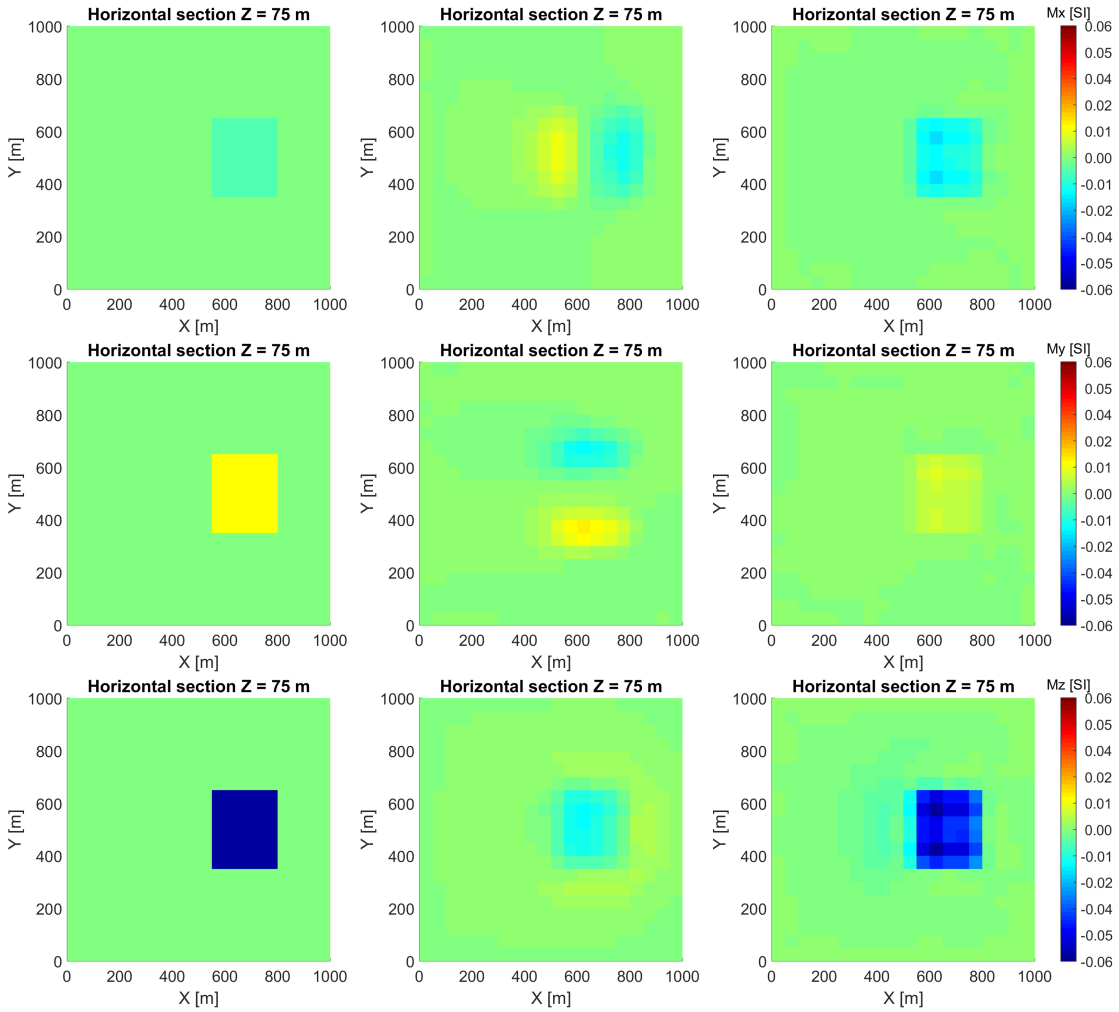

Figure 4.6. Model 1. Horizontal sections of the recovered scalar components of the magnetization vector. The inversion results using only the minimum norm stabilizer (second column) and using both the minimum norm stabilizer and the Gramian constraints (third column) are provided. The first column shows the scalar components of the magnetization vector of the true model.

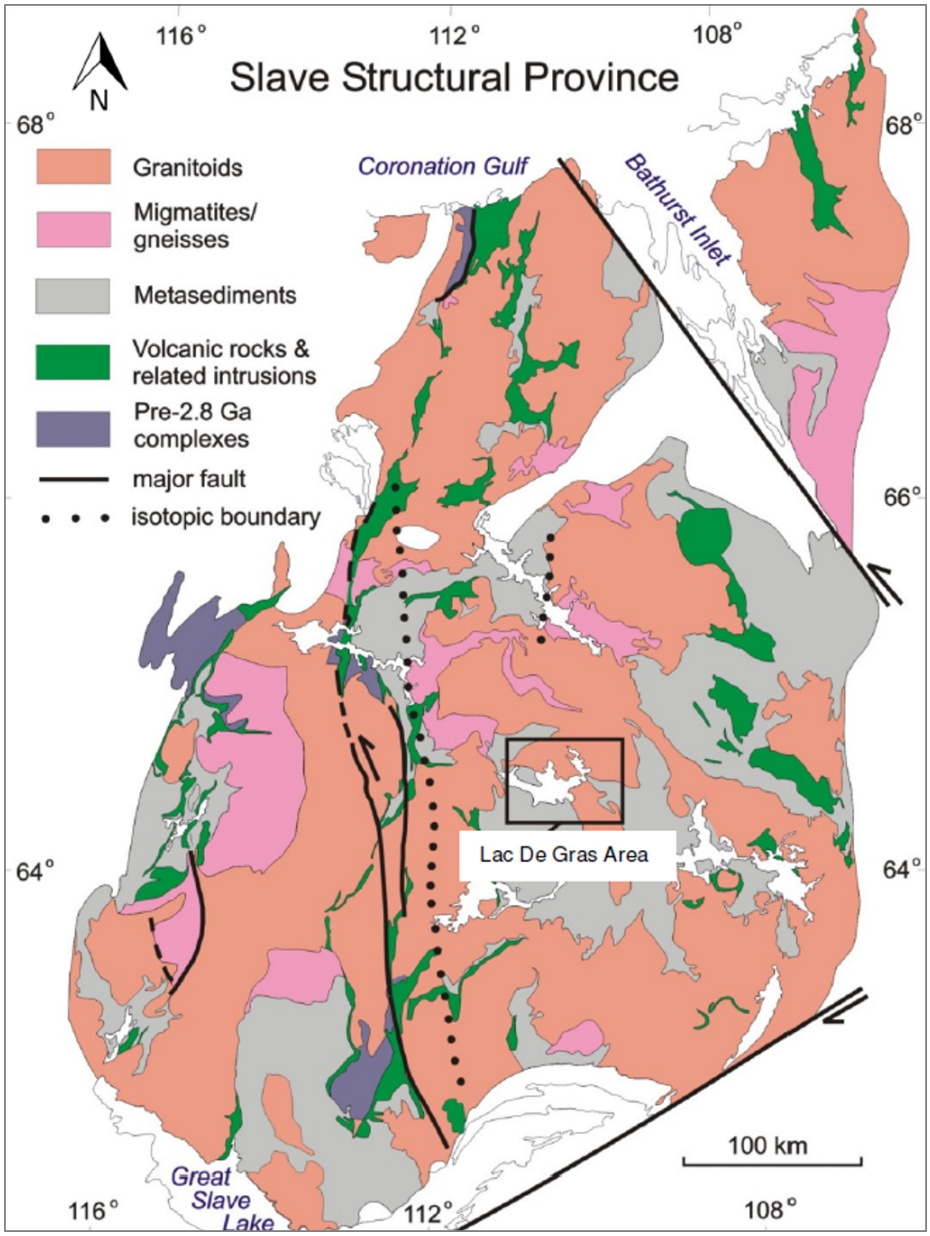

Figure 4.7. A regional geology map of the Slave Structural Province (from Yip and Thompson, 2015, as modified from Stubley, 1998). The black box outlines the Lac de Gras area for kimberlite exploration.

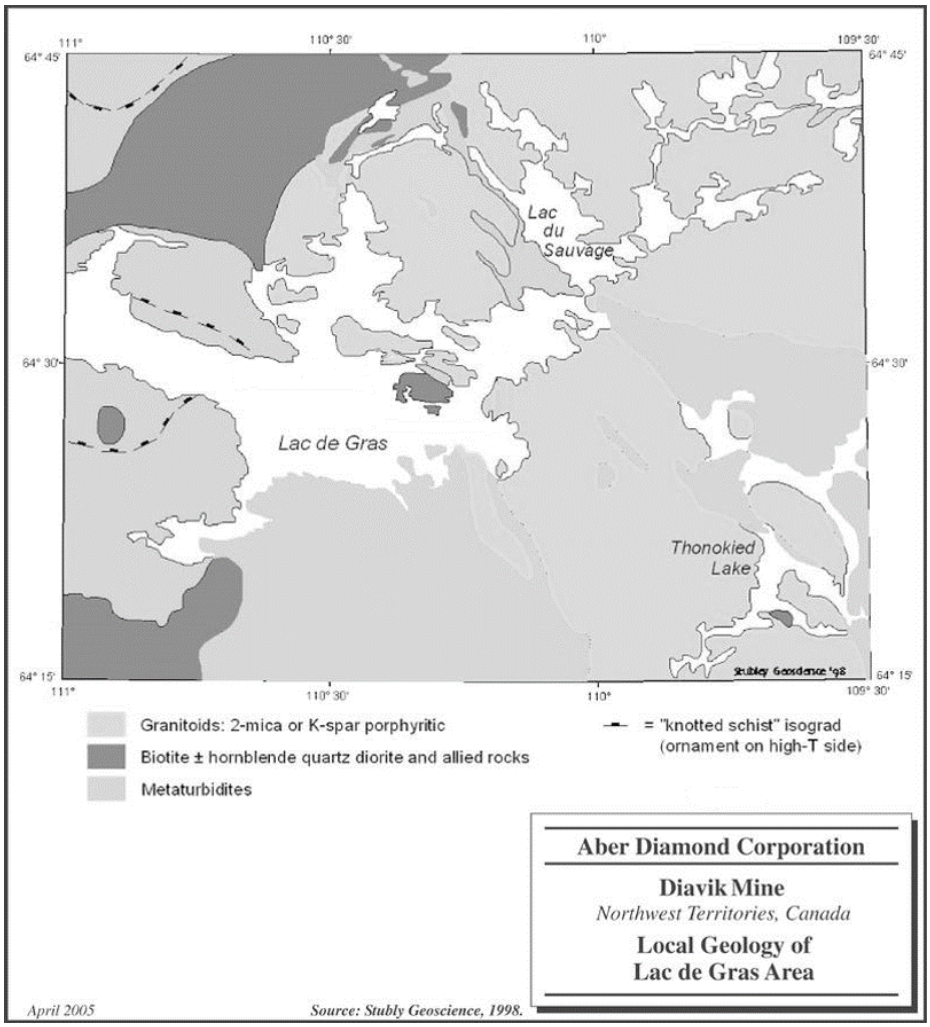

Figure 4.8. A local geology map of the Lac de Gras area (from Roscoe and Postle, 2005, as modified from Stubley, 1998). Three main Archean lithologies are present in this area.

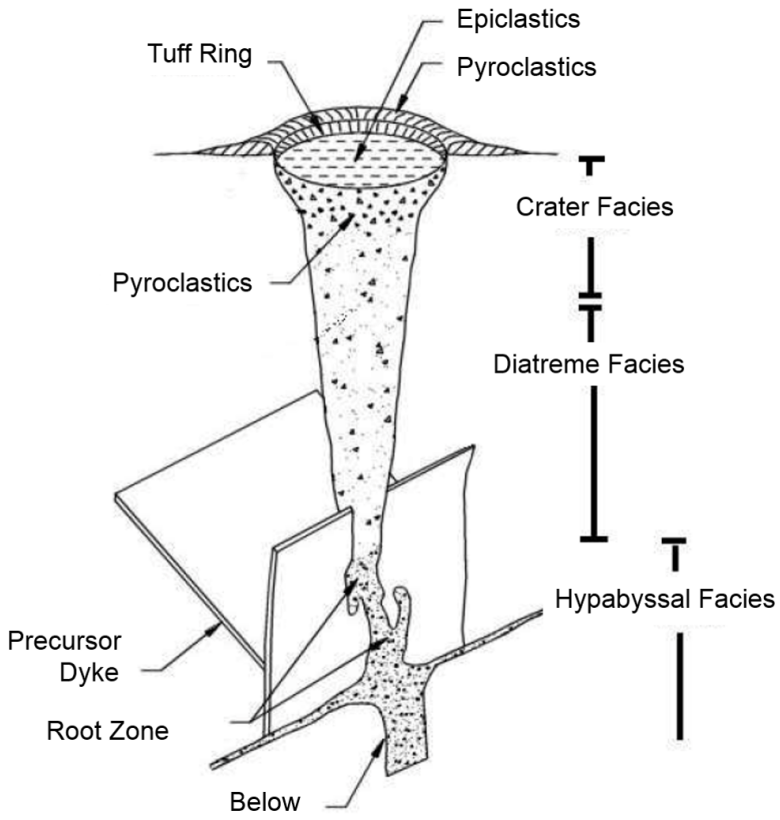

Figure 4.9. Facies and components of a typical kimberlite pipe with no erosion (from Power and Hildes, 2007).

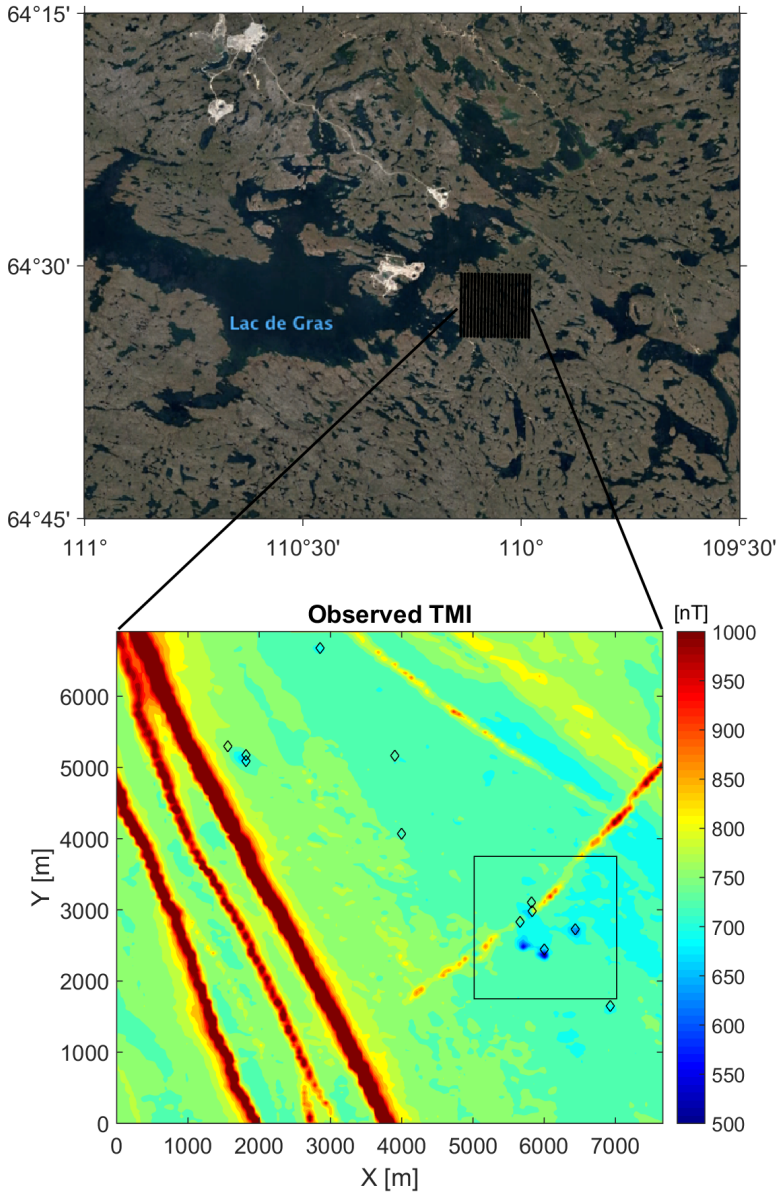

Figure 4.10. Airborne magnetic survey in the Lac de Gras area. Top panel shows the flight lines of the airborne magnetic survey. There are 103 flight lines with a line spacing of 75 m. Bottom panel shows the map of the observed TMI data in the survey area using a local coordinate. The diamond symbols indicate the known kimberlite pipes. The black box shows the subset used for the inversion.

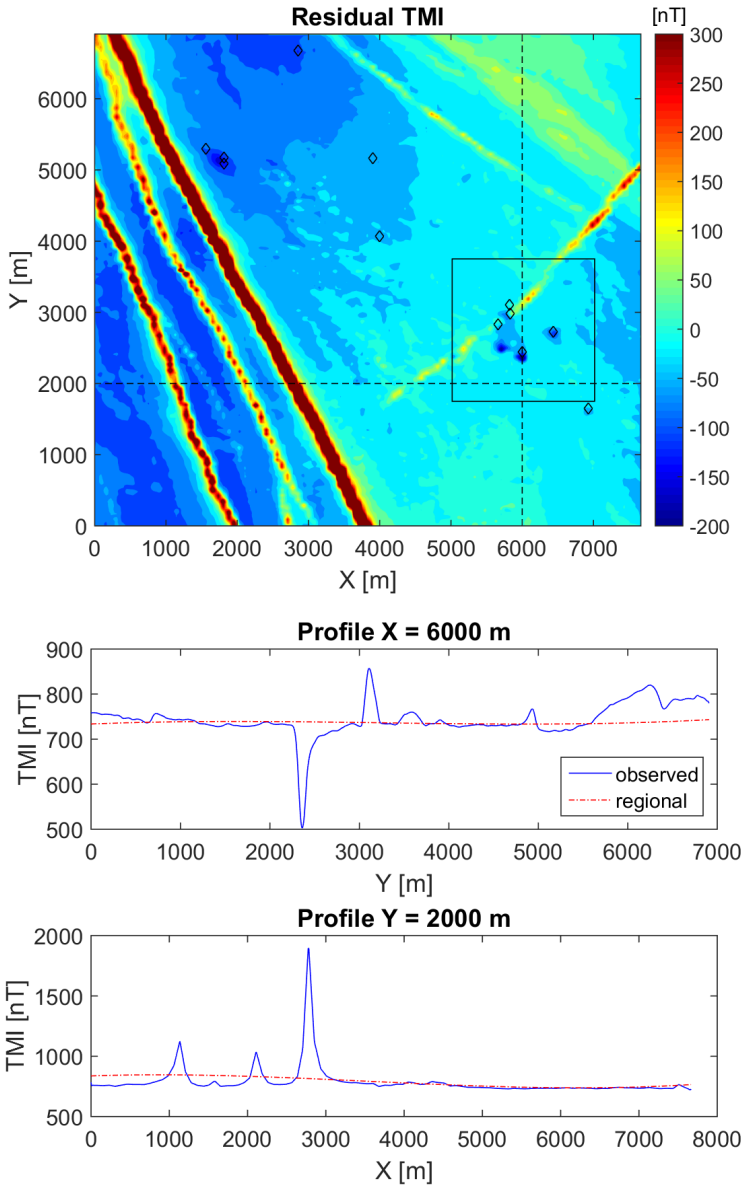

Figure 4.11. Map of the residual TMI field in the survey area. The diamond symbols indicate the known kimberlite pipes. The black box shows the subset used for the inversion. Two profiles of the observed and regional fields are provided. A third order polynomial was used to approximate the regional field.

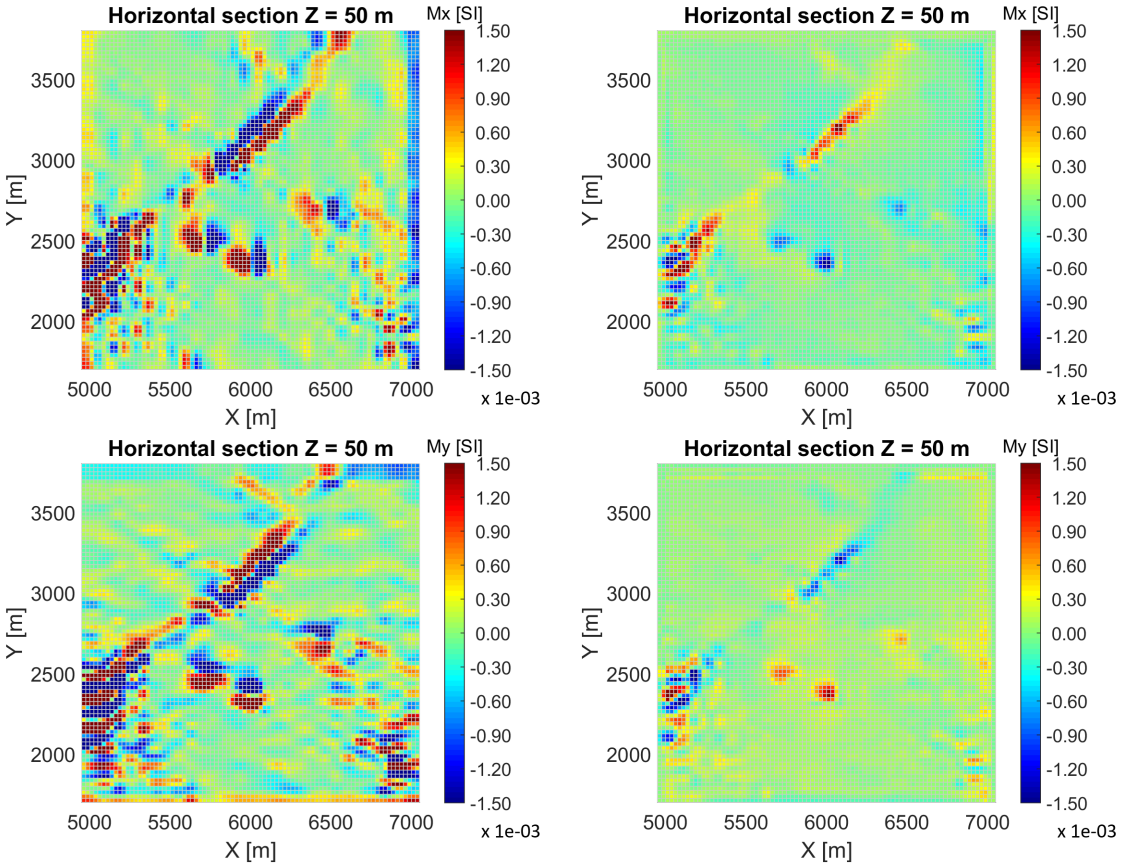

Figure 4.12. Horizontal sections of the recovered M_x (top panels) and M_y (bottom panels) components of the magnetization vector in the survey area. For comparison, the inversion results obtained by using only the minimum norm stabilizer (left panels) and using both the minimum norm and Gramian stabilizers (right panels) are provided. Both inversions ran to a normalized misfit of 1%.

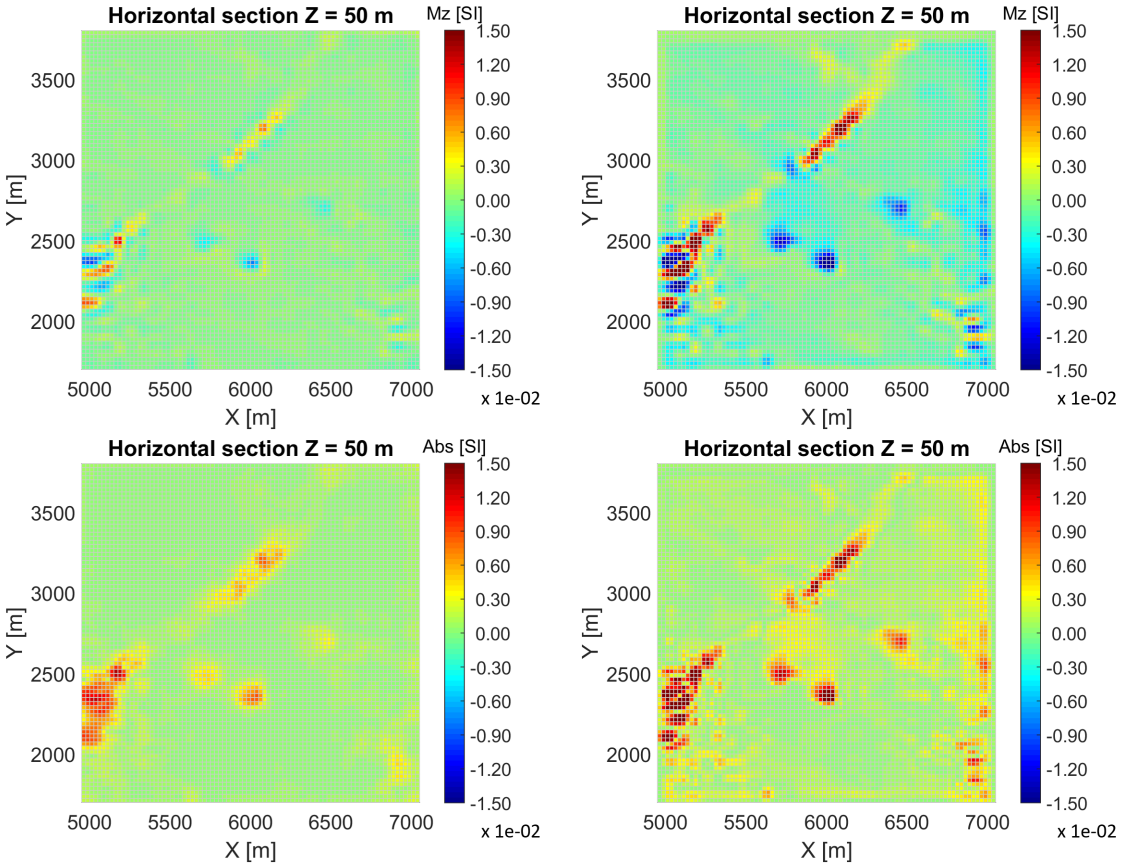

Figure 4.13. Horizontal sections of the recovered M_z component (top panels) and magnitude (bottom panels) of the magnetization vector in the survey area. For comparison, the inversion results obtained by using only the minimum norm stabilizer (left panels) and using both the minimum norm and Gramian stabilizers (right panels) are provided. Both inversions ran to a normalized misfit of 1%.

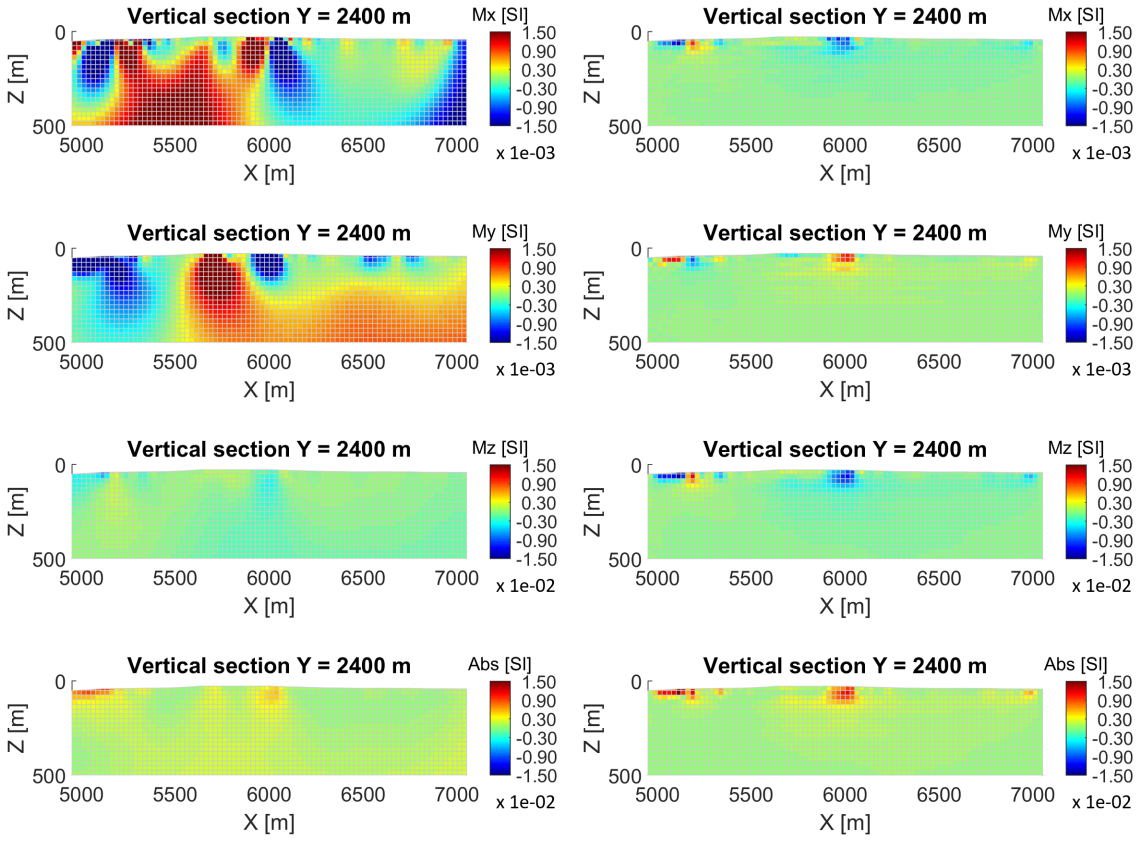

Figure 4.14. Vertical sections of the recovered scalar components (top three panels) and magnitude (bottom panels) of the magnetization vector in the survey area. For comparison, the inversion results obtained by using only the minimum norm stabilizer (left panels) and using both the minimum norm and Gramian stabilizers (right panels) are provided. Both inversions ran to a normalized misfit of 1%.

CHAPTER 5

JOINT INVERSION OF MAGNETIC AND ELECTROMAGNETIC DATA

Airborne surveys are routinely used for mineral exploration and regional geophysical study. These surveys usually collect different geophysical data simultaneously. One of the major challenges in interpretation of airborne geophysical data is the ability to jointly invert multiple geophysical datasets to self-consistent 3D earth models of physical properties that can subsequently be used for mapping the mineral deposits. In this chapter, I developed a joint inversion method for the magnetization vector and conductivity using Gramian constraints in the presence of remanent magnetization. The developed joint inversion algorithm was applied to the airborne total magnetic intensity (TMI) and electromagnetic (EM) data collected for kimberlite exploration in the Lac de Gras area of the Northwest Territories of Canada. A localized Gramian constraint approach was also used in the case study to recover multiple lithologic relationships between the different physical properties.

5.1 Theory

5.1.1 Inverse problem formulation

Previous chapters have discussed inverse problems related to the potential field only. This chapter extends the joint inversion approach to include both potential field and electromagnetic data. In the joint inversion for the magnetization vector and conductivity, when remanent magnetization is present, the parametric functional is given as follows:

$$P(\widetilde{\mathbf{m}}^{(1)},\widetilde{\mathbf{m}}^{(2)}) = \sum_{i=1}^{2}\Big(\big\|\mathbf{W}_d^{(i)}\big(\tilde{\mathbf{A}}^{(i)}(\widetilde{\mathbf{m}}^{(i)})-\mathbf{d}^{(i)}\big)\big\|^2+\alpha^{(i)}\big\|\mathbf{W}_m^{(i)}\big(\widetilde{\mathbf{m}}^{(i)}-\widetilde{\mathbf{m}}_{apr}^{(i)}\big)\big\|^2\Big)$$

$$+\beta\Big(S_{G_T}\big(\widetilde{\mathbf{m}}_x^{(1)},\widetilde{\mathbf{m}}^{(2)}\big)+S_{G_T}\big(\widetilde{\mathbf{m}}_y^{(1)},\widetilde{\mathbf{m}}^{(2)}\big)+S_{G_T}\big(\widetilde{\mathbf{m}}_z^{(1)},\widetilde{\mathbf{m}}^{(2)}\big)\Big), \qquad (5.1)$$

where the model parameters are defined as:

$$\mathbf{m}^{(1)} = [M_x \; M_y \; M_z]^\top, \tag{5.2}$$

$$\mathbf{m}^{(2)} = \sigma - \sigma_b. \tag{5.3}$$

The normalized model parameters and corresponding model weighting coefficients are calculated in the following way:

$$\widetilde{\mathbf{m}}^{(i)} = W_{m,c}^{(i)} \, \mathbf{m}^{(i)}, \; W_{m,c}^{(i)} = \frac{1}{\max \left| \mathbf{m}_s^{(i)} \right|}, \; i = 1, 2, \tag{5.4}$$

where $\mathbf{m}_s^{(i)}$ are the model parameters obtained from the separate inversions. The vectors $\widetilde{\mathbf{m}}_x^{(1)}$, $\widetilde{\mathbf{m}}_y^{(1)}$, and $\widetilde{\mathbf{m}}_z^{(1)}$ in expression (5.1) are the normalized components of the magnetization vector, which are given as:

$$\widetilde{\mathbf{m}}_x^{(1)} = W_{m,c}^{(1)} \, M_x, \tag{5.5}$$

$$\widetilde{\mathbf{m}}_y^{(1)} = W_{m,c}^{(1)} \, M_y, \tag{5.6}$$

$$\widetilde{\mathbf{m}}_z^{(1)} = W_{m,c}^{(1)} \, M_z. \tag{5.7}$$

Iterative process (2.37) or (2.38) of the regularized conjugate gradient method can be used to solve the minimization problem (5.1). For this specific inverse problem, the derivative matrix of the Gramian terms in expression (5.1) is computed as follows:

$$\mathbf{G} = \begin{bmatrix} \mathbf{G}_x^{(1)} & & & \\ & \mathbf{G}_y^{(1)} & & \\ & & \mathbf{G}_z^{(1)} & \\ & & & \mathbf{G}^{(2)} \end{bmatrix}, \tag{5.8}$$

where the matrices $\mathbf{G}_x^{(1)}$, $\mathbf{G}_y^{(1)}$, $\mathbf{G}_z^{(1)}$, and $\mathbf{G}^{(2)}$ are the partial derivative matrices of the Gramian constraints with respect to $\widetilde{\mathbf{m}}_x^{(1)}$, $\widetilde{\mathbf{m}}_y^{(1)}$, $\widetilde{\mathbf{m}}_z^{(1)}$, and $\widetilde{\mathbf{m}}^{(2)}$, respectively. Formulas of these matrices can be found in the previous chapters.

5.2 Model study

5.2.1 A block model

I conducted a numerical test of the developed method using a simple model of a rectangular conductive and magnetized block of the dimensions 100 m by 100 m by 50 m buried at a depth of 50 m. The block has a resistivity of 100 Ohm-m, while the homogeneous background half-space has a resistivity of 1000 Ohm-m. The magnetic properties of the block are characterized by an intensity of magnetization as $\mathbf{I} = H_0\,\mathbf{M}$, where magnetization vector, $\mathbf{M}$ has the following scalar components:

$$M_x = 0.06/\sqrt{2},$$
$$M_y = 0,$$
$$M_z = 0.06/\sqrt{2},$$

I also assume that the magnitude of inducing magnetic field is equal to $H_0 = 50\ 000$ nT, and the inclination and declination are as follows: $I = 75^\circ$ and $D = 15^\circ$.

There are 121 receivers located in the nodes of an 11 by 11 rectangular grid with 50 m spacing in both horizontal directions and at 30 m above the ground, simulating an airborne survey. The receivers measure both the permanent magnetic anomalous field due to the block's magnetization and the frequency domain magnetic field due to EM induction in the conductive block. Figure 5.1 shows the location of the receivers and the block with anomalous magnetization and conductivity.

Synthetic airborne magnetic TMI data were computed using the forward modeling code based on the integral equation method. The magnetic field data in the frequency domain were computed using the IE method for the parameters of the DIGHEM airborne system, which measures five components of the magnetic field. The first three components are coplanar fields, representing the vertical magnetic field at three different frequencies, 56000, 7200, and 900 Hz, generated by a vertical magnetic dipole source. Another two components are the coaxial fields, representing the horizontal magnetic field along the flighting direction at two frequencies, 5500 and 900 Hz, generated by a horizontal magnetic dipole source oriented along the flight line. I added 3% random noise to the observed TMI field and all components of the frequency magnetic data. The simulated TMI field is shown in Figure 5.2. Figure 5.3 presents

the frequency domain magnetic responses, which are normalized by the reference magnetic field in the free space.

The joint inversion was first applied with T being the identity operator, implying a direct correlation between the magnetization vector and the anomalous conductivity. Figures 5.4 to 5.7 provide comparisons between the joint inversion results and those obtained from the separate inversions. The individual magnetic inversion produced a very diffused anomalous body with the magnitude of the magnetization vector significantly underestimated. Inverting three components of the magnetization vector is a very nonunique problem. By using the Gramian constraints in the joint inversion, I was able to reduce this ambiguity so that the artifacts related to the M_x and M_y components were greatly reduced, as shown in Figure 5.6. The anomalous magnetic body became much more compact and obtained a more accurate magnitude of the magnetization vector. The recovered conductive anomaly also benefited from the joint inversion that the artifacts in the very shallow area were greatly reduced.

I also tested the joint inversion algorithm with operator T being the gradient operator, ∇, resulting in a structural correlation between the two physical properties. In this case the inversion based on the Gramian constraints behaves similarly to the inversion based on the cross-gradient method. The results of the joint inversion are shown in Figures 5.8 and 5.9. It turns out that correlating the gradients of the model parameters takes more iterations of joint inversion. The Gramian stabilizer with the gradients of the model parameters also helped recovering a more accurate shape and magnitude of the magnetization vector compared to the separate inversion results. The conductive anomaly was slightly improved in this test, producing a good image of the conductive target.

5.3 Case study: Kimberlite exploration in the Northwest of Canada

5.3.1 Airborne surveys

I applied the developed joint inversion algorithm to the field airborne data collected for kimberlite exploration in the Lac de Gras area of the Northwest Territories of Canada. A typical kimberlite pipe in the survey area has the shape of a carrot,

which can be subdivided from top to bottom into crater, diatreme, and hypabyssal facies, as shown in Figure 5.10 (a). The physical properties of the different facies of the kimberlite and the country rock are shown in Figure 5.10 (b). Generally, all kimberlite facies have a weakly higher magnetic susceptibility than the surrounding country rock. They are also associated with the conductive anomaly buried in a very resistive background, up to more than 10 000 Ohm-m, which is a very challenging situation in the airborne electromagnetic inversion.

I selected a subset of the airborne magnetic and electromagnetic survey data over a known kimberlite pipe, which included 40 airborne receivers at around 30 m above the ground and covered an area of approximately 500 m by 500 m, as shown in Figure 5.11. The TMI field in the entire survey area has a strong positive regional background, which was subtracted from the total field by a third order polynomial approximation. The coplanar and coaxial magnetic fields in the airborne EM survey are quite noisy. Besides regular noises (instrumental error, positioning error, etc.), these data could also be affected by the relatively high magnetization of the rocks in the target area, which can be treated as an additional noise in the EM data. I inverted the residual TMI data (Figure 5.12) and imaginary part of the frequency domain magnetic field (Figure 5.13), while the real part has been excluded due to the large noise contamination. To consider the remanent magnetization of the kimberlite targets, I jointly inverted for three scalar components of the magnetization vector and the conductivity.

5.3.2 Inversion results

In the first step of the analysis, the separate inversions of the TMI and EM data sets were conducted. More specifically, a 1D inversion was first applied to the EM data. This is important in order to determine the background resistivity, which can be used in the next 3D EM inversion. Using the 1D EM inversion result as the starting model and setting the half-space background conductivity as 10^{-5} S/m, I ran a full 3D EM inversion independently for the subsurface resistivity distribution. I also ran a 3D inversion of the TMI data independently for the magnetization vector. Figure 5.14 shows the separate inversion results. The magnetic anomaly shown in the left

panels of Figure 5.14 is too diffused to provide accurate depth information about the target, which is a typical problem for unconstrained potential field inversions. In contrast, the conductive anomaly presented in the right panels of the same figure is more compact and has a higher depth resolution due to the multiple frequency components in the airborne EM data. The cross plot derived from the separate inversions shows roughly two trends between the magnitude of the magnetization vector and the anomalous conductivity. However, these trends are too cloudy to be used for the lithologic identification.

In the next step of the analysis, I applied the joint inversion with the localized Gramian constraints using formula (3.2) with two subdomains, one for the kimberlite pipe, the other for the near-surface inhomogeneity. The results of the joint inversion with operator T being the identity operator are shown in Figure 5.15. One can see a carrot-shaped anomaly with higher magnetization and lower resistivity in Figure 5.15, which is interpreted as the kimberlite pipe. The recovered near-surface inhomogeneity outside the kimberlite pipe is conductive but not magnetic susceptible, which is typical for an overburden in the survey area. There are two linear trends observed in the cross plot of the magnitude of the magnetization vector versus the anomalous conductivity obtained from the joint inversion. One is associated with the kimberlite pipe (which is conductive and has an increased magnetic susceptibility) and the other with the near-surface inhomogeneity outside the kimberlite pipe (which is more conductive and has a lower magnetic susceptibility), respectively. A comparison between the cross plots derived from the separate and joint inversions is presented in Figure 5.16. Figure 5.17 shows the data fitting curves for the airborne magnetic and electromagnetic data. Both the separate and joint inversions fit the observed data at about the same level. To conclude, the joint inversion with the localized Gramian constraints was able to recover multiple lithologic relationships between the different physical properties, and thus enhanced surface imaging of the kimberlite targets.

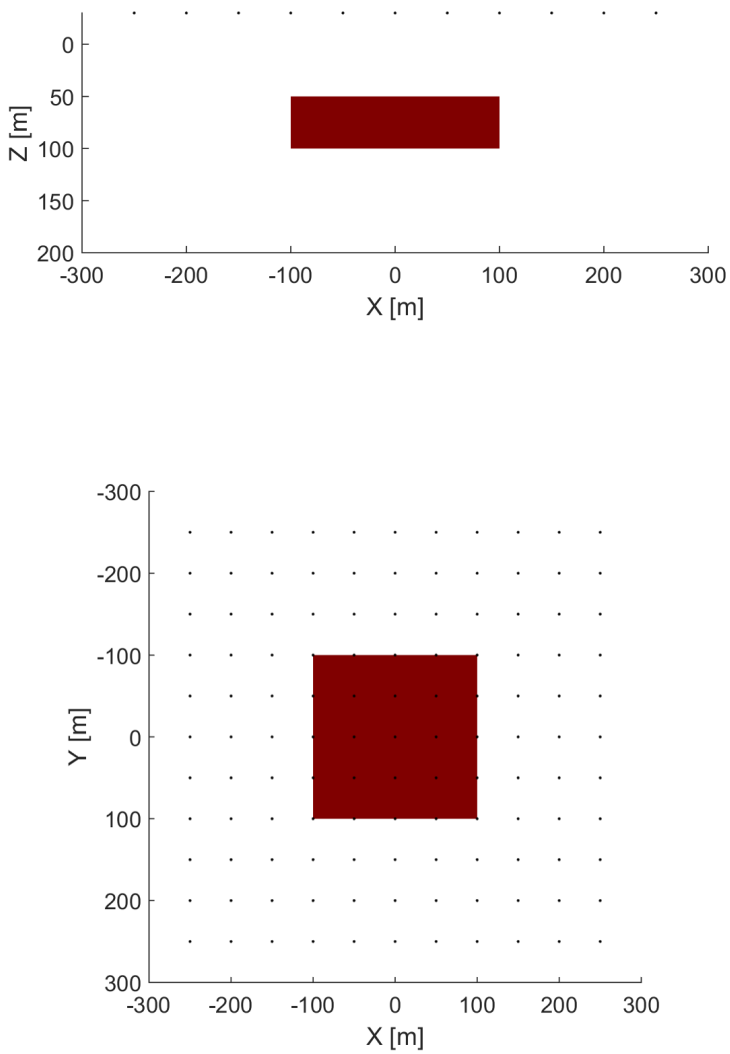

Figure 5.1. A sketch of the block model and receiver locations used in the synthetic model study. The side (top panel) and top (bottom panel) views of the block model are provided. The receivers are located in the nodes over an 11 x 11 grid of 50-m spacing at 30 m above the ground.

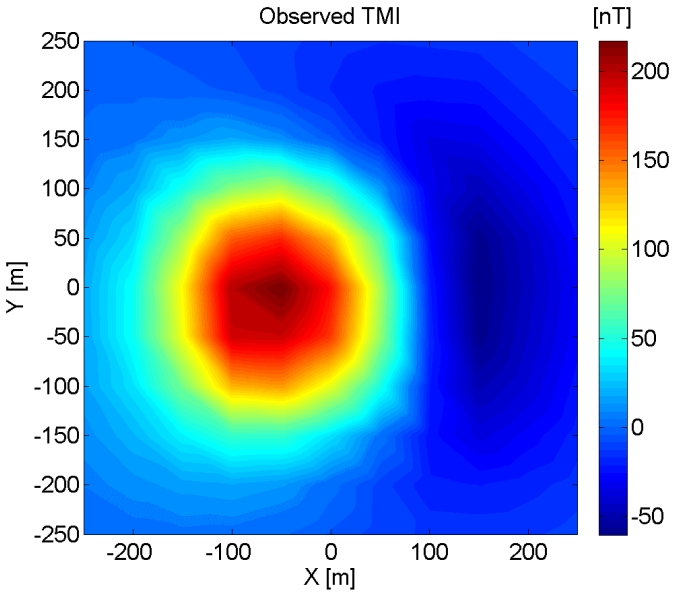

Figure 5.2. A map of the synthetic TMI field produced by the block model, contaminated by 3% random noise.

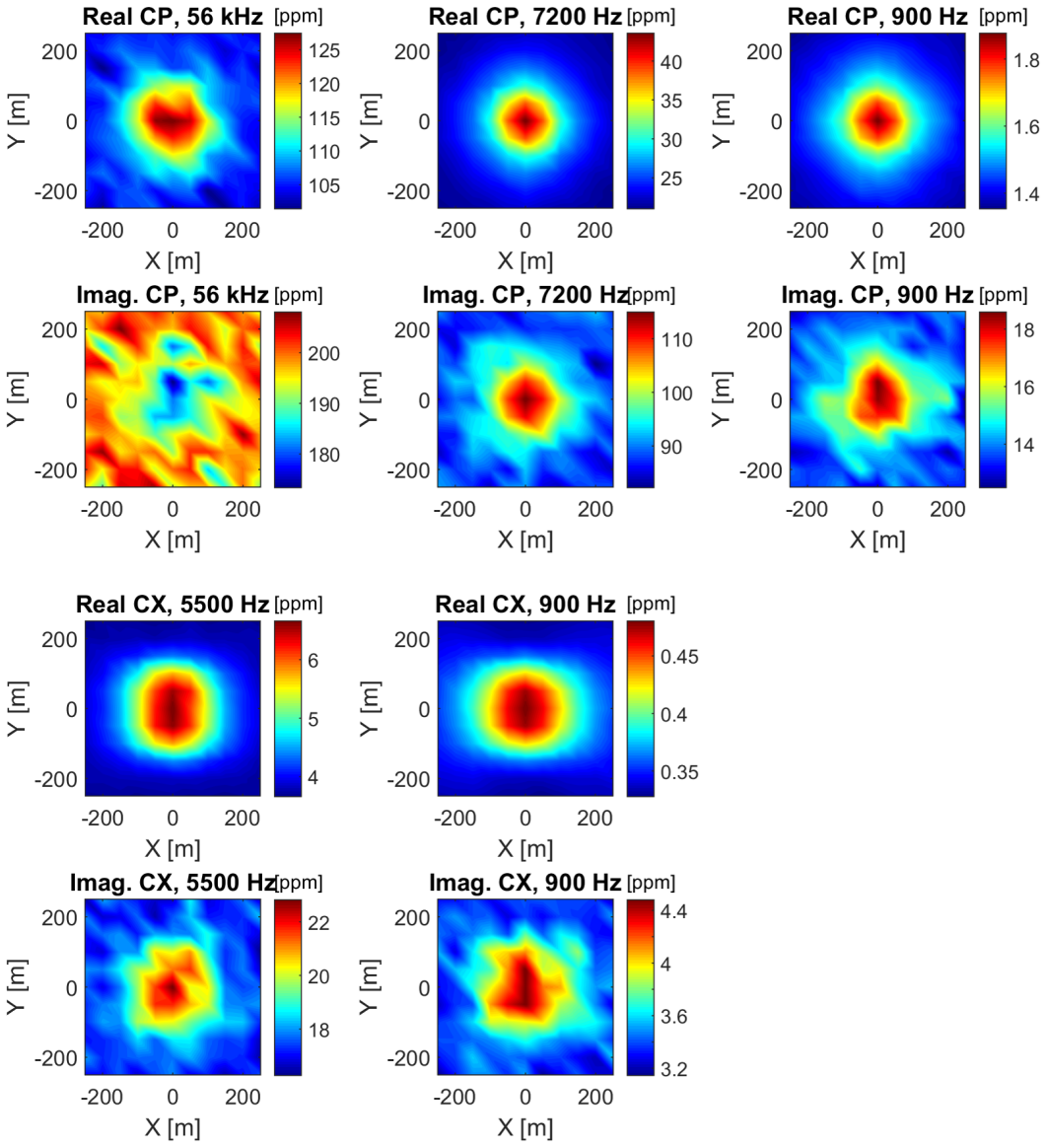

Figure 5.3. Maps of the coplanar (CP) and coaxial (CX) fields simulated for a model of the 100 Ohm-m block buried in a 1000 Ohm-m resistive background. The data are normalized by the fields in the free space and are contaminated by 3% random noise.

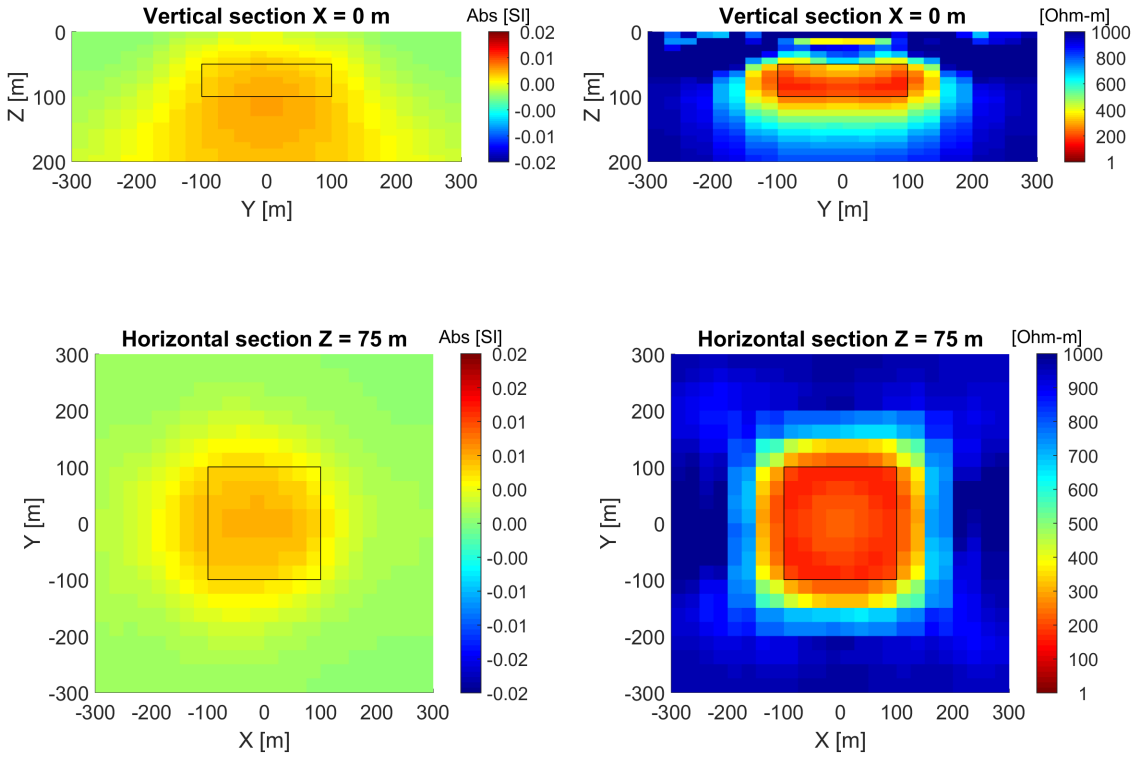

Figure 5.4. The recovered magnitude of the magnetization vector (left panels) and the resistivity (right panels) from the separate inversions.

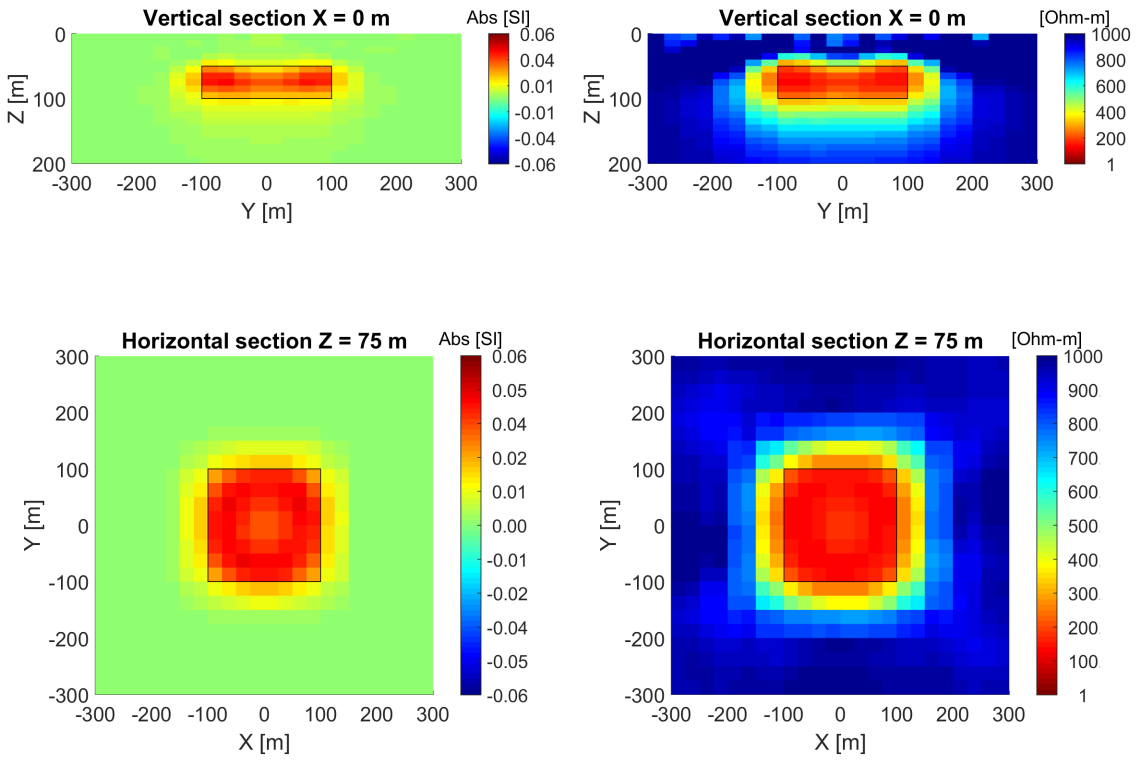

Figure 5.5. The recovered magnitude of the magnetization vector (left panels) and the resistivity (right panels) from the joint inversion with operator T being the identity operator in the Gramian constraints.

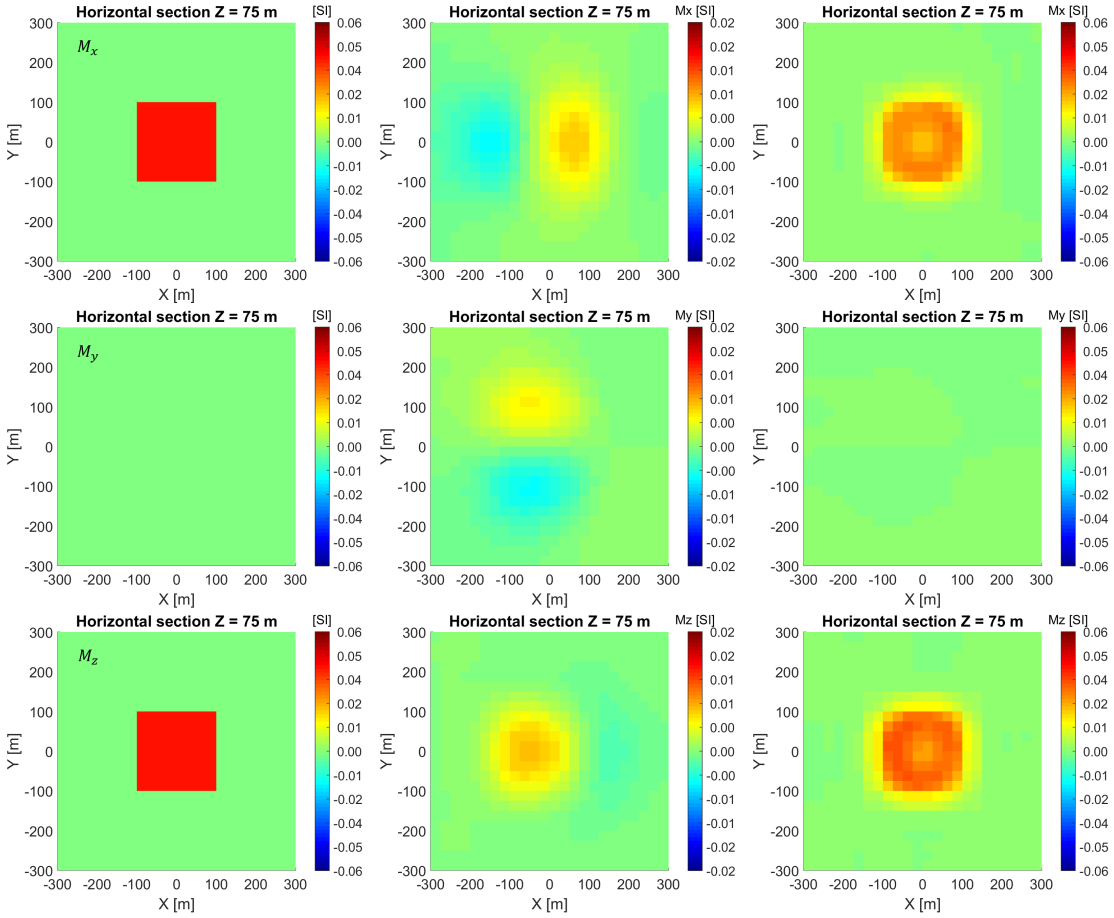

Figure 5.6. The recovered scalar components of the magnetization vector from the separate (middle panels) and joint (right panels) inversions with operator T being the identity operator. The right panels show the horizontal sections of the true model. Note that, the results of the separate magnetic inversions are plotted in a different color scale from the true model and the results of the joint inversion.

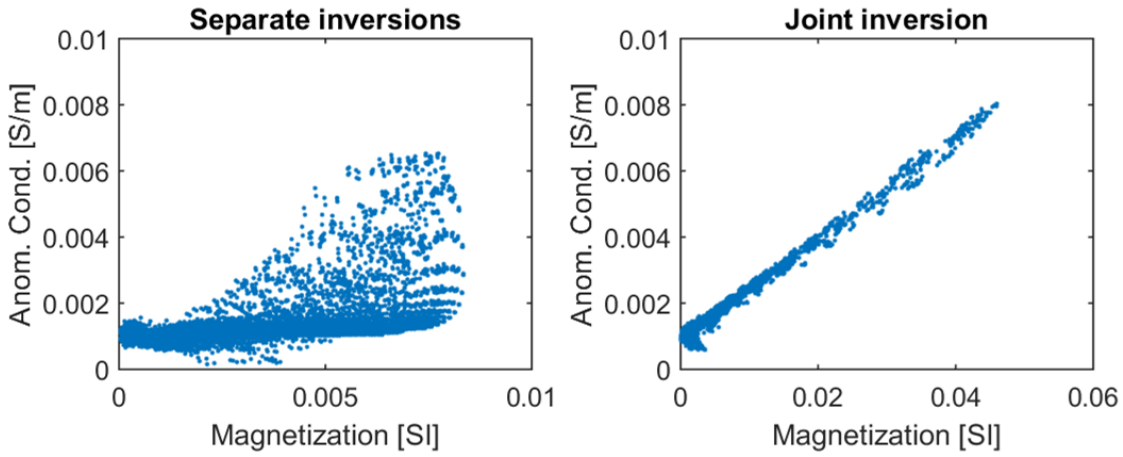

Figure 5.7. Cross plots of the magnitude of the magnetization vector versus anomalous conductivity from the separate (left) and joint (right) inversions with operator T being the identity operator in the Gramian constraints.

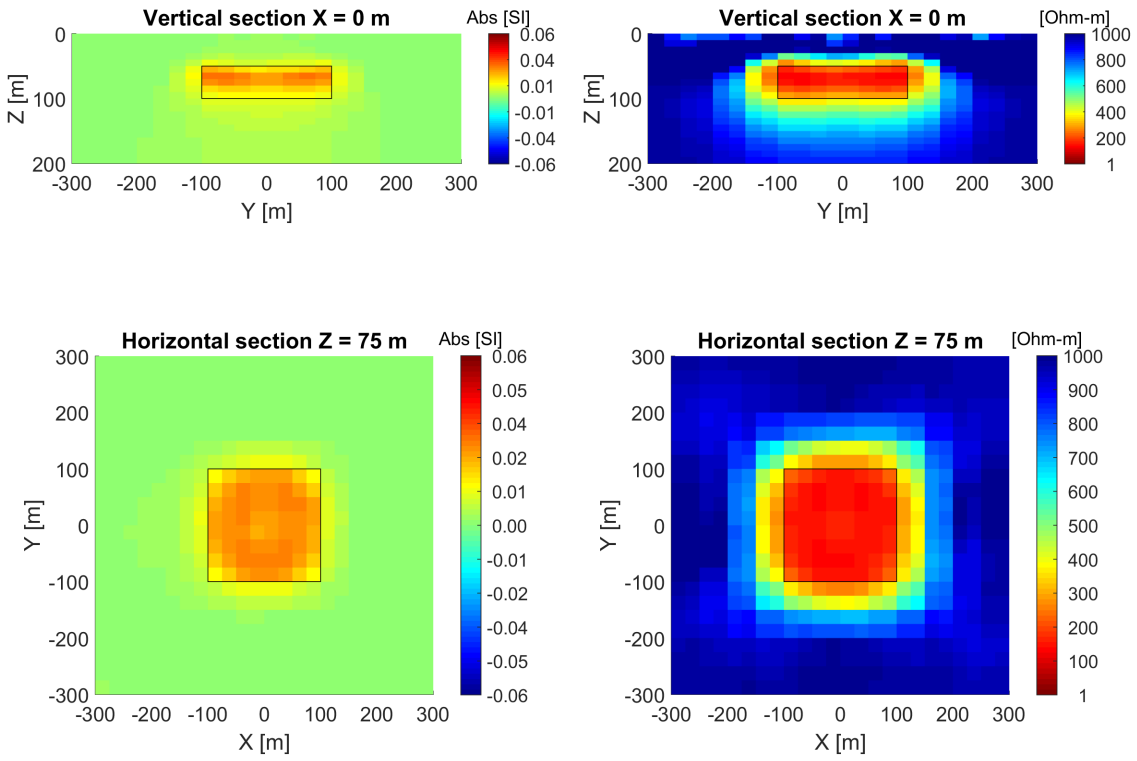

Figure 5.8. The recovered magnitude of the magnetization vector (left panels) and the resistivity (right panels) from the joint inversion with operator T being the gradient operator ∇ in the Gramian constraints.

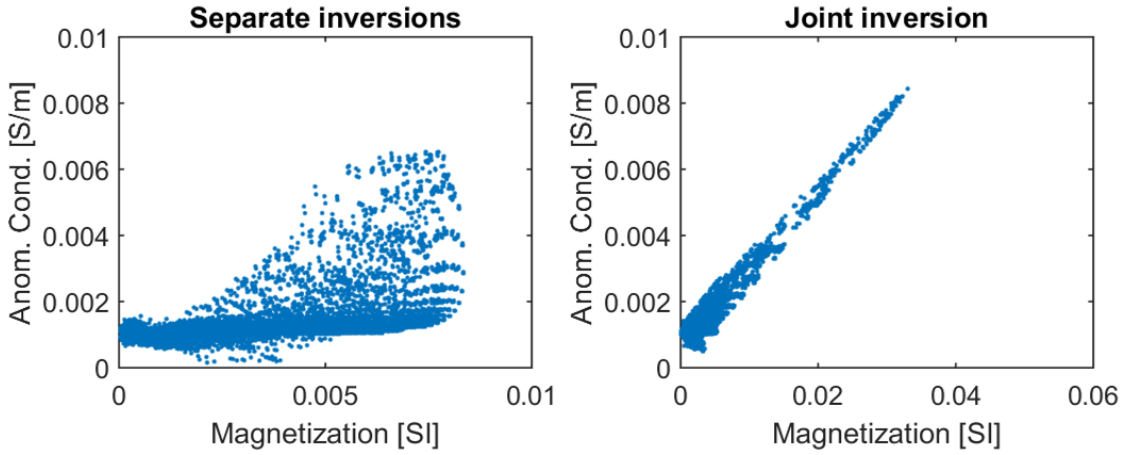

Figure 5.9. Cross plots of the magnitude of the magnetization vector versus anomalous conductivity from the separate (left) and the joint (right) inversions with operator T being the gradient operator ∇ in the Gramian constraints.

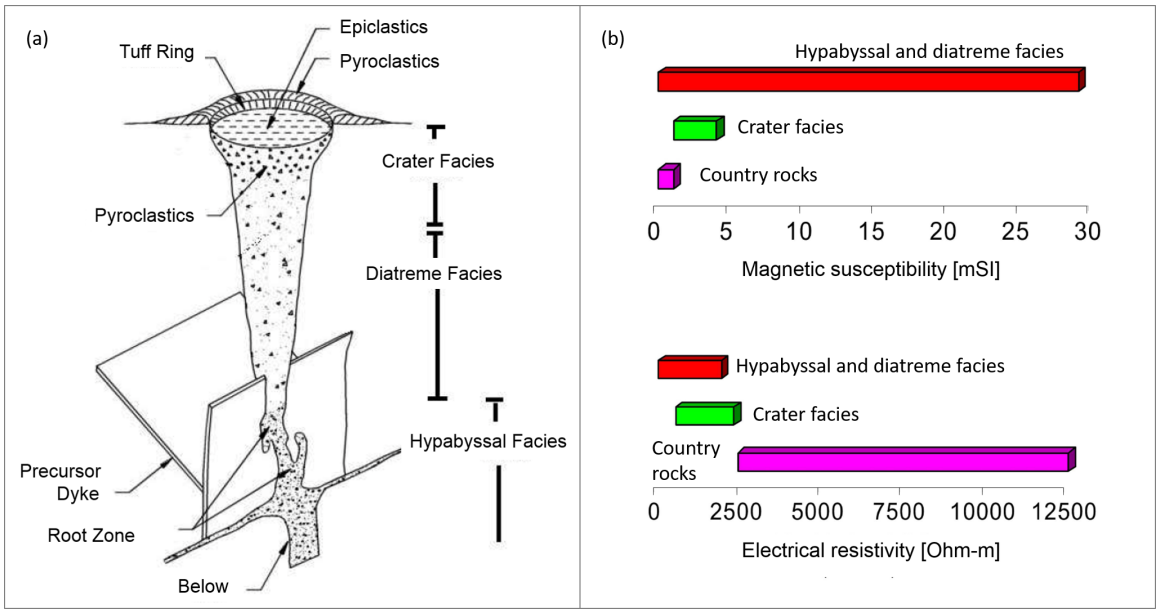

Figure 5.10. Properties of a typical kimberlite piple in the Lac de Gras area (from Power and Hildes, 2007). (a) Facies and components of the kimberlite pipe with no erosion. (b) Physical properties of the different facies of the kimberlite and the country rock.

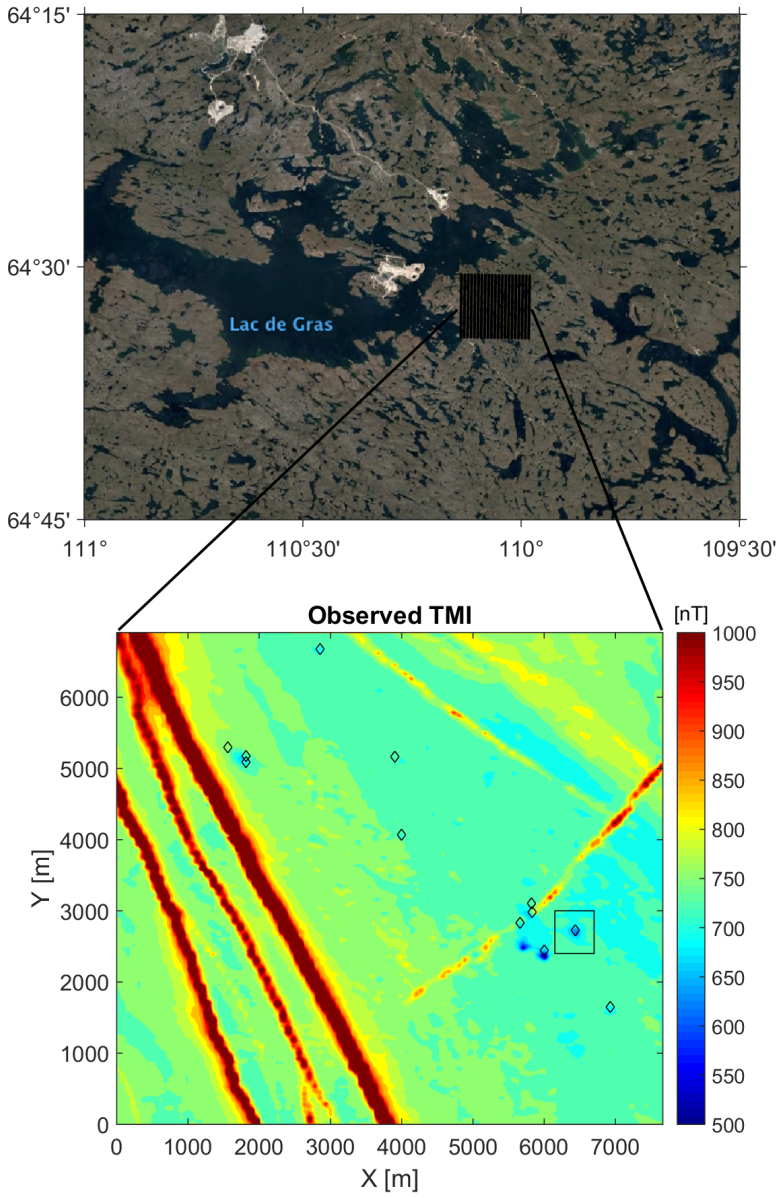

Figure 5.11. Airborne survey in the Lac de Gras area. Top panel shows the flight lines of the airborne survey. There are 103 flight lines with a line spacing of 75 m. Bottom panel shows the map of the observed TMI data in the survey area using a local coordinate. The diamond symbols indicate the known kimberlite pipes. The black box shows the subset used for the inversion.

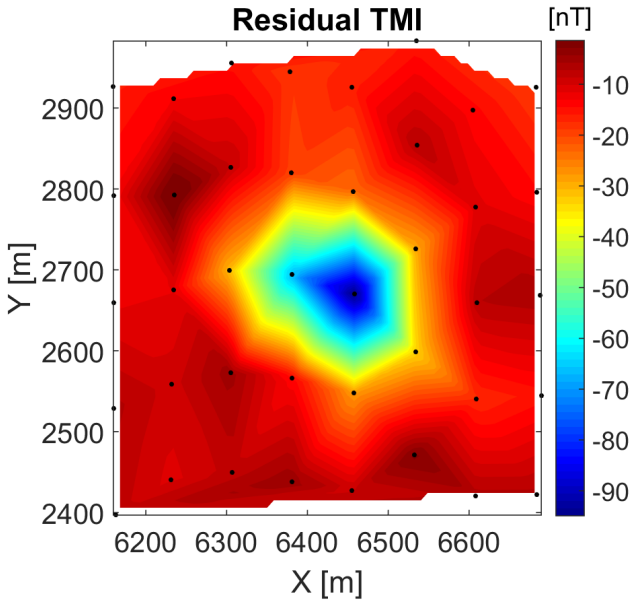

Figure 5.12. The residual TMI field over a known kimberlite pipe from the airborne magnetic survey. A third order polynomial approximation has been used to remove the regional trend. The black dots represent the location of the receivers.

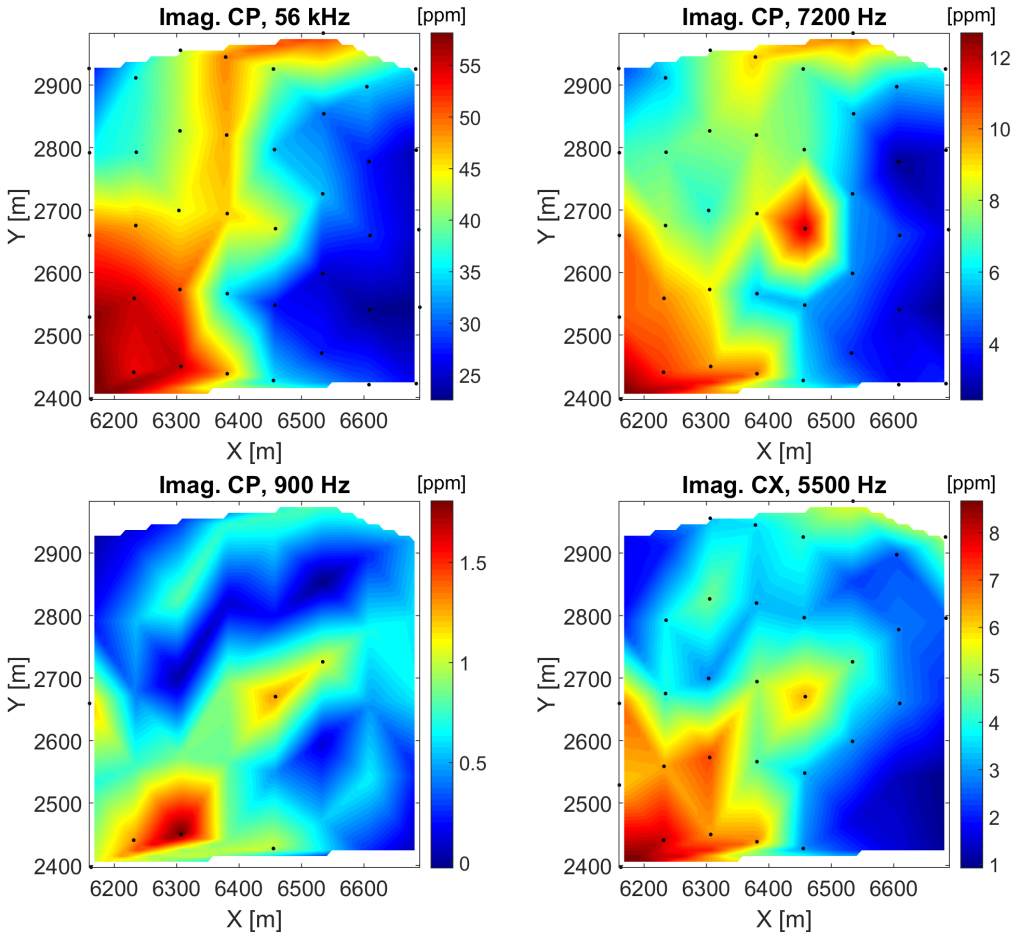

Figure 5.13. Imaginary part of the coplanar (CP) and coaxial (CX) magnetic fields over a known kimberlite pipe from the airborne electromagnetic survey. The black dots represent the data points used in the inversion, while the rest has been removed due to large noise contamination.

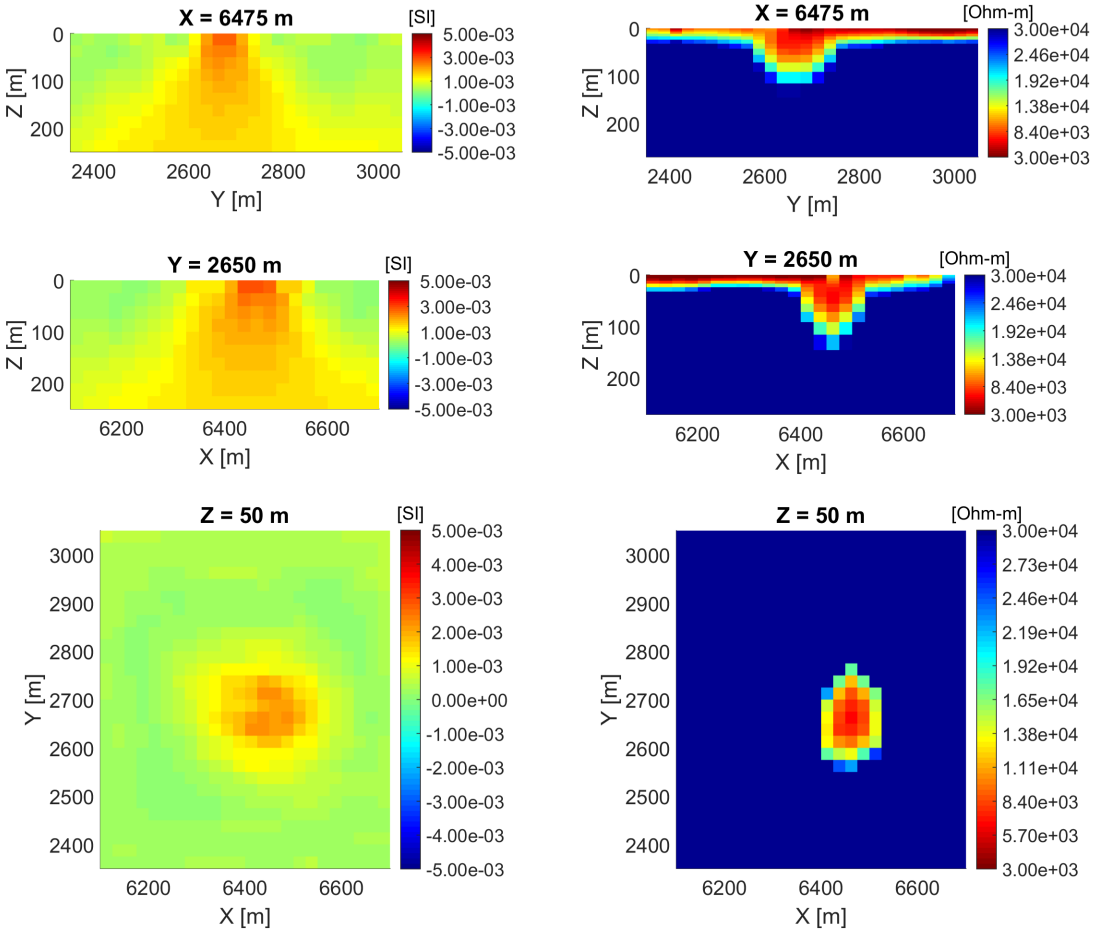

Figure 5.14. Vertical and horizontal sections of the recovered magnetization and resistivity models obtained by the separate inversions of the airborne TMI and EM data. The left panels present the magnitude of magnetization vector, while the right panels show the resistivity model in the survey area.

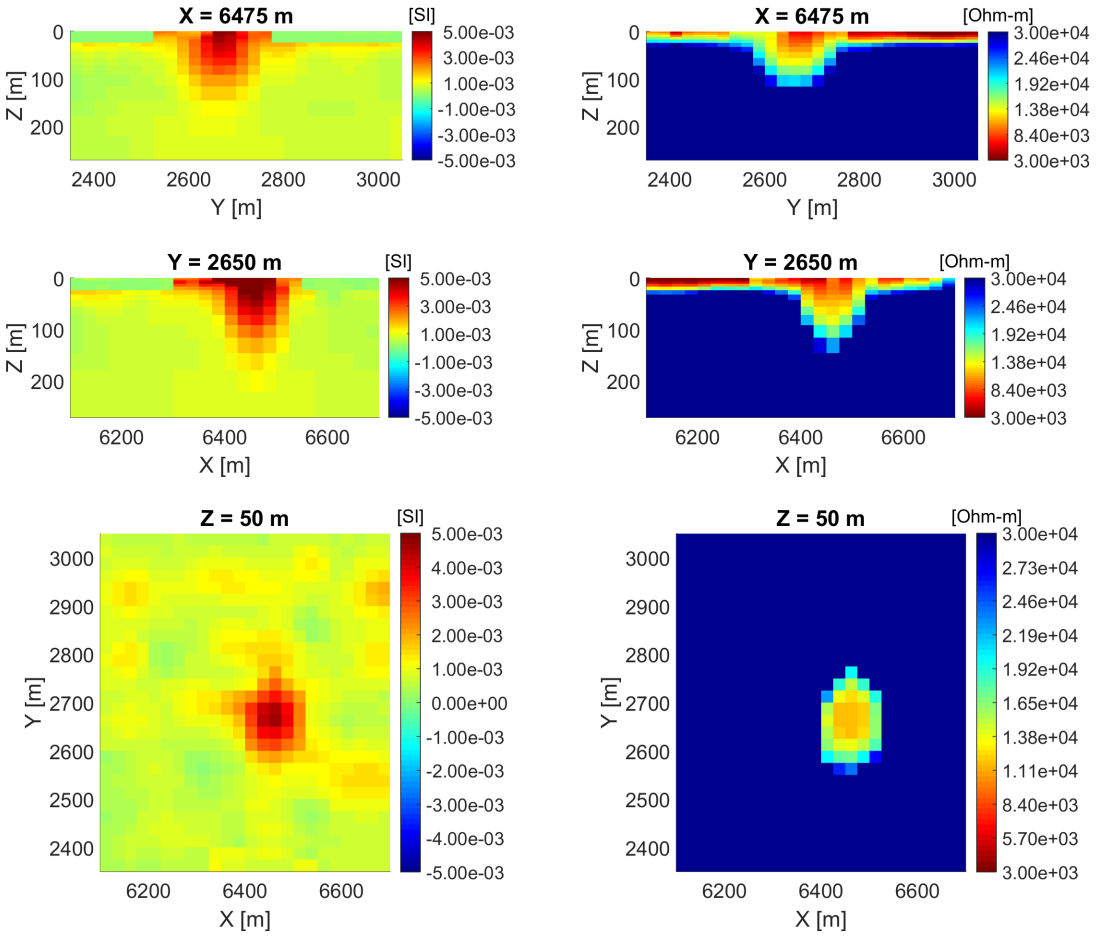

Figure 5.15. Vertical and horizontal sections of the recovered magnetization and resistivity models obtained by the joint inversion of the airborne TMI and EM data with the localized Gramian constraints.

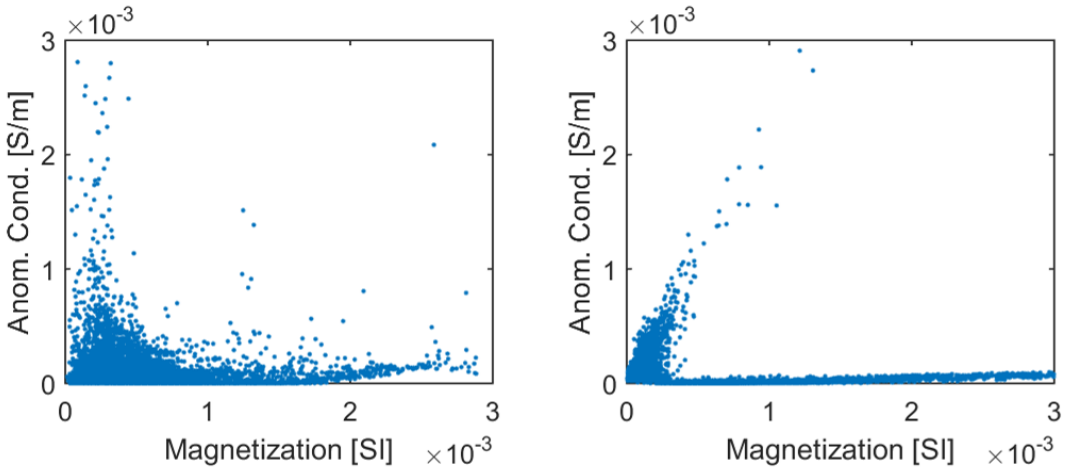

Figure 5.16. Cross plots of the predicted magnitude of the magnetization vector versus the anomalous conductivity. The left panel shows the plot derived from the separate inversions, while the right panel is the plot derived from the joint inversion with the localized Gramian constraints.

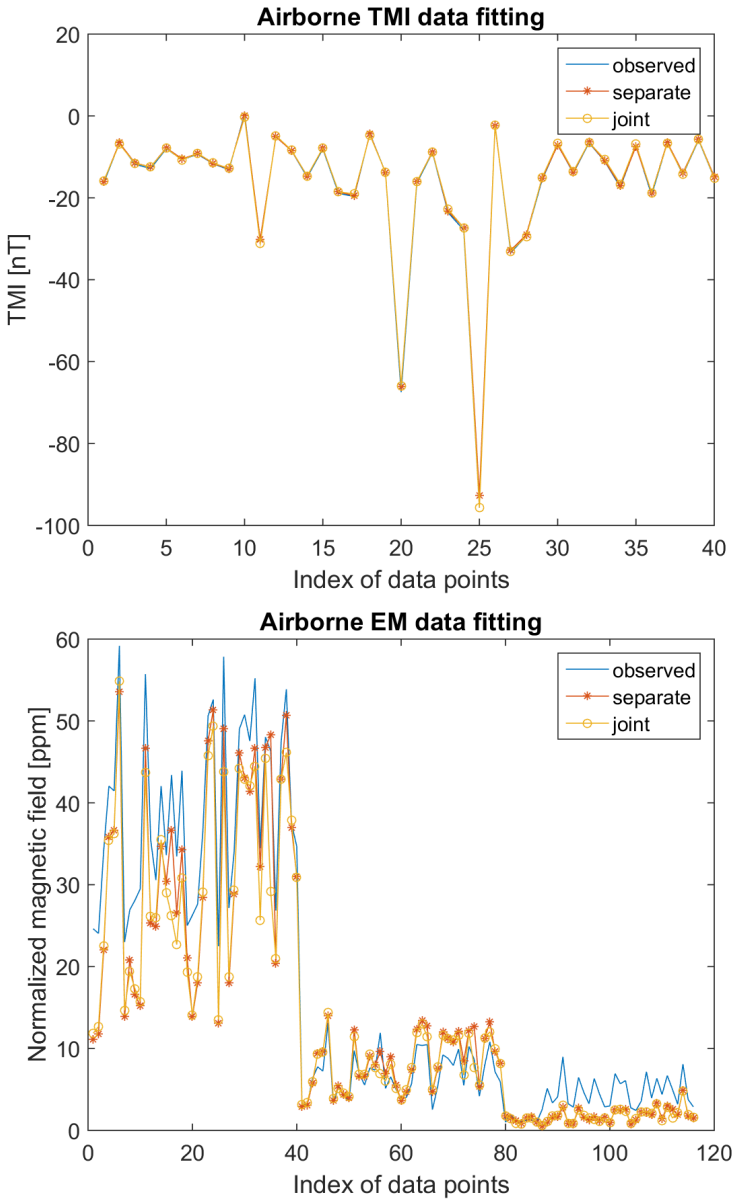

Figure 5.17. Data fitting curves for the airborne TMI (top) and EM (bottom) data. The separate and joint inversions fit the observed data at about the same level.

CHAPTER 6

CONCLUSIONS

Interpretation of multimodal geophysical data represents a data fusion problem, as different geophysical fields provide information about different physical properties of the Earth. In many cases, various geophysical data are complementary and self-constraining, making it natural to consider a joint inversion based on correlations between the different physical properties of the rocks. To date, there have been different approaches to the joint inversion. The simplest case has been when the physical properties are identical between the different geophysical methods. In other cases, joint inversion may infer theoretical, empirical, or statistical correlations between different physical properties. In a case where the specific form of the empirical or statistical correlation is unknown, joint inversion can be based on minimizing a value of the cross gradients between different model parameters.

In this dissertation, I formulated the joint inversion of potential field and electromagnetic data based on a generalized theoretical framework using Gramian constraints. I improved the application of joint inversion with respect to the following two aspects. First, I developed a model weighting technique to normalize the different model parameters with different units and magnitudes. This approach results in dimensionless model parameters and improves the stability of the joint inversion algorithm. Second, I introduced a localized Gramian constraint approach to impose different types of correlations in different subdomains of the joint inversion. Instead of enforcing a uniform correlation in the entire inversion domain, this approach can recover different lithologic relationships within different geologic bodies. Other developments in this dissertation include inverting for a nonlinear relationship between different model parameters using Gramian constraints, and a new magnetic

forward modeling algorithm based on triangular prism discretization to incorporate topography in the modeling domain.

The developed inversion algorithm was first applied to a joint inversion for density and magnetic susceptibility, assuming no remanent magnetization. When remanent magnetization is present, the model parameter becomes the magnetization vector instead of the scalar magnetic susceptibility. I developed a new magnetic inversion method for the magnetization vector using Gramian constraints, which impose spatial similarities between the different components of the magnetization vector. The kimberlite targets are characterized by a strong remnant magnetization in the case study area near Lac de Gras of the Northwest Territories of Canada. The developed magnetization vector inversion algorithm recovered round anomalies dominated by a magnetization in the vertical direction upward in the case study, which are considered to be the kimberlite targets. The joint inversion of airborne magnetic and electromagnetic data of the case study were also conducted. By using a localized Gramian constraint approach, the joint inversion recovered two linear trends between the magnitude of the magnetization vector and the anomalous conductivity: one associated with the kimberlite pipe, the other with the near-surface inhomogeneity.

In this dissertation, the subdomains used in the localized Gramian constraint approach were manually established. In the future, one can use statistical tools to determine these subdomains based on existing geologic information and the results of separate inversions, which should be more efficient and reliable. One drawback of the localized Gramian constraint approach is that it may introduce artificial boundaries between the different subdomains of an inversion. A solution to this problem is to run again the smooth inversions using initial models obtained from the joint inversion with localized Gramian constraints. Also, the joint inversion usually takes more iterations to converge due to the increased number of data and model parameters. It is necessary to develop faster joint inversion algorithms in the future, e.g., iterative Newton-type method, preconditioned conjugate gradient method, etc.

REFERENCES

Abubakar, A., G. Gao, T. M. Habashy, and J. Liu, 2012, Joint inversion approaches for geophysical electromagnetic and elastic full-waveform data: Inverse Problems, **28**, 055016.

Berdichevsky, M. N., and V. I. Dmitriev, 2008, Models and methods of magnetotellurics: Springer.

Bhattacharyya, B. K., 1980, A generalized multibody model for inversion of magnetic anomalies: Geophysics, **45**, 255–270.

Colombo, D., and M. D. Stefano, 2007, Geophysical modeling via simultaneous joint inversion of seismic, gravity, and electromagnetic data: Application to prestack depth imaging: The Leading Edge, **26**, 326–331.

Constable, S. C., R. L. Parker, and C. G. Constable, 1987, Occams inversion: A practical algorithm for generating smooth models from electromagnetic sounding data: Geophysics, **52**, 289–300.

De Stefano, M., F. G. Andreasi, S. Re, M. Virgilio, and F. F. Snyder, 2011, Multiple-domain, simultaneous joint inversion of geophysical data with application to subsalt imaging: Geophysics, **76**, R69–R80.

Ellis, R. G., B. de Wet, and I. N. Macleod, 2012, Inversion of magnetic data from remanent and induced sources: ASEG Extended Abstracts, 1–4.

Gallardo, L. A., and M. A. Meju, 2003, Characterization of heterogeneous near-surface materials by joint 2D inversion of DC resistivity and seismic data: Geophysical Research Letters, **30**, 1658.

Gao, G., A. Abubakar, and T. M. Habashy, 2012, Joint petrophysical inversion of electromagnetic and full-waveform seismic data: Geophysics, **77**, WA3–WA18.

Gribenko, A., and M. Zhdanov, 2007, Rigorous 3D inversion of marine CSEM data based on the integral equation method: Geophysics, **72**, WA73–WA84.

Haber, E., and D. Oldenburg, 1997, Joint inversion: a structural approach: Inverse Problems, **13**, 63.

Hansen, P., 2010, Discrete inverse problems: Society for Industrial and Applied Mathematics.

Hohmann, G. W., 1975, Threedimensional induced polarization and electromagnetic modeling: Geophysics, **40**, 309–324.

Hu, W., A. Abubakar, and T. M. Habashy, 2009, Joint electromagnetic and seismic inversion using structural constraints: Geophysics, **74**, R99–R109.

Hursán, G., and M. S. Zhdanov, 2002, Contraction integral equation method in three-dimensional electromagnetic modeling: Radio Science, **37**, 1–13. (1089).

Jegen, M. D., R. W. Hobbs, P. Tarits, and A. Chave, 2009, Joint inversion of marine magnetotelluric and gravity data incorporating seismic constraints: Preliminary results of sub-basalt imaging off the Faroe Shelf: Earth and Planetary Science Letters, **282**, 47–55.

Jin, J., 2014, The finite element method in electromagnetics, 3rd ed.: Wiley-IEEE Press.

Lelièvre, P. G., and D. W. Oldenburg, 2009, A 3D total magnetization inversion applicable when significant, complicated remanence is present: Geophysics, **74**, L21–L30.

Li, Y., and D. W. Oldenburg, 1996, 3-D inversion of magnetic data: Geophysics, **61**, 394–408.

———, 2003, Fast inversion of large-scale magnetic data using wavelet transforms and a logarithmic barrier method: Geophysical Journal International, **152**, 251–265.

Li, Y., S. E. Shearer, M. M. Haney, and N. Dannemiller, 2010, Comprehensive approaches to 3D inversion of magnetic data affected by remanent magnetization: Geophysics, **75**, L1–L11.

Martin, R., V. Monteiller, D. Komatitsch, S. Perrouty, M. Jessell, S. Bonvalot, and M. Lindsay, 2013, Gravity inversion using wavelet-based compression on parallel hybrid CPU/GPU systems: application to southwest ghana: Geophysical Journal International, **195**, 1594–1619.

Molodtsov, D. M., V. N. Troyan, Y. V. Roslov, and A. Zerilli, 2013, Joint inversion of seismic traveltimes and magnetotelluric data with a directed structural constraint: Geophysical Prospecting, **61**, 1218–1228.

Moorkamp, M., B. Heincke, M. Jegen, A. W. Roberts, and R. W. Hobbs, 2011, A framework for 3-D joint inversion of MT, gravity and seismic refraction data: Geophysical Journal International, **184**, 477–493.

Newman, G. A., E. Gasperikova, G. M. Hoversten, and P. E. Wannamaker, 2008, Three-dimensional magnetotelluric characterization of the Coso geothermal field: Geothermics, **37**, 369–399.

Portniaguine, O., and M. S. Zhdanov, 2002, 3D magnetic inversion with data compression and image focusing: Geophysics, **67**, 1532–1541.

Power, M., and D. Hildes, 2007, Geophysical strategies for kimberlite exploration in northern Canada: Proceedings of the Fifth Decennial International Conference on Mineral Exploration, edited by B. Milkereit, 1025–1031.

Roscoe, W. E., and J. T. Postle, 2005, Diavik Diamond Mine mineral reserve and resource audit, prepared for Aber Diamond Corporation: Technical Report NI 43-101.

Stubley, M. P., 1998, Bedrock geology of the East Island area, Lac de Gras, prepared for Diavik Diamond Mines Inc.: Internal report, Stubley Geoscience.

Tikhonov, A. N., 1963, Solution of incorrectly formulated problems and the regularization method: Soviet Mathematics - Doklady, **4**, 1035–1038.

Čuma, M., G. A. Wilson, and M. S. Zhdanov, 2012, Large-scale 3D inversion of potential field data: Geophysical Prospecting, **60**, 1186–1199.

Vozoff, K., and D. L. B. Jupp, 1975, Joint Inversion of Geophysical Data: Geophysical Journal of the Royal Astronomical Society, **42**, 977–991.

Yip, C. G., 2008, Mineral resource and reserve update, Diavik Diamond Mine, Northwest Territories, Canada, prepared for Harry Winston Diamond Corporation: Technical Report Form 43-101F1.

Yip, C. G., and K. S. Thompson, 2015, Diavik Diamond Mine, Northwest Territories, Canada, prepared for Dominion Diamond Corporation: Technical Report NI 43-101.

Zhdanov, M. S., 2002, Geophysical inverse theory and regularization problems: Elsevier.

———, 2009, Geophysical electromagnetic theory and methods: Elsevier.

Zhdanov, M. S., A. Gribenko, and G. Wilson, 2012, Generalized joint inversion of multimodal geophysical data using Gramian constraints: Geophysical Research Letters, **39**, L09301.

Zhu, Y., M. Čuma, M. S. Zhdanov, and Y. Kinakin, 2014, Joint inversion of airborne gravity gradiometry and magnetic data from the Lac de Gras region of the Northwest Territories of Canada: SEG Expanded Abstracts, 1709–1713.

Zhu, Y., and M. S. Zhdanov, 2015, Joint inversion of airborne magnetic and electromagnetic data: case study in the Northwest Territories of Canada: SEG Expanded Abstracts, 864–868.

Zhu, Y., M. S. Zhdanov, and M. Čuma, 2013, Gramian constraints in the joint inversion of airborne gravity gradiometry and magnetic data: SEG Expanded Abstracts, 1166–1170.

———, 2015, Inversion of TMI data for the magnetization vector using Gramian constraints: SEG Expanded Abstracts, 1602–1606.